



A THESIS FOR THE

Master in Telecommunication Engineering

**MULTIPLEXING CAPABILITIES OF HOLOGRAPHIC
ANTENNAS WITH MULTIPLE POLARIZATIONS**

by
David Sardà Martin

SUPERVISOR: Xavier Mestre

Department of Telecommunication Engineering

Escola Tècnica Superior d'Enginyeria (ETSE)
Universitat Autònoma de Barcelona (UAB)

June 2024



El sotasingnant, *Xavier Mestre*, Professor de l'Escola Tècnica Superior d'Enginyeria (ETSE) de la Universitat Autònoma de Barcelona (UAB),

CERTIFICA:

Que el projecte presentat en aquesta memòria de Treball Final de Master ha estat realitzat sota la seva direcció per l'alumne *David Sardà Martin*.

I, perquè consti a tots els efectes, signa el present certificat.

Bellaterra, *June 2024*.

Signatura: Xavier Mestre.

Resum:

L'exploració de "extremelly large antenna arrays" (ELAAs) utilitzant espectre d'alta freqüència ha portat a una transició en el camp de la radiació electromagnètica, passant del cas d'ús comú de la propagació en camp llunyà a la propagació en camp proper. En aquest projecte, s'ha explorat el rendiment de les ELAAs en un escenari amb un transmissor ELAA i un receptor amb múltiples polaritzacions, estudiant el precodificador òptim que maximitza la capacitat. També s'ha desenvolupat i validat amb èxit l'aproximació hologràfica asimptòtica dels valors propis del canal i els modes actius disponibles quan s'utilitza aquest precodificador òptim per a diferents configuracions de polarització al transmissor. A més, s'ha comparat la diferència entre les diferents configuracions de polarització, mostrant que amb menys polaritzacions al transmissor, el nombre de modes actius és menor i la capacitat també es redueix.

Resumen:

La exploración de "extremelly large antenna arrays" (ELAAs) utilizando espectro de alta frecuencia ha llevado a una transición en el campo de la radiación electromagnética, pasando del uso común de la propagación en campo lejano a la propagación en campo cercano. En este proyecto, se ha explorado el rendimiento de las ELAAs en un escenario con un transmisor ELAA y un receptor con múltiples polarizaciones, estudiando el precodificador óptimo que maximiza la capacidad. También se ha desarrollado y validado con éxito la aproximación holográfica asintótica de los valores propios del canal y los modos activos disponibles al usar ese precodificador óptimo para diferentes configuraciones de polarización en el transmisor. Además, se ha comparado la diferencia entre las distintas configuraciones de polarización, mostrando que con menos polarizaciones en el transmisor, el número de modos activos es menor y la capacidad también se reduce.

Summary:

The exploration of extremely large antenna arrays (ELAAs) using high-frequency spectrum has led to a transition in electromagnetic radiation field, transitioning from the common use case of far-field propagation to near-field propagation. In this project it has been explored ELAAs performance in an scenario with a transmitter ELAA and a receiver with multiple polarizations, studying the optimal precoder that maximizes the capacity. It also has been developed and validated successfully the holographic asymptotic approximation of the eigenvalues of the channel and the available active modes when using that optimal precoder for different polarization configurations at the transmitter. Also, it has been compared the difference between the different polarizations configurations showing that with less polarizations at the transmitter the number of active modes is lower and the capacity also is being reduced.

Contents

List of Figures	vii
1 Introduction	1
2 State of the Art	5
2.1 Antenna Arrays	5
2.1.1 Benefits of antenna arrays	6
2.1.2 Types of Antenna Arrays	8
2.1.3 Beamforming	9
2.1.4 Last Improvements on Antenna Arrays	10
2.1.5 Extremely Large Antenna Arrays	11
2.2 Analysis of the capabilities of HMIMO	16
2.2.1 Introduction to HMIMO	17
2.2.2 HMIMO capabilities	17
2.2.3 Channel modeling and channel estimation	18
2.2.4 Research and applications	19
3 Effect of polarization on ELAAs: an asymptotic Study	23
3.1 Near Field Properties	24
3.1.1 Near-Field Properties for ELAAs	25
3.2 Scenario Description	26
3.3 Signal definition from scenario	28

3.4	Designing the optimum precoder	29
3.4.1	Designing the optimum precoder for fully polarized transmitter	30
3.5	Asymptotic behaviour of the channel eigenvalues	32
3.5.1	Previous considerations	33
3.5.2	Fully polarized transmitter	34
3.5.3	Double polarization transmitter	37
3.6	Activation of different transmit modes	38
3.6.1	Fully polarized transmitter	40
3.6.2	Double polarization transmitter	42
4	Numerical validation	45
4.1	Scenario by default	45
4.2	Calculating the optimum precoder matrix	46
4.2.1	Steps Followed	47
4.2.2	Analysing the capacity	47
4.3	Accuracy of the asymptotic approximations	53
4.3.1	Validation procedure	53
4.3.2	Matrix $\mathcal{W}^{t_{pol} \times r_{pol}}$ validation	53
4.3.3	Eigenvalues validation	57
4.4	Activation modes	61
4.4.1	Fully polarized Transmitter	62
4.4.2	Double Polarization Transmitter	63
4.4.3	Steps	64
4.4.4	Results analysis	65
4.4.5	Activation modes with power	69
5	Conclusions	73
5.1	Matlab code used	77

List of Figures

1.1	Bit rate limitation vs Bandwidth.	2
2.1	SCR-270 antenna installed in Hawaii during World War II to detect Japanese attacks.	6
2.2	Radiation pattern of an antenna array.	8
2.3	Phased antenna array.	10
2.4	Normalized gain of ELAAs	13
2.5	heat map of the normalized gain when the ELAA focuses a signal at the point(0, 0, $d_B = 1000 d_F$).	14
2.6	Normalized gain of ELAAs	14
2.7	Near-field ISAC network and four representative potential applications	15
2.8	Clarke's Channel estimations compared to Fourier plane-wave spectral representation	19
2.9	Future applications of HMIMO in 6G	20
3.1	Near Field and Far field	24
3.2	Wavefront seeing from an ELAA.	25
3.3	Scenario followed of an antenna array transmitter and a receiver with each of antenna and antenna elements is a three orthogonal dipole.	27
4.1	Capacity when the optimum precoder is done for each point on the grid for a fully polarized transmitter.	48
4.2	Optimum precoder calculated for position X=Y=2	49

4.3 Optimum precoder calculated for position X=Y=15	49
4.4 Capacity when the optimum precoder is done for just one point of the grid for a fully polarized transmitter	49
4.5 Capacity when the optimum precoder is done for each point on the grid for a double polarization transmitter	49
4.6 Optimum precoder calculated for position X=Y=2	50
4.7 Optimum precoder calculated for position X=Y=15	50
4.8 Capacity when the optimum precoder is done for just one point of the grid for a double polarization transmitter	50
4.9 Difference in capacity between fully polarized and double polarization transmitter when the optimum precoder is used at every point.	52
4.10 Relative error of component [1,1] for $r_{pol} = t_{pol} = 3$	54
4.11 Relative error of component [1,2] for $r_{pol} = t_{pol} = 3$	54
4.12 Relative error of component [2,2] for $r_{pol} = t_{pol} = 3$	54
4.13 Relative error of component [3,3] for $r_{pol} = t_{pol} = 3$	54
4.14 Accumulated absolute error at the power of 2 for matrix $\mathcal{W}^{t_{pol} \times r_{pol}}$	55
4.15 Relative error of component [1,1] for $r_{pol} = 3, t_{pol} = 2$	56
4.16 Relative error of component [1,2] for $r_{pol} = 3, t_{pol} = 2$	56
4.17 Relative error of component [2,2] for $r_{pol} = 3, t_{pol} = 2$	56
4.18 Relative error of component [3,3] for $r_{pol} = 3, t_{pol} = 2$	56
4.19 Accumulated absolute error at the power of 2 for matrix $\mathcal{W}^{t_{pol} \times r_{pol}}$	57
4.20 Relative error of eigenvalue 1 $r_{pol} = t_{pol} = 3$	58
4.21 Relative error of eigenvalue 2 for $r_{pol} = t_{pol} = 3$	58
4.22 Relative error of eigenvalue 3 for $r_{pol} = t_{pol} = 3$	58
4.23 Absolute error on eigenvalue 1 with fixed Area at position Y=60 and Z=80 for $r_{pol} = 3, t_{pol} = 3$	58
4.24 Absolute error on eigenvalue 2 with fixed Area at position Y=60 and Z=80 for $r_{pol} = 3, t_{pol} = 3$	58

4.25 Absolute error on eigenvalue 3 with fixed Area at position Y=60 and Z=80 for $r_{pol} = 3, t_{pol} = 3$	58
4.26 Relative error of eigenvalue 1 $r_{pol} = 3, t_{pol} = 2$	59
4.27 Relative error of eigenvalue 2 for $r_{pol} = 3, t_{pol} = 2$	59
4.28 Relative error of eigenvalue 3 for $r_{pol} = 3, t_{pol} = 2$	59
4.29 Absolute error on eigenvalue 1 with fixed Area at position Y=60 and Z=80 for $r_{pol} = 3, t_{pol} = 2$	59
4.30 Absolute error on eigenvalue 2 with fixed Area at position Y=60 and Z=80 $r_{pol} =$ $3, t_{pol} = 2$	59
4.31 Absolute error on eigenvalue 3 with fixed Area at position Y=60 and Z=80 for $r_{pol} = 3, t_{pol} = 2$	59
4.32 Ratio of eigenvalue 1 with corrected factor $r_{pol} = 3, t_{pol} = 3$	60
4.33 Ratio of eigenvalue 2 with corrected factor for $r_{pol} = 3, t_{pol} = 3$	60
4.34 Ratio of eigenvalue 3 with corrected factor for $r_{pol} = 3, t_{pol} = 3$	60
4.35 Ratio of eigenvalue 1 with corrected factor for $r_{pol} = 3, t_{pol} = 2$	61
4.36 Ratio of eigenvalue 2 with corrected factor for $r_{pol} = 3, t_{pol} = 2$	61
4.37 Ratio of eigenvalue 3 with corrected factor for $r_{pol} = 3, t_{pol} = 2$	61
4.38 SNR_M comparison with limits.	66
4.39 Activation modes in the space for $r_{pol} = 3, t_{pol} = 3$ (plot distance)	66
4.40 Activation modes in the space for $r_{pol} = 3, t_{pol} = 3$ (plot distance) with asymptotic approximation	66
4.41 Activation modes in the space for $r_{pol} = 3, t_{pol} = 3$ (plot points)	67
4.42 Activation modes in the space for $r_{pol} = 3, t_{pol} = 3$ (plot points) with asymptotic approximation	67
4.43 Activation modes in the space for $r_{pol} = 3, t_{pol} = 2$ (plot distance)	68
4.44 Activation modes in the space for $r_{pol} = 3, t_{pol} = 2$ (plot distance) with asymptotic approximation	68
4.45 Activation modes in the space for $r_{pol} = 3, t_{pol} = 2$ (plot points)	68
4.46 Activation modes in the space for $r_{pol} = 3, t_{pol} = 2$ (plot points) with asymptotic approximation	68

4.47 Activation modes in the space for $r_{pol} = 3, t_{pol} = 2$ with power 10^6 W	69
4.48 Activation modes in the space for $r_{pol} = 3, t_{pol} = 3$ with power 10^3 W	69
4.49 Activation modes in the space for $r_{pol} = 3, t_{pol} = 3$ with power 10^{-2} W	70
4.50 Activation modes in the space for $r_{pol} = 3, t_{pol} = 2$ with power 10^6 W	70
4.51 Activation modes in the space for $r_{pol} = 3, t_{pol} = 2$ with power 10^3 W	70
4.52 Activation modes in the space for $r_{pol} = 3, t_{pol} = 2$ with power 10 W	71
4.53 Activation modes in the space for $r_{pol} = 3, t_{pol} = 2$ with power 10^{-4} W	71

Chapter 1

Introduction

Day after day, in wireless communications systems there's a growing demand, increasing the data to transmit and the number of users that we need to transmit data, recent advances and new technologies based on data in telecommunications, need to increase the capable bit-rate of the systems, such as IoT (Internet of Things) that requires a constant flow of data. To sustain this growth, we need to increase the capacity of our systems.

The Shannon theorem, from 1948, provides the fundamental limit on the maximum achievable data rate (capacity) of a communication channel as:

$$C = B \log_2(1 + SNR) = B \log_2 \left(1 + \frac{P\beta}{BN_0} \right) \quad (1.1)$$

Where B is the bandwidth, P is the transmit power, $\beta \in [0, 1]$ channel gain, and N_0 noise spectral density. From this we can note that the easiest way to increase the capacity is increasing the bandwidth since it is outside the logarithm. To achieve that, wireless communication standards have been constantly moving to higher frequency spectrum bands, which are less populated and allow for higher transmission bandwidths. For example, in 4G we worked on different frequency ranges like 700 MHz, 800 MHz, 1800 MHz, 2100 MHz, and 2600 MHz, with 5G we work at different frequency ranges, but if we focus on the upper-bands, they work at frequency ranges above 24-52 GHz. It is anticipated that 6G may utilize even higher frequency bands, including the terahertz (THz) spectrum, for ultra-high-speed communication and novel applications.

With the increase of the bandwidth, it is expected to get better bit rate, but these new frequencies are less favourable in terms of propagation (higher channel losses) meaning that we will need to increase the power, increasing also the interference to the users at other locations.

Even considering that we can increase the bandwidth indefinitely ($B \rightarrow \inf$) as we can see on equation 1.1, the part inside the logarithm tend to be $1 + x$, for $x \approx 0$ we can approximate the logarithm as $\log(1 + x) \approx \frac{x}{\ln(2)}$, then despite that the B that

multiples the logarithm the capacity will converge at $\frac{P\beta}{N_0 \ln(2)}$, that can be see on the following Figure 1. [Ram23]

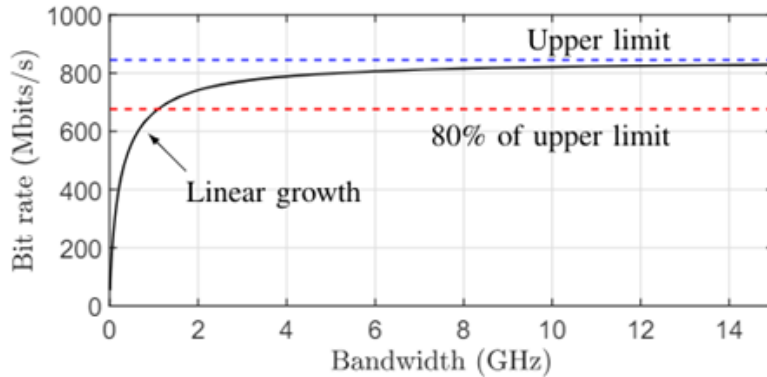


Figure 1.1: Bit rate limitation vs Bandwidth.

Shannon has made several relevant contributions to communications, establishing key limits that define the capabilities of communication systems. From a Shannon theorem reformulation we could extract that the maximum number of streams in MIMO (Multiple Input Multiple Output) systems, which is determined by the minimum of the number of transmit antennas and receive antennas. This limit is crucial for leveraging spatial diversity to maximize data throughput and signal reliability.

Extremely Large Antenna Arrays (ELAAs) take this concept further by utilizing a vast number of spatially distributed antennas. This large aperture enhances the spatial resolution and capacity of MIMO systems, allowing for the transmission of a higher number of independent data streams. In ELAAs, the ability to deploy a an extensive array of antennas significantly increases the number of spatial channels and also allowing to focus the power of a signal in a particular region of the space thereby pushing the boundaries of both Shannon's limit, improving the number of simultaneous streams and incrementing the capacity of the system. This advanced configuration is essential for achieving higher data rates and improving spectral efficiency, making ELAAs a cornerstone technology for next-generation communication networks.

Practically, ELAAs enable MIMO systems to exploit spatial diversity across a broader spectrum, from Wi-Fi networks to cellular systems and beyond and allowing to have low interference to near sytems. By integrating hundreds or even thousands of antennas within a confined area, ELAAs can support the simultaneous transmission of multiple data streams to multiple users, enhancing network capacity and efficiency. This capability is particularly advantageous in dense urban environments and areas with high user density, where traditional MIMO configurations may face limitations due to space or regulatory constraints. Moreover, ELAAs facilitate adaptive beamforming and spatial multiplexing techniques, optimizing signal propagation and reducing interference. As wireless communication technologies evolve towards 5G and beyond, ELAAs,

along with advanced antenna arrays, promise to play a significant role in meeting the increasing demand for higher data rates, seamless connectivity, and robust performance, especially in the forthcoming 6G networks.

But ELAAs also have inconveniences, since predicting the behaviour of all of that antennas so we can transform the signal to send to fully take advantage of this mentioned capabilities can be very hard computationally. In this project we will do some exploration about this capabilities of ELAAs allowing to demonstrate this characteristics and building some approximations to facilitate the computational cost of building an antenna array and predict it's behavior.

The main technical objectives of this project are:

- Explore the state of the art in ELAAs and Holographic Massive-Input Multiple-Output (HMIMO) systems in telecommunications. This includes reviewing current research, identifying key challenges, and understanding the potential applications and benefits of these advanced technologies.
- Investigate the state of the art in near-field communication techniques specifically for ELAAs and Holographic MIMO (HMIMO). Focus on understanding the unique characteristics of near-field propagation, the impact on system performance, and the latest methodologies for optimizing near-field communication in ELAA systems.
- Conduct a detailed study and implementation using Matlab of the optimal transmitter design for capacity maximization. This involves mathematical modeling, algorithm development, and simulation to identify the best strategies for enhancing the capacity of ELAA-based systems.
- Study, implement in Matlab, and verify the approximation accuracy of the eigenvalues of the electromagnetic channel. We will compare the asymptotic approximations that will simplify the necessary calculations and those obtained directly from the channel definition in an ELAA scenario. This analysis will cover cases involving fully polarized and double-polarization transmitters, providing insights into how polarization affects channel properties and capacity. This includes working on the formulation to obtain these parameters.
- Study, implement in Matlab, and verify the number of available active modes across the space for both asymptotic approximations that will simplify the necessary calculations and those obtained directly from the channel definition in an ELAA scenario. This includes working on the formulation to obtain these parameters, examining the distribution and behavior of active modes for both fully polarized and double-polarization transmitters, and understanding their implications on system performance and capacity.

Chapter 2

State of the Art

In this section, we explore the current advancements and research in the field of antenna arrays, with a particular focus on ELAAs. Antenna arrays have been a cornerstone in the development of modern communication systems, enabling the enhancement of signal reception and transmission through spatial diversity and beamforming techniques. As the demand for higher data rates and greater network capacity continues to grow, the development of ELAAs has gained significant attention. These antennas are designed to operate effectively at large scales, offering potential improvements in coverage, resolution, and overall system performance.

We begin by reviewing the fundamental concepts of antenna arrays and ELAAs, including a brief overview of the theory behind antenna arrays, their various types, and their common applications. Understanding these basics is crucial for appreciating the complexities and innovations discussed in later sections. Following this theoretical overview, we will delve into the latest studies and methodologies aimed at improving the capacity and performance of ELAAs. This includes innovations in design, signal processing algorithms, and integration techniques aimed at overcoming the inherent challenges associated with large aperture sizes, such as increased complexity and bandwidth requirements. By examining the latest research and technological advancements, this section provides a comprehensive overview of the current state of ELAAs and highlights the key trends and future directions in this rapidly evolving field.

2.1 Antenna Arrays

An antenna array is a group of connected antennas arranged in a regular structure to form a single transmitter/receiver. Each individual antenna, called an element, is connected to a single receiver or transmitter. The radio waves from each element combine, enhancing power in desired directions and canceling it in other directions to enhance the performance of the

system. They are fundamental in modern communication systems because they offer significant advantages over single antennas. By controlling the relative phase and amplitude of the signal at each element, the array can form a directive beam, which improves signal strength and reduces interference from unwanted directions.

Antenna arrays can also be designed to operate over a wide range of frequencies, making them versatile for different applications. The spacing between elements is typically a function of the wavelength of the operating frequency, which affects the overall size of the array. In practice, antenna arrays are used in various fields including telecommunications, radio astronomy, and defense. They are critical in systems where directional transmission and reception of signals are essential. The ability to electronically steer the beam without moving the antenna physically is a significant advantage, especially in dynamic environments.

In Figure 2.1, we can see a real-life antenna array. This is a picture of the SCR-270 antenna installed in Hawaii during World War II to detect Japanese attacks. It worked at 110 MHz, so the elements were large and far from each other:



Figure 2.1: SCR-270 antenna installed in Hawaii during World War II to detect Japanese attacks.

2.1.1 Benefits of antenna arrays

Antenna arrays use multiple antennas fed from the same transmitter or receiver. By adjusting the phase of the currents, the spherical waves from individual antennas combine at far field from plane waves, creating a beam of radio waves in a specific direction. Constructive interference occurs when waves are in phase, enhancing radiated power. Destructive interference occurs when waves are out of phase, reducing power in undesired directions. During reception, in-phase signals from desired directions reinforce each other, while out-of-phase signals from other directions cancel out. This improves signal strength, directivity, and reduces interference, enhancing overall communication performance.

Antenna arrays play a crucial role in wireless communications and radar systems. Some key points that have proven that antenna arrays can have a huge impact on telecommunications are:

- **Diversity Gains:** Antenna arrays exploit spatial diversity by using multiple antennas. When signals experience fading due to multipath propagation, different antennas may encounter varying fading conditions. By combining their outputs, the overall signal quality improves.
- **Interference Mitigation:** Antenna arrays can nullify interference from unwanted directions. By adjusting the array's weights, the main beam can be steered away from interfering sources. There are several null steering algorithms that help to minimize interference while maintaining desired signal strength.
- **Spectrum Reuse:** Antenna arrays facilitate spectrum reuse, enhancing overall network capacity.
- **Coverage Enhancement:** Arrays extend coverage by focusing energy where needed. This is specially useful when using high frequency bands, since propagation conditions are much worse than in usual (below GHz) bands.

All of items of the previous list, can be achieved with beamforming techniques, so beamforming, that we will talk more in deep in section later, is very important technique that help antenna array to have a crucial role in telecommunications systems, giving them a very desirable characteristics.

We can explore how antenna arrays behave with their radiation pattern, but before we need to take into account that the radiation pattern will give us an idea of how they behave but only on the far-field, since the radiation pattern assumes it depends only on the viewing angle. In the near field, electromagnetic interactions are more complex, involving significant variations in amplitude and phase with distance, thus requiring more detailed analysis beyond angular dependencies.

The radiation pattern of antenna array includes a main lobe, which is a strong, focused beam in the desired direction, and several sidelobes, which are weaker beams at various angles. These sidelobes represent unintended radiation in other directions. Increasing the size of the antenna and the number of its elements results in a narrower main lobe and higher gain, meaning the main beam becomes more focused and powerful. Additionally, this reduces the strength of the sidelobes, minimizing radiation in unwanted directions.

In the Figure 2.2 we can see the radiation pattern of an antenna array, as we can see in the image we can expect from antenna arrays a large directivity towards the desired direction,

focusing the signal into a user and in other directions the directivity will be much lower, allowing to have not much interference into other users.

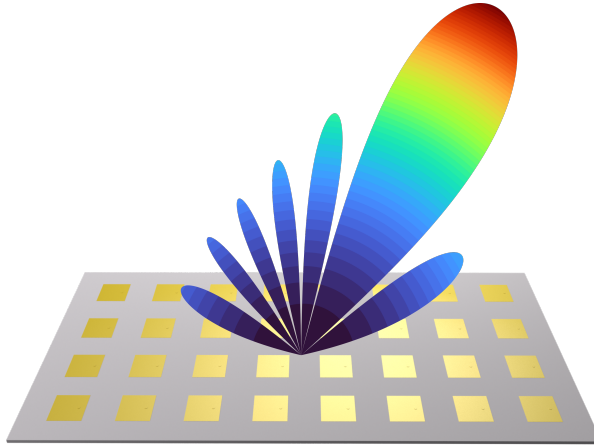


Figure 2.2: Radiation pattern of an antenna array.

2.1.2 Types of Antenna Arrays

Antenna arrays come in various configurations, each designed to meet specific requirements and applications. These configurations determine the arrangement of the individual antenna elements and influence the array's beamforming capabilities, directionality, and overall performance. Understanding the different types of antenna arrays helps in selecting the appropriate design for a given application, whether it be in telecommunications, radar, satellite communications, or other fields. Below are some common types of antenna arrays:

- **Linear Arrays:** Linear arrays consist of antenna elements arranged in a straight line. They are commonly used in applications like radar and wireless communication. By adjusting the phase and amplitude of the signals at each element, linear arrays can steer the beam in the horizontal plane. For it's simplicity this will be the kind of arrays considered in this project.
- **Planar Arrays:** Planar arrays have antenna elements arranged in a two-dimensional grid. This configuration allows for beam steering in both horizontal and vertical planes, providing greater control over the direction and shape of the beam. Planar arrays are often used in advanced applications such as satellite communications and phased-array radar systems.
- **Circular Arrays:** Circular arrays feature antenna elements arranged in a circular pattern. This arrangement provides omnidirectional beam steering capabilities, allowing for equal

performance in all directions around the circle. Circular arrays are useful in applications requiring 360-degree coverage, such as direction finding and certain types of communication systems.

2.1.3 Beamforming

Beamforming is a signal processing technique used in antenna arrays to direct the transmission or reception of signals in specific directions. It enhances signal strength in the desired direction while minimizing interference from other directions.

Beamforming works by adjusting the relative phase and amplitude of the signals at each antenna element. By precisely controlling these parameters, the signals can constructively interfere in the desired direction or region and destructively interfere in unwanted ones. This results in a focused beam of radio waves that improves communication performance and reduces interference.

As we seen, beamforming have a huge role on the improvements on antenna arrays, so let's take a more closer view to what we are achieving with beamforming and why it is so important:

- **Directional Radiation Pattern:** Antenna arrays allows the system to focus the signal in a specific direction, improving the signal quality and reducing interference. This allows that with different beamforming techniques to focus beams to different specific users or regions, allowing transmission and reception on the same frequencies.
- **Interference Rejection:** Antenna arrays can reject interfering signals having a direction of arrival different from that of a desired signal [Dir]. This can significantly improve the signal-to-noise ratio, enhancing the overall performance of the system.
- **High Gain and Increased Directivity:** The use of antenna beamforming allows the antenna array to achieve higher gains and increased directivity compared to a single antenna [Zhu23]. This can result in improved signal quality, increased range, and reduced interference.
- **Compensation for Signal Loss at Higher Frequencies:** At higher frequencies such as mmWave, the signal becomes really weak due to enormous losses. Antennas are joined into arrays to compensate for this, offering high directive gain and beamforming capabilities [Com].

There are several ways with antenna arrays to achieve beamforming, one of the more typical and most well known are phased antenna arrays. Phased antenna arrays have the unique ability

to change the shape and direction of the radiation pattern without physically moving the antenna. Elements in an antenna array are placed in such a way that the signals transmitted by individual antennas sum up and provide better gain, directivity and performance in a particular direction. This is achieved by transmitting signals of the same frequency from all the individual elements in the array but with a certain phase difference/shift between each antenna element in the array. The phase shift is calculated to provide constructive interference in the desired direction while destructive interference may occur in other directions.

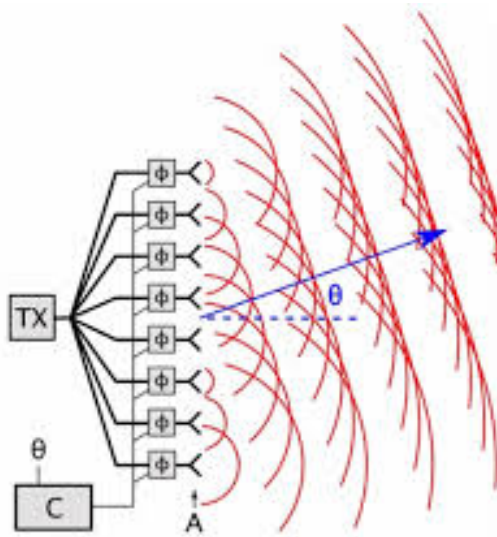


Figure 2.3: Phased antenna array.

2.1.4 Last Improvements on Antenna Arrays

Antenna arrays have a huge impact in telecommunications, but there's still a lot of improvements that can be done. Researchers realized about that and bring new studies about it from different perspectives, from integrating with other technologies, material improvements, new architectures... Let us show some examples of recent studies and improvements on antenna arrays as examples:

- **Components and design improvements:** For example on [Liu24] a novel patch phased array antenna with improved scanning performance is presented. Where the active element pattern is changed as desired through a modified SIW cavity, resulting in an extension of the phased array's 3 dB scanning range.
- **Using deep learning for adaptive beamforming in Massive MIMO:** As said integrating technologies as deep learning for example using deep learning for adaptive beamforming in Massive MIMO include efficient channel estimation with CNNs and RNNs,

hybrid beamforming optimization to reduce RF chain requirements, and end-to-end learning frameworks for directly mapping input signals to beamforming vectors, resulting in improved spectral efficiency and robust performance in dynamic environments.

- **Conformal Antenna Arrays:** A conformal antenna array is a flat radio antenna designed to conform to a specific shape while maintaining its performance, often a curved surface, with each element connected to a phase shifter for high directivity, typically used at high frequencies like UHF or microwave. Li on [Li22] presents a design for a dipole with four branches, which is fed by a Marchand balun and is intended to be conformal with the wing of an unmanned aerial vehicle. The design achieves better impedance matching performance and moves the scanning blindness out of the operating frequency band.

2.1.5 Extremely Large Antenna Arrays

The evolution of antenna arrays represents a remarkable journey in the field of wireless communication technology. Initially, antenna arrays emerged as an innovative approach to enhance the performance of individual antennas by combining multiple elements in a structured configuration. These early antenna arrays, often referred to as Large Antenna Arrays (LAAs), paved the way for significant advancements in signal processing, beamforming, and spatial diversity techniques.

As communication needs expanded and technology progressed, traditional antenna arrays evolved into ELAAs to meet the growing demand for enhanced performance and capabilities. ELAAs incorporate a vast number of antenna elements, often distributed over a large area or spanning multiple locations, to achieve unprecedented levels of sensitivity, resolution, and coverage. This evolution has been fueled by advancements in materials, electronics, signal processing, and network infrastructure. New materials and fabrication techniques enable the creation of smaller, more efficient antenna elements, while advancements in electronics and signal processing allow for sophisticated beamforming and signal optimization algorithms. Additionally, the proliferation of high-speed data networks and cloud computing infrastructure has facilitated the deployment and management of large-scale ELAAs, further pushing the boundaries of scientific research, telecommunications, radio astronomy, and other fields.

With the rise of bandwidth-intensive applications such as high-definition video streaming, virtual reality, and IoT devices, there has been an unprecedented need for higher bit-rate transmission and improved signal quality. ELAAs address this demand by providing the necessary infrastructure to support seamless connectivity, real-time data transmission, and efficient spectrum utilization.

ELAAs represent the evolution of large antenna arrays (LAAs) and are poised to revolutionize wireless communication systems, particularly in the context of future 6G technology.

ELAAs are characterized by their significantly expanded array aperture, enabling them to support ultra-high-speed communications and deliver unprecedented levels of performance. These arrays leverage advanced beamforming and precoding techniques to optimize signal transmission, thereby enhancing network capacity and coverage. As the demand for faster and more reliable wireless connectivity continues to grow, ELAAs are expected to play a crucial role in meeting these demands and unlocking the full potential of next-generation communication networks.

ELAAs compared to antenna array technology, are distinguished by their extensive scale and enhanced capabilities compared to traditional antenna arrays. ELAAs are characterized by their substantially expanded aperture, achieved by incorporating a vast number of antenna elements distributed over a large area or spanning multiple locations.

The key differentiators of ELAAs from traditional antenna arrays lie in their scale, complexity, and performance capabilities:

1. **Scale:** ELAAs are typically much larger in size compared to traditional antenna arrays. They may encompass hundreds or even thousands of antenna elements, arranged in a structured configuration to achieve specific performance objectives.
2. **Complexity:** ELAAs are more complex in terms of design, deployment, and operation. They require sophisticated signal processing algorithms and beamforming techniques to optimize performance and adapt to changing environmental conditions.
3. **Performance:** ELAAs offer enhanced performance characteristics, including increased sensitivity, resolution, and coverage. By leveraging a large number of antenna elements, ELAAs can achieve higher gain, improved spatial resolution, and greater flexibility in directing and shaping electromagnetic beams.
4. **Applications:** ELAAs enable a wide range of applications across various fields, including telecommunications, radar, radio astronomy, and wireless sensor networks. They are particularly well-suited for high-speed data transmission, massive MIMO systems, and next-generation communication networks, such as 6G.

However, it is important to note that while there is ongoing research and development in this area, full-scale practical implementations of ELAAs might still be in the future.

2.1.5.1 ELAAs capabilities

When we work with ELAAs, we need to consider that they don't work like just single antennas, they have they particularities and researches have carried studies to show that and explore all the possibilities that ELAAs give us.

For example if we take a look to the normalized gain, antenna gain that is scaled maximum gain of the antenna, of ELAAs we can see that as shown in [Ram23] it depends on the distance in the radiative near-field (explained later), but normalised gain converges to its maximum value at a distance much shorter than the Fraunhofer array distance. Hence, we can usually achieve the maximum array gain in the near-field.

Ramezani considers for his study suppose an scenario where a single-antenna isotropic transmitter located at the location $(0, 0, z)$ sends a signal to an ELAA deployed in the xy plane centered at the origin. The behaviour of the normalized gain can be explained theoretically with the following equations.

Consider a planar array that has N antennas in each row and M antennas in each column, where A is the physical area of each antenna, $\mathcal{S}_{m,n}$ is the set of points in the xy-plane spanned by the antenna in the m th row and n th column of the ELAA, \mathcal{S} is the area spanned by the reference antenna located in the origin.

$$G_{\text{array}} = \frac{\sum_{m=1}^M \sum_{n=1}^N \left| \int_{\mathcal{S}_{m,n}} E(x, y) dx dy \right|^2}{M N A \int_{\mathcal{S}} |E(x, y)|^2 dx dy} \quad (2.1)$$

where:

$$E(x, y) = \frac{E_0}{4\pi} \frac{\sqrt{z(x^2 + z^2)}}{(x^2 + y^2 + z^2)^{5/4}} e^{-j \frac{2\pi}{\lambda} \sqrt{x^2 + y^2 + z^2}} \quad (2.2)$$

is the electric field measured an arbitrary point $(x, y, 0)$ with E_0 being the electric density.

This can be seen in Figure 2.4 where they plot the array normalized gain according to the previous demonstrated equation for ELAAs with different numbers of antennas. In particular, the solid blue curve shows the array gain for an ELAA with $M = 30$ rows and $N = 40$ columns of antennas, while the dotted red curve represents the array gain of another ELAA with $M = 300$ and $N = 400$.

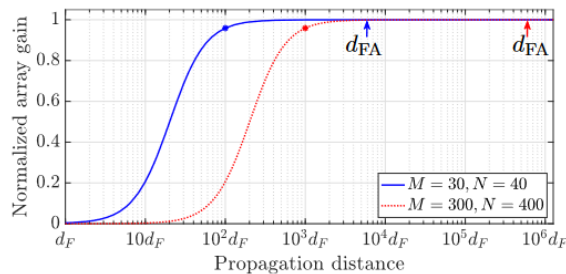


Figure 2.4: Normalized gain of ELAAs

They studied the beamfocusing with ELAAs in this paper, but before let us differentiate between the term beamforming and beamfocusing. Beamforming is a technique that directs a

wireless signal towards a specific receiving device, rather than spreading the signal omnidirectionally. Beamfocusing is a special kind of 3D-beamforming where most of the radiated power is concentrated in a confined focal region around a point in the 3D space, defined by both angular (azimuth and elevation angles) and radial domains. [Mon23]

Also, they showed how ELAAs are capable of beamfocusing enabling to give to the location of the user a lot of power, but giving very low interference to other users that can be around it and as you can see the beamfocusing is very precise in the sense the region where the power received is significant is very small. Similar studies they have been conducted for RIS as you can see on [Bj1]

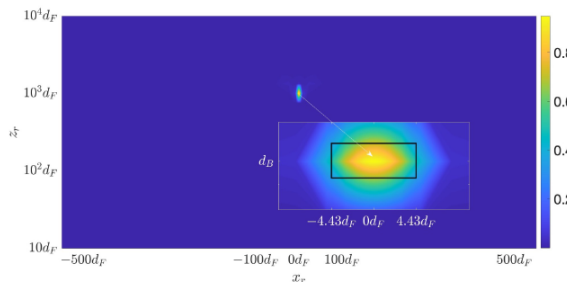


Figure 2.5: heat map of the normalized gain when the ELAA focuses a signal at the point $(0, 0, d_B = 1000 d_F)$.

In the same study, they also showed that ELAAs are capable to transmit to different users in the near field with a limited interference between them, this behaviour has also been validated in other studies like for example [Cui22]. The following figure 2.6 show the results obtained where they configured shown the normalized array gains for five focal points in the same direction (five users in the same angular direction) that have non-overlapping 3 dB BWs:

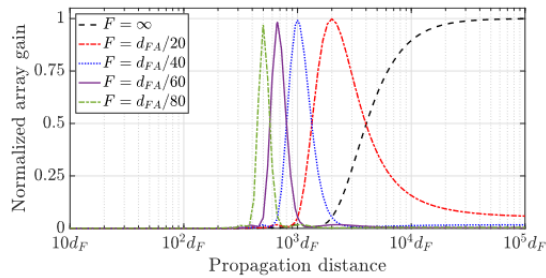


Figure 2.6: Normalized gain of ELAAs

2.1.5.2 ELAAs applications

ELAAs are meant to have a significant impact on wireless communications, different articles present different examples of how ELAAs can be used in different applications, for example on [He24] the authors discuss different applications of ELAAs integrated with ISAC (Integrated Sensing and Communication) for the future.

ISAC merges wireless communication and sensing into one system, optimizing resources and enabling advanced applications like smart cities. ISAC can be present in advanced applications such as autonomous driving and smart cities. ELAAs are particularly well-suited for ISAC due to their high spatial resolution and beamfocusing capabilities, which leverage additional spatial degrees of freedom (DoFs) in the near-field regime. Let us view the potential applications of ISAC with ELAAs.

- **Integrated Localization and Communication:** ELAAs enhance base stations' ability to support both localization and communication by leveraging near-field spherical-wave propagation, allowing direct estimation of user location from uplink signal angles and enabling simultaneous communication and target sensing in downlink scenarios.
- **Interference Management:** The beamfocusing capability of ELAAs mitigates mutual interference in ISAC systems by managing interference in radar-communication coexistence scenarios and utilizing the abundant spatial DoFs to enhance overall system performance.
- **Physical-Layer Security Enhancement:** ELAAs improve physical-layer security by focusing signals on specific targets, minimizing information leakage, and preventing eavesdropping, especially in near-field scenarios where an eavesdropper is close to the target.
- **Multi-Station Collaborative ISAC:** ELAAs enable multi-station collaborative ISAC by offering wider coverage and improved performance through joint transmission and reception at distributed nodes, increasing spatial multiplexing gain and capacity while suppressing interference and maximizing probing power.

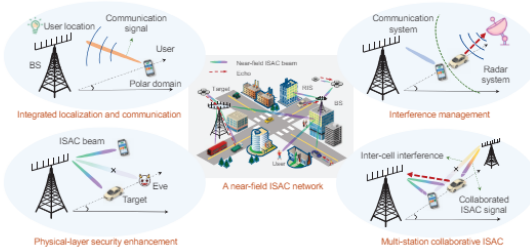


Figure 2.7: Near-field ISAC network and four representative potential applications

ELAAs is still a technology that researchers are working on so there are not much active projects with an advance state. An example of practical implementation of ELAAs could be The Next Generation Very Large Array (ngVLA), which is an ambitious project developed by the National Radio Astronomy Observatory (NRAO) aimed at revolutionizing radio astronomy capabilities. It entails constructing a sophisticated interferometric array consisting of 244 large antennas, each 18 meters in diameter, and 19 smaller antennas, each 6 meters in diameter, distributed over a vast area. Operating at frequencies ranging from 1.2 GHz to 116 GHz, the ngVLA is designed to achieve unprecedented sensitivity and spatial resolution, enabling groundbreaking scientific discoveries across various fields of astrophysics.

The ngVLA project addresses key science goals, including unveiling the formation of solar system analogues, probing planetary system conditions with astrochemistry, charting galaxy assembly and evolution, understanding the formation and evolution of black holes, and testing fundamental principles of gravity using Galactic Center pulsars. Through ultra-sensitive imaging capabilities, the ngVLA aims to provide milliarcsecond resolution, offering new insights into the Universe. This project is currently in the design and development phase, the ngVLA is anticipated to commence full science operations by mid-2034.

2.2 Analysis of the capabilities of HMIMO

Now that we have introduced antenna arrays and ELAAs, which are cutting-edge advancements in wireless communication technology poised to significantly boost system capacity and performance, we can delve deeper into their capabilities. These arrays incorporate numerous densely packed antenna elements, enabling them to achieve superior spatial resolution and advanced beamforming capabilities, essential for meeting the increasing demand for higher data rates and more reliable connections in today's communication networks.

In this context, we explore the state-of-the-art in ELAA technology, focusing on methodologies to analyze and optimize their capacity and performance. A key area of interest involves employing beamfocusing techniques to enhance signal delivery efficiency and reduce interference. Researchers are also integrating ELAAs' capabilities into Holographic MIMO (HMIMO) systems. By leveraging ELAAs' precise beamforming and adaptive signal processing capabilities, studies aim to improve the spatial resolution and efficiency of HMIMO. This collaborative approach not only enhances HMIMO's performance but also extends its applicability across diverse scenarios in next-generation wireless networks. By harnessing the strengths of ELAAs, researchers are paving the way for more robust and adaptable communication systems that can meet the evolving demands of modern connectivity needs.

In the subsequent sections, we will delve into the state-of-the-art of HMIMO, exploring recent

advancements and methodologies that enhance their effectiveness in wireless communication systems.

2.2.1 Introduction to HMIMO

Holographic Multiple-Input Multiple-Output (HMIMO) communications use intelligent meta-surfaces, which are flat structures made of tiny meta-atoms that manipulate electromagnetic waves. Alternatively, HMIMO can be implemented by creating a surface with numerous small, closely spaced antennas. This implementation allows to control wave properties like strength, phase, and direction very precisely, allowing HMIMO to create clear and focused signals. By packing many of these radiating elements closely together, HMIMO forms a continuous electromagnetic space that can approach the highest possible data limits in wireless communication. This technology uses efficient methods to adjust signal strength and direction without needing traditional radio frequencies, which saves on costs and energy. As the number of elements increases, HMIMO can produce narrow beams of signals that minimize spreading, making it ideal for clear communication in places without obstacles.

2.2.2 HMIMO capabilities

Now, let us explore more technically the capabilities of HMIMO. Let's begin talking about the number of simultaneous streams that we can have with HMIMO. The spatial DoF refers to the number of independent data streams that can be simultaneously transmitted through the wireless propagation environment. When the transceiver aperture is sufficiently large and includes a massive number of elements, the normalized spatial DoF in HMIMO is asymptotically limited by [An23a]:

$$DoF = \begin{cases} \frac{2}{\lambda} \text{ per meter,} & \text{Linear array} \\ \frac{\pi}{\lambda^2} \text{ per square meter,} & \text{Planar array} \end{cases} \quad (2.3)$$

Dardari explored the Degrees of Freedom (DoF) in point-to-point HMIMO systems with different transceiver setups and near-field communications, finding that spatial DoF can exceed one even in strong line-of-sight (LoS) conditions, thus increasing HMIMO channel capacity [An23a].

Lu and Zeng [Lu21] derived a closed-form expression for SNR using optimal single-user MRT-based beamforming, considering signal phase, amplitude, and projected aperture variations across array elements in both far-field and near-field scenarios. They found that SNR increases with the number of elements but with diminishing returns. They proposed a uniform-power distance criterion to refine near- and far-field separation. Wang [An23a] showed that an LoS-dominated HMIMO system can achieve a power gain of about 9.94 dB (3.30 bits/s/Hz SE

increase) in far-field scenarios compared to conventional MIMO. However, as aperture increases, signal attenuation and polarization mismatch increase, resulting in a maximum channel power gain of 1/3 in the near field.

Let's now analyse the capacity which will give us important vision on how HMIMO is improving the the number of users we can serve at the same time. It can be demonstrated that the ergodic capacity of a point-to-point HMIMO system can be calculated as:

$$C = \max_{\mathbf{Q}_a: \text{tr}(\mathbf{Q}_a) \leq 1} \mathbb{E} \left[\log_2 \det \left(\mathbf{I}_{n_r} + \gamma \mathbf{H}_a \mathbf{Q}_a \mathbf{H}_a^H \right) \right] \quad (2.4)$$

where $\mathbf{Q}_a = \mathbb{E}[\mathbf{x}_a \mathbf{x}_a^H]$ is the transmit covariance matrix with dimensions $(2M + 1) \times (2M + 1)$, being M half of the number of transmit antennas, and trace $\text{tr}(\mathbf{Q}_a) \leq 1$, γ is the signal-to-noise ratio (SNR) at the receiver, and \mathbf{H}_a is the channel matrix from the transmitter to the receiver.

When working with holographic beamforming we can distinguish four typical scenarios which are i) point-to-point, ii) multi-user, iii) wideband and iv) near-field. In our case we will focus in that last case which can also explain the other scenarios.

In the near-field region of HMIMO systems, novel opportunities arise for improving performance. Exploiting distance information and phase variations enables effective beam-focusing techniques, enhancing throughput and mitigating interference (Zhang, [Zha22]). This approach utilizes customized beams to achieve new DoF as explained previously, addressing both angular and distance-domain interference challenges that conventional far-field beamforming cannot handle. Additionally, Wei [Wei22] investigate triple polarization schemes for multi-user HMIMO, demonstrating a threefold increase in capacity compared to conventional systems, thanks to compact sub-wavelength antennas and innovative polarization strategies.

2.2.3 Channel modeling and channel estimation

The channel modeling is an important part to analyse the results that we can obtain, since it will allow us to predict and understand signal behavior. There are two groups of techniques for channel modeling [An23b]:

- Deterministic channels are typically characterized either through ray tracing or actual channel measurements to model the propagation environment
- Stochastic models which are preferred for conducting communication theoretic analysis, since they provide valuable insights into the statistical properties of a class of propagation environments, an example of that group is Clarke's classic stochastic model relies on the assumption of an isotropic and scalar wave propagation environment in the far field.

Having accurate channel state information (CSI) is crucial for recovering signals at the receiver but also in order to construct the optimum transmitter. Unfortunately, channel estimation becomes extremely challenging in HMIMO systems due to the use of electromagnetically large surfaces. Researchers have developed different techniques tailored for single-user scenarios, which can be readily adapted for multi-user scenarios by assigning orthogonal pilot sequences to each user. For practical multiuser HMIMO communications, it will be necessary determine the appropriate pilot reuse factor and design the pilot pattern to strike a favorable tradeoff between the overhead and the achievable performance, which will make this scenario more complex. Some examples are for example O.T. Demir. [An23b] proposed a subspace-based channel estimation technique leveraging the rank deficiency in spatial correlation matrices due to dense antenna deployment, achieving superior performance over LS estimators without prior channel statistics. An example is Demir proposed a subspace-based channel estimation technique leveraging the rank deficiency in spatial correlation matrices due to dense antenna deployment, achieving superior performance over LS estimators without prior channel statistics.

For channel modeling and channel estimation there have been several studies to verify their performance, for example on [An23b], we can see comparison from the estimations like on Figure 2.8, where they are comparing the channel estimations from Clarke and the Fourier plane-wave spectral representation.

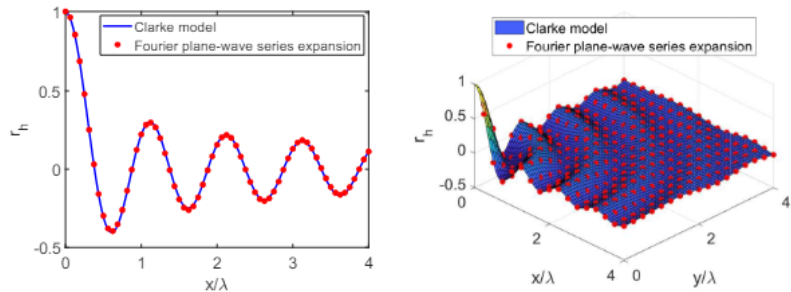


Figure 2.8: Clarke's Channel estimations compared to Fourier plane-wave spectral representation

2.2.4 Research and applications

While the broader concept of MIMO technology have been around since the 1990s, the specific focus on HMIMO, characterized by the deployment of extremely large antenna arrays, has gained significant attention and research interest mainly in the past decade with the higher demands on bit-rate for the telecommunications and it's a concept that it's call to have a significant impact in telecommunications that's why there a lot of research's and possible investigation lines around this concept, and it is being considered to use in a lot of environments.

For example, some studies about the hardware architecture around HMIMO. An efficient HMIMO implementation leverages cost- and energy-efficient metasurfaces, reducing the number of required RF chains compared to conventional full-digital MIMO. Shlezinger [Shl21] designed a metasurface-based antenna for generating holographic waveforms, highlighting the trade-off between flexibility, complexity, and energy consumption. Dai [Dai20] created a 256-element metasurface prototype with 2-bit phase shifting, achieving 19.1 dBi antenna gain at 28.5 GHz. Advanced HMIMO designs often use multi-layer architectures resembling neural networks to perform signal processing directly in the wave domain, optimizing performance under practical hardware constraints.

Other research's study for example the mutual coupling and advantages that can bring. Mutual coupling in closely packed antenna elements affects the radiation pattern and impedance. Conventional MIMO places antennas at least half a wavelength apart to minimize mutual coupling, limiting array gain to the number of antennas. Recent research suggests exploiting mutual coupling in subwavelength-spaced antennas can achieve super-directivity, significantly increasing array gains [Mar19]. In HMIMO systems, the array gain could reach the square of the number of radiating elements, enhancing coverage without increasing transmit power.

All these studies are done in order to introduce HMIMO into different environments that could even help us on our daily life, for example they can be used for Wireless Transfer Power (WTP) by using metasurfaces, the reception becomes less sensitive to incident wave angle and polarization, leading to improvements in circuit size, beamwidth, and conversion efficiency. Also they can be used in satellite communications to compensate for their severe path loss, a spatially continuous aperture can achieve a high directional gain with a small antenna size [Gon23]. HMIMO can significantly enhance ISAC by providing fine-grained, high-gain beam patterns, the large number of antennas in HMIMO systems allows for better resource allocation and more efficient utilization of the shared hardware platform, leading to improved overall system performance. [An23b]. And HMIMO will have an impact in a lot of other environments.



Figure 2.9: Future applications of HMIMO in 6G

In this project we will focus the studies in the capacity for ELAAs using optimal precoders that maximizes the capacity in environment CSI, meaning that the transmitter will know the

channel. We will take a close look at the effect of having different number of polarizations at the transmitter and how it affects to the system, focusing in study the number of active modes available at different points in the space, which has not been previously studied in a extensive way.

Chapter 3

Effect of polarization on ELAAs: an asymptotic Study

In this section, we introduce a comprehensive channel model under multiple orthogonal polarizations and study the capacity of the capacity of ELAAs and the optimization of precoders in the given scenario. We start by outlining the scenario, detailing the assumptions and conditions that define our study. This sets the stage for understanding ELAA behavior and performance under various conditions.

Following the scenario presentation, we delve into the theoretical framework for analyzing ELAA capacity, examining fundamental principles and key performance factors. Next, we explore optimal precoders, crucial for maximizing signal transmission efficiency. We discuss methods to determine these optimal precoders, considering ELAA-specific requirements and constraints. We study the modes activated by these precoders, providing insights into their contribution to overall system performance, and analyze mode distribution and utilization, highlighting their impact on capacity and efficiency.

Additionally, we investigate all this precoder parameters in the holographic asymptotic regime, when the number of antenna elements and the distance between the elements tend to 0, emulating a radiative surface as in HMIMO, considering system behavior as it scales to infinity. The used approximation is also valid when the number of antenna elements is not that high. This analysis helps in understanding long-term performance and scalability of ELAAs based in some analytical formulas.

By the end of this section, we aim to provide a thorough understanding of the theoretical aspects of ELAA capacity, optimal precoder design, and system behavior in asymptotic conditions. This theoretical foundation is essential for guiding future research and development in large-scale antenna systems.

3.1 Near Field Properties

In antenna theory, it is crucial to distinguish between the near field and the far field. The near field is where the wavefront is spherical, whereas the far field is characterized by a planar wavefront. Understanding this distinction is fundamental for analyzing antenna behavior and performance. Let us explain how these regions are distinguished and their particularities.

The near field is the closer region to the transmitter antenna, it can be divided in two regions: the reactive near field and the radiative near field. The reactive near field starts from the surface of the antenna and continues to d_N . In this region, the power decreases inversely proportional to the distance raised to a power higher than 2, making the field behavior more complex. For extremely large antenna arrays, the reactive near-field ends approximately at d_N .

$$d_N = 0.62 \frac{\sqrt{D^3}}{\lambda} \quad (3.1)$$

Where D is the antenna's largest dimension. The radiative near-field (Fresnel region), also known as Fresnel region, begins after the reactive near-field and covers the distance between d_N and d_F , where the far field begins. In the radiative the power decrease inversely proportional to the distance at the power of 2. This d_F distance is called the Fraunhofer distance or Rayleigh distance and is approximated by the equation:

$$d_F = \frac{2D^2}{\lambda} \quad (3.2)$$

This is the distance beyond which the radiated spherical waves can be viewed as approximately planar because the phase difference between the waves from the antenna's center and edge is smaller than $\frac{\pi}{8}$ at the observation point.

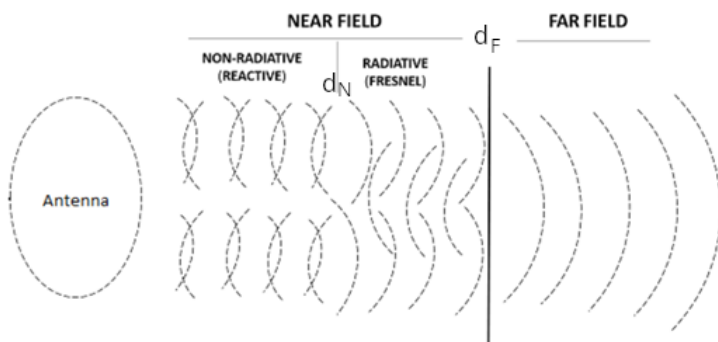


Figure 3.1: Near Field and Far field

This Fraunhofer distance is still relatively small if we make some calculations even considering large frequencies, specially due to the fact that maximum length of antennas tend to be small

as well. Due to the fact that Fraunhofer distance is small the near-field has been overlooked by communication community, but this will not be the case for 6G when working with ELAAs.

3.1.1 Near-Field Properties for ELAAs

The Fraunhofer distance is often defined as the distance that separates the wavelength-dependent limit between the near-field and far-field of a single antenna. This distance is not relevant in our context since we are not considering the far field behaviors. Let's take a closer look on why when working with ELAAs we need to consider the near-field instead of using the far-field approximation.

Considering each antenna component of the array, the signal received from each of them can be seen as planar in the receiver, but when comparing the different signals of each of the antenna components then the curvature becomes noticeable.

This can be more intuitive to see, when we look otherwise, we use one transmitter and an ELAA as a receiver, considering channel reciprocity we know that this effect can be seen on both directions. On the Figure ?? we can see a visual representation about it.

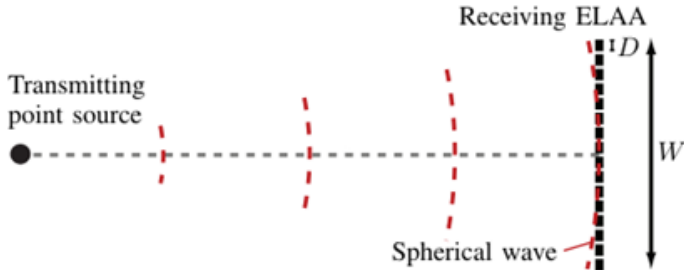


Figure 3.2: Wavefront seeing from an ELAA.

An ELAA contain many small antennas that each one is small but the maximum dimension of the ELAA (W) becomes bigger, making that between different elements on the ELAA separated, there's a phase difference on the wave received, meaning that the defined previously as Fraunhofer distance where the phase variation is lower than $\frac{\pi}{8}$ is no longer accomplished. Usually this new Fraunhofer distance, since we assume planar array antennas, can be calculated as the diagonal of the ELAA, so the Rayleigh distance will continue to be calculated equally as before (7) but considering W instead of D .

$$d_F = \frac{2W^2}{\lambda} \quad (3.3)$$

That's one of the reasons, for ELAAs this Fraunhofer distance d_F will be much bigger meaning that we can no longer assume far field, and we will need to consider near field as well since we

are not surpassing anymore the Fraunhofer distance mentioned.

Another reason is related to ELAAs geometry, the geometric properties of ELAAs, such as their size, shape, and configuration, play a more significant role in determining their behavior than the Fraunhofer distance. Understanding these properties and their interaction with electromagnetic waves is essential for accurate modeling and analysis of antenna arrays.

On the other hand, we need to consider the fact that the combined radiation pattern of the array is not merely a sum of the individual antenna patterns, but a complex result of the interference and phase relationships between these elements. Each antenna element in the array contributes to the overall radiation pattern, and the constructive or destructive interference between the waves emitted by these elements can significantly alter the pattern's shape and directionality. This phenomenon is highly dependent on the relative phases and amplitudes of the signals fed to each antenna element, as well as the physical arrangement of the elements themselves.

The conventional far-field approximation, while suitable for smaller arrays, fails to accurately capture the behavior of ELAAs, leading to significant errors in channel gain estimation. Therefore, considering the near-field properties of ELAAs is essential for obtaining reliable results in communication systems and other applications.

3.2 Scenario Description

First, we will review some near field properties and particularize them for the case of ELAAs, which will help us to recognize the importance of considering the near field instead of assuming the far field when working with antenna arrays.

We can assume the scenario where we have a transmitting ELAA with $(2M+1)$ antenna elements, each one of them formed with three orthogonal dipoles and a receiver antenna also formed with three orthogonal dipoles. Each of the antenna elements from the transmitted are separated a distance vector \mathbf{r}_m from the receiver, where m is the m th antenna element. We can see a representation of that scenario on the following Figure 3.3, note that this scenario in some cases will present a variation where we will have a double polarization at the transmitter side instead of a full polarization [AA24].

Considering this scenario, the vector distance from m th transmit antenna element and the receive antenna is given by:

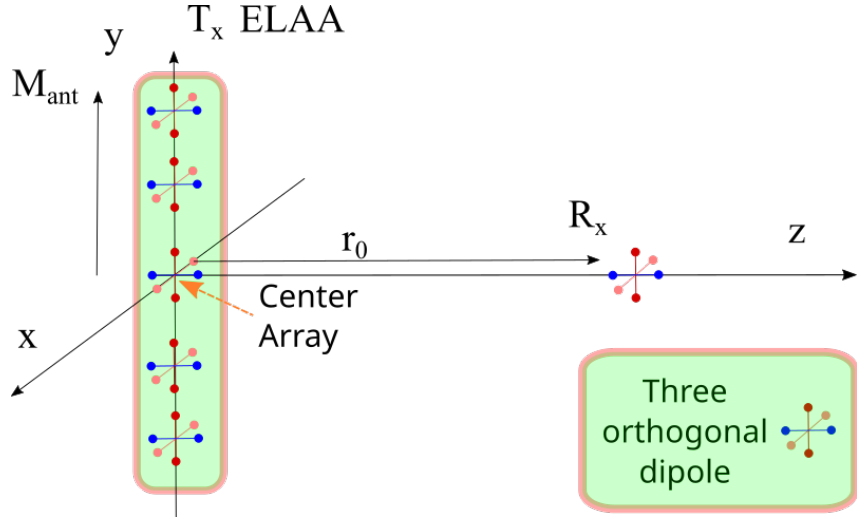


Figure 3.3: Scenario followed of an antenna array transmitter and a receiver with each of antenna and antenna elements is a three orthogonal dipole.

$$\mathbf{r}_m = \begin{pmatrix} 0 \\ m\Delta_T \\ 0 \end{pmatrix} - \begin{pmatrix} 0 \\ D \sin(\theta) \\ D \cos(\theta) \end{pmatrix} \quad (3.4)$$

We can also calculate the distance from the element on the antenna array to the receiver:

$$r_m^2 = \mathbf{r}_m^H \mathbf{r}_m = m^2 \Delta_T^2 + D^2 - 2m\Delta_T D \sin \theta = (m\Delta_T - D \sin \theta)^2 + D^2 \cos^2 \theta \quad (3.5)$$

And, the unitary vector from the element on the antenna array to the receiver antenna can be expressed as:

$$\hat{\mathbf{r}}_m = \frac{1}{r_m} \mathbf{r}_m \quad (3.6)$$

where θ is the elevation angle and Δ_T is the separation between antenna elements. The Green function allows to characterize the channel between a transmitter antenna and a receiver as:

$$\mathbf{H}_m = \frac{j\eta}{2\lambda r_m} \exp\left(-j\frac{2\pi}{\lambda} r_m\right) \mathbf{Q} \mathcal{H}_m = \frac{\xi}{\lambda r_m} \exp\left(-j\frac{2\pi}{\lambda} r_m\right) \mathbf{Q} \mathcal{H}_m \quad (3.7)$$

Where ξ is a complex constant that is proportional to the permittivity of the medium and can be calculated as:

$$\xi = \frac{j\eta}{2}$$

In the above expressions, η is the permittivity of the medium, λ is the signal wavelength, r_m is the modulus of the vector \mathbf{r}_m , \mathbf{Q} is a rotation matrix to model the rotations of the receiver, modeling

the fact that the three receiving dipoles may not be placed along the reference coordinate system. Finally, the matrix \mathcal{H}_m can be calculated as:

$$\mathcal{H}_m = \alpha_m \mathbf{I}_3 - \beta_m \hat{\mathbf{r}}_m \hat{\mathbf{r}}_m^H \quad (3.8)$$

where:

$$\alpha_m = \left(1 + \frac{l\lambda}{2\pi r_m} - \frac{\lambda^2}{(2\pi r_m)^2} \right) \quad (3.9)$$

$$\beta_m = \left(1 + 3 \frac{j\lambda}{2\pi r_m} - 3 \frac{\lambda^2}{(2\pi r_m)^2} \right) \quad (3.10)$$

It can clearly be seen that this rotation matrix does not really affect the capacity of the channel and is essentially superfluous to the discussion in this work, so that we will assume from now on that $\mathbf{Q} = \mathbf{I}_3$.

This matrix can be decomposed as a sum of terms independent of r_m , that are usually referred to as radiative terms and terms that are inversely dependent of r_m that are reactive terms, these reactive terms are usually neglected since they decay rapidly with the distance and become low compared to 1, so they are only considered in the reactive near field. So, from now on we will focus on the radiative terms and completely disregard the reactive near field terms.

3.3 Signal definition from scenario

Continuing from the channel definition and with the same scenario definition as previous, once we have the channel for each of the antenna elements, we need to calculate the channel definition for the whole antenna array. To do that we need to stack all the antenna channels in a matrix. For the case where the number of polarizations are different on the transmitter or the receiver we must select the corresponding entries of the above matrix [AA24]. For the case of a double polarization transmitter we will assume the first polarizations (according to the orientation of the cartesian system of coordinates) are always used, so the corresponding channel model will be:

$$\mathbf{H}_m^{t_{pol} \times r_{pol}} = [\mathbf{H}_m]_{1:r_{pol}, 1:t_{pol}} \quad (3.11)$$

where r_{pol} and t_{pol} are the number of polarizations used at the receiver and transmitter respectively. Considering that we have $2M + 1$ transmit antennas side by side:

$$\mathbf{H}^{(2M+1)t_{pol} \times r_{pol}} = [\mathbf{H}_{-M}^{t_{pol} \times r_{pol}}, \dots, \mathbf{H}_M^{t_{pol} \times r_{pol}}] \quad (3.12)$$

Observe that this matrix can be decomposed as a sum of terms independent of r_m , sometimes referred to as radiative terms, plus terms decaying as $O(r_m^{-2})$ and $O(r_m^{-3})$, sometimes referred to as reactive terms. From now on we will fully disregard these two terms in the channel definition and only consider the term that decays as $O(r_m^{-1})$, so that we will take

$$\mathbf{H}_m = \frac{\xi}{\lambda r_m} \exp\left(-j\frac{2\pi}{\lambda}r_m\right) \mathbf{P}_m^\perp \quad (3.13)$$

where

$$\mathbf{P}_m^\perp = \mathbf{I}_3 - \frac{\mathbf{r}_m \mathbf{r}_m^H}{r_m^2}. \quad (3.14)$$

The next result shows that this can also be done in the holomorphic regime (i.e for an asymptotically large number of antennas that are close together).

It can be demonstrated that regardless of the values of M and Δ_T , and as long as the total dimension of the ULA is kept constant, we can approximate the eigenvalues and left eigenvectors of the channel matrix up to an error term that decays as $O(D^{-4})$ for D large enough and when three polarizations are used at either side of the communications link. In the following section we analyze the asymptotic behavior of this matrix when a large number of transmit antennas is deployed in a fixed distance. This approximation will allow us to obtain certain insights into the finite dimensional problem when several polarizations are used at both transmitter and receiver. Following this channel model, we can describe the received signal as.

$$\mathbf{y} = \mathbf{H}^{t_{pol} \times r_{pol}} \mathbf{s} + \mathbf{n}$$

where $\mathbf{H}^{t_{pol} \times r_{pol}}$ is the channel matrix with dimensions $r_{pol} \times (2M + 1)t_{pol}$, \mathbf{n} is the noise contribution as $\mathbf{n} \sim CN(0, \sigma^2 \mathbf{I}_3)$ and \mathbf{s} is the transmitted signal. In order to maximize the received signal and get the desired behaviour, for example focusing the received signal in a certain point in the space, we can make some preprocess to the bits that are going to be sent by means of a precoding matrix (\mathbf{W}) that will multiplying the signal symbols to sent (\mathbf{x}).

$$\mathbf{y} = \mathbf{H}_m^{t_{pol} \times r_{pol}} \mathbf{W} \mathbf{x} + \mathbf{n}$$

Where s has been separated in two components, where s will be the bits to sent, the raw data that we are going to send and the receiver will need to decode and \mathbf{W} , denote a $(2M + 1)t_{pol} \times r_{pol}$ precoding matrix that transforms the r_{pol} signals intended to the receiver into a set of $(2M + 1)t_{pol}$ signals that are fed to the different transmit antennas.

3.4 Designing the optimum precoder

As previously discussed, a crucial factor in modern communication systems is their ability to serve the maximum number of users at the highest possible bit-rate. A key indicator of a

system's performance is its capacity. Therefore, we aim to calculate the optimum precoder that maximizes this capacity, assuming our ELAA transmitter has knowledge of the transmit channel [AA24].

In this section, we will demonstrate how to calculate the optimum precoder \mathbf{W} that focuses the transmission on a specific spatial region to maximize the system's capacity. By optimizing the precoder, we enhance the system's ability to deliver higher bit-rates and efficiently serve more users.

3.4.1 Designing the optimum precoder for fully polarized transmitter

To calculate that we will come from the basis that we have the explained previous scenario, where the received signal is the following:

$$\mathbf{y} = \mathbf{H}_m^{t_{pol} \times r_{pol}} \mathbf{W} \mathbf{x} + n \quad (3.15)$$

Where \mathbf{W} denote a $(2M+1)t_{pol} \times r_{pol}$ precoding matrix that transforms the t_{pol} signals intended to the receiver into a set of $(2M+1)r_{pol}$ signals that are fed to the different transmit antennas.

From that, if we assume that the intended signals to be transmitted are independent and identically distribute complex standardized Gaussian random variables, we can express the capacity of the system as:

$$C = \log \det \left(\mathbf{I}_{r_{pol}} + \frac{1}{\sigma^2} \mathbf{H}^{t_{pol} \times r_{pol}} \mathbf{W} \mathbf{W}^H \left(\mathbf{H}^{t_{pol} \times r_{pol}} \right)^H \right) \quad (3.16)$$

We will that the precoder is designed to have a total known transmit power equal to $\text{tr}(\mathbf{W} \mathbf{W}^H) = P$.

To calculate this optimum precoder we will consider the singular value decomposition $\mathbf{H}^{t_{pol} \times r_{pol}} = \mathbf{U} \boldsymbol{\Sigma}^{1/2} \mathbf{V}^H$ where matrix of right singular vectors, and $\boldsymbol{\Sigma}^{1/2} \in \mathbb{C}^{r_{pol} \times r_{pol}}$ is a diagonal matrix containing the singular values of $\mathbf{H}^{t_{pol} \times r_{pol}}$. The capacity now can be expressed with this new terms using the fact that $\det(\mathbf{I} + \mathbf{AB}) = \det(\mathbf{I} + \mathbf{BA})$ and that \mathbf{U} is an orthogonal $\mathbf{U}^H \mathbf{U} = \mathbf{I}$ matrix as:

$$C = \log \det \left(I_{r_{pol}} + \frac{1}{\sigma^2} \boldsymbol{\Sigma}^{1/2} \mathbf{V}^H \mathbf{W} \mathbf{W}^H \mathbf{V} \boldsymbol{\Sigma}^{1/2} \right). \quad (3.17)$$

Now we can use the Hadamard inequality to find the optimum precoder. The Hadamard inequality states that the determinant of a positive matrix is upper bounded by the product of its diagonal elements, with equality when the matrix is diagonal:

$$|\det(A)| \leq \prod_{i=1}^n |a_i| \quad (3.18)$$

This implies that the capacity is maximum when $\Sigma^{1/2}\mathbf{V}^H\mathbf{W}\mathbf{W}^H\mathbf{V}\Sigma^{1/2}$ is diagonal, from that we can statethat the optimum precoding matrix should the form $\mathbf{W} = \mathbf{V}\mathcal{P}^{1/2}$ where $\mathcal{P}^{1/2}$ is a diagonal matrix with positive coefficients $\sqrt{p_1}, \dots, \sqrt{p_{r_{pol}}}$. This diagonal elements from the matrix $\mathcal{P}^{1/2}$ can be understand as the power distribution for each of the channels that are available. For our case, to simplify the equations we have assumed that $\mathbf{V}^H\mathbf{V} = \mathbf{I}$)

$$C = \log \det \left(\mathbf{I}_{r_{pol}} + \frac{1}{\sigma^2} \Sigma^{1/2} \mathcal{P} \Sigma^{1/2} \right) = \log \det \left(\mathbf{I}_{r_{pol}} + \frac{1}{\sigma^2} \mathcal{P} \Sigma \right). \quad (3.19)$$

Now, it remains to find the coefficients $p_1, \dots, p_{r_{pol}}$ that maximize

$$p_1, \dots, p_{r_{pol}} = \arg \max_{p_1, \dots, p_{r_{pol}}} \log \det \left(\mathbf{I}_{r_{pol}} + \frac{1}{\sigma^2} \mathcal{P} \Sigma \right) \quad (3.20)$$

subject to all this elements are positive ($p_j > 0$) and (that the total transmitted power is the previous known value mentioned) $\text{tr}(\mathcal{P}) = P$ (this constraint follows from the fact that $\text{tr}(\mathbf{W}\mathbf{W}^H) = P$). Let $\rho_1 \geq \rho_2 \geq \dots \geq \rho_{r_{pol}}$ denote the diagonal elements of Σ , in such away that they are ordered from the biggest to the smallest, so the first channel will have the maximum power and the last one the smallest.

To solve this optimization power we can state the Lagrangian to the problem as

$$\mathcal{L} = \sum_{j=1}^{r_{pol}} \log \left(1 + \frac{1}{\sigma^2} \rho_j p_j \right) + \sum_{j=1}^{r_{pol}} \lambda_j p_j + \lambda_{r_{pol}+1} \left(P - \sum_{j=1}^{r_{pol}} p_j \right). \quad (3.21)$$

Taking derivatives with respect to p_i and forcing the result to zero we obtain the following spell out Karush-Khun-Tucker (KKT) conditions:

$$\begin{aligned} \frac{\rho_i}{\sigma^2 + \rho_i p_i} + \lambda_i - \lambda_{r_{pol}+1} &= 0 \\ \lambda_j p_j &\geq 0 \\ \lambda_{r_{pol}+1} \left(P - \sum_{j=1}^{r_{pol}} p_j \right) &\geq 0. \end{aligned} \quad (3.22)$$

To calculate the p_i values, now we will create a subset (\mathcal{I}) of indexes $i \in \{1, \dots, r_{pol}\}$ such that $p_i > 0$ for $i \in \mathcal{I}$ (note that the second inequality is strict in order to maximize the values), so for this cases where $p_i > 0$ implies that $\lambda_i = 0$ for $i \in \mathcal{I}$ and otherwise when $p_i = 0$ will be $\lambda_i > 0$ and therefore for the subset of positive values of p_i from the first inequality we can see that:

$$\frac{\rho_i}{\sigma^2 + \rho_i p_i} = \lambda_{r_{pol}+1} \quad (3.23)$$

for all $i \in \mathcal{I}$. This shows that in this subset of indexes

$$\alpha_i = \frac{1}{\lambda_{r_{pol}+1}} - \frac{\sigma^2}{\rho_i} > 0. \quad (3.24)$$

Observe that since $\rho_1 \geq \rho_2 \geq \dots \geq \rho_{r_{\text{sat}}}$ from the above equation one must have $p_1 \geq p_2 \geq \dots \geq p_{r_{\text{pol}}}$. This shows that $\mathcal{I} = \{1, 2, \dots, n_+\}$ for a certain n_+ between 1 and r_{pol} and

$$p_i = \left[\frac{1}{\lambda_{r_{\text{pol}}+1}} - \frac{\sigma^2}{\rho_i} \right]^+ \quad (3.25)$$

where $[\cdot]^+ = \max(\cdot, 0)$. The value of $\lambda_{r_{\text{pol}}+1}$ is obtained by forcing

$$P = \sum_{j=1}^{r_{\text{pol}}} p_j = \sum_{i=1}^{n_+} \left[\frac{1}{\lambda_{r_{\text{pol}}+1}} - \frac{\sigma^2}{\rho_i} \right]^+ \quad (3.26)$$

This is usually referred to as the waterfilling solution, which is solved in practice as follows. Find the maximum value of $n_+ = 1, 2, \dots$ such that

$$\frac{1}{n_+} P + \frac{1}{n_+} \sum_{i=1}^{n_+} \frac{\sigma^2}{\rho_i} = \frac{1}{\lambda_{r_{\text{pol}}+1}} > \frac{\sigma^2}{\rho_{n_+}} \quad (3.27)$$

(note that the equation always holds for $n_+ = 1$). Having found this n_+ , fix $\lambda_{r_{\text{pol}}+1}^{-1} = \frac{1}{n_+} P + \frac{1}{n_+} \sum_{i=1}^{n_+} \frac{\sigma^2}{\rho_i}$ and $p_i = \left[\frac{1}{\lambda_{r_{\text{pol}}+1}} - \frac{\sigma^2}{\rho_i} \right]^+$. To calculate the case where two polarizations are being used instead of a fully polarized transmitted we will need to just adjust the channel by selecting the columns corresponding polarizations.

3.5 Asymptotic behaviour of the channel eigenvalues

Holographic MIMO is an advanced wireless communication technology that leverages holographic principles, that involve precisely shaping and directing electromagnetic waves using interference patterns and dense antenna arrays to optimize signal transmission and reception. It uses dense arrays of tiny, closely spaced antennas to create and manipulate electromagnetic waves in highly precise ways, enabling improved spatial resolution and signal focusing. This technology can dynamically shape and direct beams, leading to significant increases in data rates, spectral efficiency, and network capacity.

In holographic MIMO, the trend is to make antenna array elements smaller and fit more of them into the same space. This approach involves packing more and more tiny antennas into a given area, which allows for more precise control over the electromagnetic wavefronts. By having a larger number of smaller elements, the system can achieve finer spatial resolution and improve their beamforming capabilities. By taking this principle to the extreme, this progression aims to create a radiative surface with an infinite number of antenna elements, effectively turning the entire surface into a highly efficient and dynamic array that can manipulate and direct radio waves with unprecedented accuracy. So, in this section we aim to study theoretically this behaviour and make an asymptotic approximation to have some closed expressions to calculate

the channel parameters for the ELAAs without requiring to work with big matrices that will lead to high computational cost.

Let's consider the asymptotic scenario where the total number of elements in the array increases indefinitely ($M \rightarrow \infty$) while the distance between consecutive elements shrinks to zero ($\Delta_T \rightarrow 0$) such that the overall aperture dimension approaches a constant value $M\Delta_T \rightarrow d$. Our main goal is to examine the matrix $\mathcal{W}^{t_{\text{pol}} \times r_{\text{pol}}}$ as defined below, since the other terms tend to uniformly approach zero rapidly for reasonable values of D , where D represents the distance from the center of the antenna array to the receiver. More specifically, we will consider the asymptotic behavior of the following matrix.

$$\mathcal{W}^{t_{\text{pol}} \times r_{\text{pol}}} = \left| \frac{\lambda}{\xi} \right|^2 \frac{1}{2M+1} \mathbf{H}^{t_{\text{pol}} \times r_{\text{pol}}} \left(\mathbf{H}^{t_{\text{pol}} \times r_{\text{pol}}} \right)^H$$

It can be seen that this matrix is the one that dictates the behavior of the power allocation algorithm above. In other words, this matrix alone determines how many spatial modes (multiplexed streams) can be active at each point of the space. In this section, we will present the asymptotic behavior for this matrix and the next section, we will present closed forms for its eigenvalues to compare them.

Before analysing the asymptotic behaviour we will make some previous considerations in terms of the formal assumptions that are needed to formulate the corresponding results.

3.5.1 Previous considerations

We will assume that the transmit power P is scaled down as the number of transmit antennas increases, so as to keep a bounded signal to noise ratio at the receive side. More specifically, we will assume that [AA24]

$$P = \frac{\bar{P}}{(2M+1)t_{\text{pol}}} \quad (3.28)$$

where \bar{P} is a fixed constant independent of the number of transmit elements of the uniform linear array. We define SNR_M as the signal to noise ratio that is observed at the receiver when the transmitter uses the optimum beamformer with $2M+1$ antennas. In other words, if we fix $p_1 = P$ and $p_2 = p_3 = 0$, and assume that the optimum beamformer is used. which corresponds to the principal right singular vector of $\mathbf{H}^{t_{\text{pol}} \times r_{\text{pol}}}$, leading to

$$\begin{aligned} \text{SNR}_M &= \frac{P}{\sigma^2} \lambda_{\max} \left[\mathbf{H}^{t_{\text{pol}} \times r_{\text{pol}}} \left(\mathbf{H}^{t_{\text{pol}} \times r_{\text{pol}}} \right)^H \right] \\ &= \frac{\bar{P}}{\sigma^2 t_{\text{pol}}} \left| \frac{\xi}{\lambda} \right|^2 \lambda_{\max} \left[\frac{1}{(2M+1)} \sum_{m=M}^M \frac{1}{r_m^2} \text{tr} \left[\left[\mathbf{P}_m^\perp \right]_{1:r_{\text{pol}}, 1:t_{\text{pol}}} \left[\mathbf{P}_m^\perp \right]_{1:r_{\text{pol}}, 1:t_{\text{pol}}}^\parallel \right] \right] \end{aligned} \quad (3.29)$$

where $\lambda_{\max}(\cdot)$ denotes the maximum eigenvalue and where

$$\mathbf{P}_m^\perp = \frac{1}{r_m^2} \begin{bmatrix} r_m^2 & 0 & 0 \\ 0 & (D \cos \theta)^2 & \frac{1}{r_m^2} (m\Delta_T - D \sin \theta) D \cos \theta \\ 0 & (m\Delta_T - D \sin \theta) D \cos \theta & r_m^2 - (D \cos \theta)^2 \end{bmatrix}. \quad (3.30)$$

Let us now introduce the definitions

$$\begin{aligned} s_M^{(k)} &= \frac{1}{2M+1} \sum_{m=M}^M \frac{1}{r_m^k} (k \text{ even }) \\ s_M^{(k)} &= \frac{1}{2M+1} \sum_{m=M}^M \frac{(m\Delta_T - D \sin \theta)}{r_m^{k+1}} (k \text{ odd }) \end{aligned} \quad (3.31)$$

It can be shown that (assuming $r_{\text{pol}} = 3$) we have

$$\text{SNR}_M = \frac{\bar{P}}{\sigma^2 t_{\text{pol}}} \left| \frac{\xi}{\lambda} \right|^2 s_M^{(2)}. \quad (3.32)$$

It is shown below that under the holomorphic regime this converges to

$$\text{SNR} = \frac{\bar{P}}{\sigma^2 t_{\text{pol}}} \left| \frac{\xi}{\lambda} \right|^2 \psi_2 \quad (3.33)$$

where

$$\psi_2 = \begin{cases} \frac{1}{2dD \cos \theta} \arctan \left(\frac{2Dd \cos \theta}{D^2 - d^2} \right) & d < D \\ \frac{1}{2dD \cos \theta} \pi / 2 & d = D \\ \frac{1}{2dD \cos \theta} \left[\pi + \arctan \left(\frac{2Dd \cos \theta}{D^2 - d^2} \right) \right] & d > D. \end{cases} \quad (3.34)$$

Observe that SNR decays as the square of the distance D , in the sense that (for the case $D > d$) we have

$$\psi_2 = \frac{1}{D^2} \frac{1}{2 \left(\frac{d}{D} \right) \cos \theta} \arctan \left(\frac{2 \frac{d}{D} \cos \theta}{1 - \left(\frac{d}{D} \right)^2} \right) \quad (3.35)$$

where $\frac{d}{D}$ can be seen as a constant.

Let us now analyse the asymptotic behaviour of the channel eigenvalues. First, we will be studying the matrix $\mathcal{W}^{t_{\text{pol}} \times r_{\text{pol}}}$ when the number of elements of array tends to infinity ($M \rightarrow \infty$) and the distance between consecutive elements tends to zero ($\Delta_T \rightarrow 0$), we will call the length aperture d and D the distance from the center of the ELAA transmitter to the receiver.

3.5.2 Fully polarized transmitter

We analyze here the scenario with a fully polarized transmitter and receiver is ($t_{\text{pol}} = r_{\text{pol}} = 3$) Using the conventional definition of the Riemannian integral, one can prove that under the

conditions $M \rightarrow \infty$ while $\Delta_T \rightarrow 0$ and $M\Delta_T \rightarrow d$ the matrix $\mathcal{W}^{r_{\text{pol}} \times r_{\text{pol}}}$ converges to $\bar{\mathcal{W}}^{3 \times 3}$ [Agu23]:

$$\bar{\mathcal{W}}^{3 \times 3} = \begin{pmatrix} \psi_2 & 0 & 0 \\ 0 & \psi_4 D^2 \cos^2 \theta & -\psi_3 D^2 \cos^2 \theta \\ 0 & -\psi_3 D^2 \cos^2 \theta & \psi_2 - \psi_4 D^2 \cos^2 \theta \end{pmatrix} \quad (3.36)$$

where ψ_2 has been presented before and where:

$$\begin{aligned} \psi_3 &= -\frac{D \sin(\theta)}{(D^2 + d^2)^2 - (2dD \sin \theta)^2} \\ \psi_4 &= \frac{1}{2} \frac{1}{(D \cos \theta)^2} \frac{(D^2 + d^2) - 2D^2 \sin^2 \theta}{(D^2 + d^2)^2 - (2dD \sin \theta)^2} + \frac{\psi_2}{2(D \cos \theta)^2} \end{aligned} \quad (3.37)$$

Proof. We observe that when $t_{\text{pol}} = r_{\text{pol}} = 3$ the matrix $\mathcal{W}^{t_{\text{pol}} \times r_{\text{pol}}}$ takes the form

$$\mathcal{W}^{t_{\text{pol}} \times r_{\text{pol}}} = \frac{1}{2M+1} \sum_{m=-M}^M \frac{1}{r_m^2} \mathbf{P}_m^\perp = \begin{bmatrix} s_M^{(2)} & 0 & 0 \\ 0 & s_M^{(4)} D^2 \cos^2 \theta & s_M^{(3)} D \cos \theta \\ 0 & s_M^{(3)} D \cos \theta & s_M^{(2)} - s_M^{(4)} D^2 \cos^2 \theta \end{bmatrix}$$

where we have used the fact that $r_m^2 = (m\Delta_T - D \sin \theta)^2 + D^2 \cos^2 \theta$ and where $s_M^{(k)}$ is defined in (3.31). Therefore, we only need to show that $s_M^{(k)} \rightarrow \psi_k$ for $k = 2, 3, 4$.

The case $k = 2$ is the easiest to handle, since the definition of Riemann integral directly implies that we can write

$$\begin{aligned} \frac{1}{2M+1} \sum_{m=-M}^M \frac{1}{r_m^2} &= \frac{1}{2M+1} \sum_{m=-M}^M \frac{1}{(m\Delta_T - D \sin \theta)^2 + D^2 \cos^2 \theta} \\ &= \frac{1}{(2M+1)\Delta_T} \int_{-M\Delta_T}^{M\Delta_T} \frac{1}{(x - D \sin \theta)^2 + D^2 \cos^2 \theta} dx + o(1) \\ &= \frac{1}{2dD \cos \theta} \left[\arctan \left(\frac{d + D \sin \theta}{D \cos \theta} \right) + \arctan \left(\frac{d - D \sin \theta}{D \cos \theta} \right) \right] + o(1) \\ &= \psi_2 + o(1). \end{aligned}$$

Observe that last identity follows from the identity

$$\arctan a + \arctan b + i\pi = \arctan \left(\frac{a+b}{1-ab} \right)$$

for some $i \in \mathbb{Z}$ that is adjusted so that the left hand side falls within $(-\pi/2, \pi/2)$ and where a and b are defined as the arguments of the two arctangents in the above equation. In our case, we have $a > 0$ and

$$ab = \frac{d^2 - D^2}{D^2 \cos^2 \theta} + 1$$

so that $ab > 1$ if and only if $d > D$. Hence, we reason as follows. If $d = D$, we have $ab = 1$ so these two variables have the same sign and $\arctan a + \arctan b = \pi/2$. If $d < D$ we have $ab < 1$ and one can see that the above formula holds with $i = 0$. If $d > D$, we have $ab > 1$ one must have $b > 0$ so that $a > 1/b$ so that $\arctan a + \arctan b > \pi/2$. As a consequence, we need $i = -1$ in the above equation.

The case $k = 4$ is very similar, in the sense that the definition of Riemann integral directly leads to

$$\begin{aligned} \frac{1}{2M+1} \sum_{m=-M}^M \frac{1}{r_m^4} &= \frac{1}{(2M+1)\Delta_T} \int_{-M\Delta_T}^{M\Delta_T} \frac{1}{((x-D\sin\theta)^2 + D^2\cos^2\theta)^2} dx + o(1) \\ &= \psi_4 + o(1) \end{aligned}$$

where we have used the fact that [Gradystein, 2.148]

$$\int \frac{1}{(1+y^2)^2} dy = \frac{1}{2} \frac{y}{(1+y^2)} + \frac{1}{2} \arctan y$$

Finally, the case $k = 3$ is solved similarly,

$$\begin{aligned} \frac{1}{2M+1} \sum_{m=-M}^M \frac{1}{r_m^3} &= \frac{1}{(2M+1)\Delta_T} \int_{-M\Delta_T}^{M\Delta_T} \frac{(x-D\sin\theta)}{((x-D\sin\theta)^2 + D^2\cos^2\theta)^2} dx + o(1) \\ &= \psi_3 + o(1) \end{aligned}$$

where we have used

$$\int \frac{2y}{(1+y^2)^2} dy = -\frac{1}{1+y^2}$$

At high values of the signal to noise ratio, the achievable rate essentially depends on the determinant of the channel matrix, which can be well approximated as $\det \bar{\mathbf{W}}^{(t_{\text{pol}} \times r_{\text{pol}})}$ according to the above reasoning. This implies that one can try to optimize the system parameters to provide the optimum rate at high SNR. In our case, one can easily find a closed form solution to the above determinant, which is given by

$$\det \bar{\mathcal{W}}^{t_{\text{pol}} \times r_{\text{pol}}} = \frac{\psi_2}{4} \left(\psi_2^2 - \frac{1}{(D^2+d^2)^2 - (2dD)^2 \sin^2\theta} \right) = \frac{\psi_2}{4} \left(\psi_2^2 - \frac{1}{(D^2-d^2)^2 + (2dD\cos\theta)^2} \right)$$

Since $\psi_2 > 0$ by definition we have $\det \bar{\mathcal{W}}^{t_{\text{pol}} \times r_{\text{pol}}} > 0$ if and only if the second term of the above product is positive. Indeed, when $d = D$ the above determinant becomes equal to

$$\det \bar{\mathcal{W}}^{(t_{\text{pol}} \times r_{\text{pol}})} = \frac{\psi_2}{4} \frac{(\pi/2)^2 - 1}{(2D^2)^2 \cos^2\theta} > 0.$$

When $d < D$ we may use the fact that

$$\psi_2^2 - \frac{1}{(D^2-d^2)^2 + (2dD\cos\theta)^2} = \frac{f\left(\frac{2dD\cos\theta}{D^2-d^2}\right)}{(2dD\cos\theta)^2}$$

where $f(x) = \arctan^2(x) - \frac{x^2}{1+x^2} > 0$, proving that $\det \bar{\mathcal{W}}^{(t_{\text{pol}} \times r_{\text{pol}})} > 0$, and a similar reasoning can be made when $d > D$.

Up to a multiplicative factor D^{-6} , $\det \bar{\mathcal{W}}^{(t_{\text{pol}} \times r_{\text{pol}})}$ is a function of the only two variables d/D and θ , implying that there might exist a finite optimum value of d/D for a given elevation angle θ .

3.5.3 Double polarization transmitter

Now, we can analyze the situation where the transmitter only employs two orthogonal polarizations [Agu23], so that $t_{\text{pol}} = 2$ and $r_{\text{pol}} = 3$. Using the conventional definition of the Riemanni under the same conditions as in the case $t_{\text{pol}} = r_{\text{pol}} = 3$ ($M \rightarrow \infty$ while $\Delta_T \rightarrow 0$ and $M\Delta_T \rightarrow d$ ($d \neq D$)) the matrix $\mathcal{W}^{r_{\text{pol}} \times r_{\text{pol}}}$ converges to $\bar{\mathcal{W}}^{2 \times 3}$:

$$\bar{\mathcal{W}}^{2 \times 3} = \begin{pmatrix} \psi_2 & 0 & 0 \\ 0 & \psi_6(D \cos \theta)^4 & \psi_5(D \cos \theta)^3 \\ 0 & \psi_5(D \cos \theta)^3 & \psi_4(D \cos \theta)^2 - \psi_6(D \cos \theta)^4 \end{pmatrix} \quad (3.38)$$

Where ψ_2 has been presented before and:

$$\begin{aligned} \psi_s &= \frac{(D^2 + d^2) D \sin \theta}{((D^2 + d^2)^2 - (2dD \sin \theta)^2)^2} \\ \psi_6 &= \frac{1}{4} \frac{1}{(D \cos \theta)^2} \frac{((D^2 + d^2)^2 - 4D^4 \sin^2 \theta)}{((d^2)^2 - (2dD \sin \theta)^2)^2} \\ &\quad + \frac{3}{8} \frac{1}{(D \cos \theta)^4} \left[\frac{(D^2 + d^2)^2 - 2D^2 \sin^2 \theta}{((D^2 + d^2)^2 - (2dD \sin \theta)^2)} + \psi_2 \right] \\ &= \frac{1}{4} \frac{1}{(D \cos \theta)^2} \left[\frac{((D^2 + d^2)^2 - 4D^4 \sin^2 \theta)}{((D^2 + d^2)^2 - (2dD \sin \theta)^2)^2} + 3\psi_4 \right] \end{aligned} \quad (3.39)$$

Proof. The proof follows the same approach as the proof of Proposition 2. From the definition of $\mathcal{W}^{2 \times 3}$ we can write

$$\begin{aligned} \mathcal{W}^{2 \times 3} &= \begin{bmatrix} s_M^{(2)} & 0 & 0 \\ 0 & (D \cos \theta)^4 s_M^{(6)} & (D \cos \theta)^3 s_M^{(5)} \\ 0 & (D \cos \theta)^3 s_M^{(5)} & (D \cos \theta)^2 s_M^{(4)} - (D \cos \theta)^4 s_M^{(6)} \end{bmatrix} \\ &= \frac{1}{2M+1} \sum_{m=-M}^M \frac{1}{r_m^2} \begin{bmatrix} 1 & 0 \\ 0 & \frac{D^2 \cos^2 \theta}{r_m^2} \\ 0 & \frac{D \cos \theta (m\Delta_T - D \sin \theta)}{r_m^2} \end{bmatrix} \begin{bmatrix} 1 & 0 & 0 \\ 0 & \frac{D^2 \cos^2 \theta}{r_m^2} & \frac{D \cos \theta (m\Delta_T - D \sin \theta)}{r_m^2} \end{bmatrix} \end{aligned} \quad (3.40)$$

where we have used the definitions previously. Therefore, we only need to show that $s_M^{(5)} \rightarrow \psi_5$ and $s_M^{(6)} \rightarrow \psi_6$, using the definition of Riemann integral. Regarding the first, one can readily see that

$$\begin{aligned} s_M^{(5)} &= \frac{1}{2M+1} \sum_{m=-M}^M \frac{(m\Delta_T - D \sin \theta)}{\left((m\Delta_T - D \sin \theta)^2 + (D \cos \theta)^2\right)^3} \\ &= \frac{1}{(2M+1)\Delta_T} \int_{-M\Delta_T}^{M\Delta_T} \frac{(x - D \sin \theta)}{\left((x - D \sin \theta)^2 + (D \cos \theta)^2\right)^3} dx + o(1) \\ &= \psi_S + o(1) \end{aligned} \quad (3.41)$$

where we have used the fact that

$$\int \frac{y}{(1+y^2)^3} dy = -\frac{1}{4} \frac{1}{(1+y^2)^2}. \quad (3.42)$$

Regarding $s_M^{(6)}$, we have

$$\begin{aligned} s_M^{(6)} &= \frac{1}{2M+1} \sum_{m=-M}^M \frac{1}{\left((m\Delta_T - D \sin \theta)^2 + (D \cos \theta)^2\right)^3} \\ &= \frac{1}{(2M+1)\Delta_T} \int_{-M\Delta_T}^{M\Delta_T} \frac{1}{\left((x - D \sin \theta)^2 + (D \cos \theta)^2\right)^3} dx + o(1) \\ &= \psi_6 + o(1) \end{aligned} \quad (3.43)$$

$$\int \frac{1}{(1+y^2)^3} dy = \frac{1}{4} \frac{y}{(1+y^2)^2} + \frac{3}{8} \left[\frac{y}{1+y^2} + \arctan y \right]. \quad (3.44)$$

Here, as before, it is interesting to investigate the determinant of $\bar{W}^{2 \times 3}$ in order to establish the multiplexing order of the system with only two polarizations at the transmitter. In this case, we can see the expression of the determinant becomes more complicated, although it can be analyzed in a similar way.

This matrices can be very useful to help us calculate some parameters for example the number of activation nodes in one point, this way the calculus becomes simpler and we don't require to solve process with the waterfilling process explained before, that will require large memory to store big matrices for the channel and others and as the number of antennas increases, the resources needed for the calculation increases also highly.

3.6 Activation of different transmit modes

Now, we will be calculating the number of activation modes for each of the above cases (fully polarized transmitter and case of double polarization at the transmitter side). The maximum number of activation of modes activated can be directly related to the maximum number of parallel streams between the transmitter and receiver that we can have. This can be directly

related to the Shannon theorem explained before that establishes that the maximum number of streams in MIMO systems, is determined by the minimum of the number of transmit antennas (M_t) and receive antennas (M_r). In this case with the scenario that we have this number will be determined by the number of polarizations of the receiver .

The number of active modes will be directly related to the distance, since if we increase the distance the SNR at the receiver will be lower as well and as we will see the number of active modes will decrease as well.

To calculate this values we will be using the approximations of the $\mathcal{W}^{t_{\text{pol}} \times r_{\text{pol}}}$ matrices that we have previously seen in order to obtain it's eigenvalues and finally calculate the active modes from them.

The number of modes that are being activated for each channel depends on the eigenvalues of $\mathbf{H}^{t_{\text{pol}} \times r_{\text{pol}}} (\mathbf{H}^{t_{\text{pol}} \times r_{\text{pol}}})^H$, which we denoted previously as $\rho_1 \geq \rho_2 \geq \dots \geq \rho_{r_{\text{pol}}}$, so we will see them ordered in the diagonal, we can see this eigenvalues as the power distribution between each one of the channels. It can easily seen that as ($M \rightarrow \infty$) the eigenvalues of $\mathbf{H}^{t_{\text{pol}} \times r_{\text{pol}}} (\mathbf{H}^{t_{\text{pol}} \times r_{\text{pol}}})^H$ increase in magnitude, so that the overall capacity increases in magnitude as well, this effect is consequence of the fact that the availability of CSI at the transmitter allows to focus the energy in a certain spatial region. In order to analyze the asymptotic behavior of the capacity using again the holomorphic limit ($M \rightarrow \infty, \Delta_T \rightarrow 0, M\Delta_T \rightarrow d, 0 < d < \infty$) we need to scale down the total transmit power as the number of transmitters grows without bound. To that effect, we will assume that we fix the total transmitted power according to:

$$P = \frac{\bar{P}}{(2M+1)t_{\text{pol}}}. \quad (3.45)$$

Using the definition of SNR_M above, we can rewrite $\frac{\bar{P}}{\sigma^2 t_{\text{pol}}} |\frac{\varepsilon}{\lambda}|^2 s_M^{(2)}$

$$\begin{aligned} C &= \max_{\text{tr}(\mathbf{WW}^H)=P} \log \det \left(\mathbf{I}_{r_{\text{pol}}} + \frac{1}{\sigma^2} \mathbf{H}^{t_{\text{pol}} \times r_{\text{pol}}} \mathbf{W} \mathbf{W}^H (\mathbf{H}^{t_{\text{pol}} \times r_{\text{pol}}})^H \right) \\ &= \max_{\text{tr}(\mathbf{WW}^H)=\text{SNR}_M} \log \det \left(\mathbf{I}_{r_{\text{pol}}} + \frac{1}{(2M+1)} \frac{1}{s_M^{(2)}} \left| \frac{\lambda}{\xi} \right|^2 \mathbf{H}^{t_{\text{pol}} \times r_{\text{pol}}} \mathbf{W} \mathbf{W}^H (\mathbf{H}^{t_{\text{pol}} \times r_{\text{pol}}})^H \right) \\ &= \sum_{i=1}^{n_+} \log \left(1 + \frac{\gamma_i}{s_M^{(2)}} \tilde{p}_i \right) \end{aligned} \quad (3.46)$$

where now $\gamma_i, i = 1, 2, 3$, are the three positive eigenvalues of:

$$\mathcal{W}^{t_{\text{pol}} \times r_{\text{pol}}} = \left| \frac{\lambda}{\xi} \right|^2 \frac{1}{2M+1} \mathbf{H}^{t_{\text{pol}} \times r_{\text{pol}}} (\mathbf{H}^{t_{\text{pol}} \times r_{\text{pol}}})^H \quad (3.47)$$

or, equivalently, the eigenvalues of:

$$\mathcal{W}^{t_{\text{pol}} \times r_{\text{pol}}} = \frac{1}{2M+1} \sum_{m=-M}^M \frac{1}{r_m^2} [\mathbf{P}_m^\perp]_{:,1:t_{\text{pol}}} [\mathbf{P}_m^\perp]_{:,1:t_{\text{pol}}}^H \quad (3.48)$$

and where \tilde{p}_i are now defined as

$$\tilde{p}_i = \left[\frac{1}{\vartheta} - \frac{s_M^{(2)}}{\gamma_i} \right]^+ \quad (3.49)$$

where ϑ is the waterlevel, which is fixed according to:

$$\text{SNR}_M = \sum_{j=1}^{r_{\text{pol}}} \tilde{p}_i = \sum_{i=1}^{n_+} \left[\frac{1}{\vartheta} - \frac{s_M^{(2)}}{\gamma_i} \right]^+. \quad (3.50)$$

Now, observe that according to Propositions 1 and 2 above, $\mathcal{W}^{t_{\text{pol}} \times r_{\text{pol}}}$ can be well approximated (when $M \rightarrow \infty, \Delta_T \rightarrow 0, M\Delta_T \rightarrow d, 0 < d < \infty$) by a matrix with analytical closed form entries.

3.6.1 Fully polarized transmitter

For the case of a fully polarized transmitter, as we seen on the previous section, the $\mathcal{W}^{3 \times 3}$ can be approximated as $\overline{\mathcal{W}}^{3 \times 3}$:

$$\overline{\mathcal{W}}^{3 \times 3} = \begin{pmatrix} \psi_2 & 0 & 0 \\ 0 & \psi_4 D^2 \cos^2 \theta & -\psi_3 D^2 \cos^2 \theta \\ 0 & -\psi_3 D^2 \cos^2 \theta & \psi_2 - \psi_4 D^2 \cos^2 \theta \end{pmatrix} \quad (3.51)$$

We can therefore find a closed form expression for the three eigenvalues as

$$\begin{aligned} \gamma_1 &= \psi_2 \\ \gamma_2 &= \frac{1}{2} \left(\psi_2 + \frac{1}{\sqrt{(D^2 - d^2)^2 + (2dD \cos \theta)^2}} \right) \\ \gamma_3 &= \frac{1}{2} \left(\psi_2 - \frac{1}{\sqrt{(D^2 - d^2)^2 + (2dD \cos \theta)^2}} \right) \end{aligned} \quad (3.52)$$

We observe that we always have $\gamma_1 \geq \gamma_2 \geq \gamma_3 > 0$.

This shows that the condition of ordered in descendent order is met since:

- When analysing first eigenvalue vs second eigenvalue: In this case it can be demonstrated that the second term between brackets is smaller than ψ_2 , therefore when comparing the eigenvalues γ_1 and γ_2 we can easily see that γ_1 will be bigger.
- Between the second and third eigenvalue: This case is easier since we can see that they are equal but the second term between brackets it's being subtracted instead of added, and this term has been demonstrated to be smaller than ψ_4 .

- Third eigenvalue bigger than 0: This as the previous condition can be seen because the first term between brackets will be positive and bigger than the second term, this make that this eigenvalue is positive.

Now, lets analyse the condition for activation of the different number of transmission modes (1,2 or 3).

- Activation of one mode ($n_+ = 1$). The condition for activation of only one node is

$$\frac{1}{2} \text{SNR} + \frac{1}{2} \left[\frac{1}{\gamma_1} + \frac{1}{\gamma_2} \right] < \frac{\psi_2}{\gamma_2} \quad (3.53)$$

which can be rewritten as:

$$\text{SNR} < \text{SNR}^{(1)} = \psi_2 \frac{\gamma_1 - \gamma_2}{\gamma_1 \gamma_2} = \frac{\psi_2 - \frac{1}{\sqrt{(D^2-d^2)^2+(2dD \cos \theta)^2}}}{\psi_2 + \frac{1}{\sqrt{(D^2-d^2)^2+(2dD \cos \theta)^2}}} \quad (3.54)$$

- Activation of two modes ($n_+ = 2$). The two conditions are given by

$$\begin{aligned} \frac{1}{2} \text{SNR} + \frac{1}{2} \left[\frac{1}{\gamma_1} + \frac{1}{\gamma_2} \right] &> \frac{\psi_2}{\gamma_2} \\ \frac{1}{3} \text{SNR} + \frac{1}{3} \left[\frac{1}{\gamma_1} + \frac{1}{\gamma_2} + \frac{1}{\gamma_3} \right] &< \frac{\psi_2}{\gamma_3} \end{aligned} \quad (3.55)$$

and this can be reformulated as:

$$\begin{aligned} \text{SNR}^{(1)} < \text{SNR} < \text{SNR}^{(2)} &= \left[\frac{2}{\gamma_3} - \frac{1}{\gamma_1} - \frac{1}{\gamma_2} \right] \psi_2 = \frac{2\psi_2 + 6 \frac{1}{\sqrt{(D^2-d^2)^2+(2dD \cos \theta)^2}}}{\psi_2^2 - \frac{1}{(D^2-d^2)^2+(2dD \cos \theta)^2}} \psi_2 - 1 \\ &= \frac{\psi_2 - \frac{1}{\sqrt{(D^2-d^2)^2+(2dD \cos \theta)^2}}}{\psi_2 + \frac{1}{\sqrt{(D^2-d^2)^2+(2dD \cos \theta)^2}}} + \frac{8\psi_2 \frac{1}{\sqrt{(D^2-d^2)^2+(2dD \cos \theta)^2}}}{\psi_2^2 - \frac{1}{(D^2-d^2)^2+(2dD \cos \theta)^2}} = \text{SNR}^{(1)} + \frac{8\psi_2 \frac{1}{\sqrt{(D^2-d^2)^2+(2dD \cos \theta)^2}}}{\psi_2^2 - \frac{1}{(D^2-d^2)^2+(2dD \cos \theta)^2}} \end{aligned} \quad (3.56)$$

- Activation of three nodes ($n_+ = 3$). This occurs when $\text{SNR} > \text{SNR}^{(2)}$ as defined above.

As an example, we can particularize these thresholds in the broadside ($\theta = 0$), directly leading to

$$\begin{aligned} \text{SNR}^{(1)} &= \frac{1}{\psi_2} \frac{\psi_2 - \frac{1}{D^2+d^2}}{\psi_2 + \frac{1}{D^2+d^2}} \\ \text{SNR}^{(2)} &= \frac{1}{\psi_2} \frac{\psi_2 - \frac{1}{D^2+d^2}}{\psi_2 + \frac{1}{D^2+d^2}} + 8 \frac{\frac{1}{(D^2+d^2)}}{\psi_2^2 - \frac{1}{(D^2+d^2)^2}} \end{aligned} \quad (3.57)$$

- Activation of two modes ($n_+ = 2$). The two conditions are given by

$$\begin{aligned}\frac{1}{2}\text{SNR} + \frac{\psi_2}{2} \left[\frac{1}{\gamma_1} + \frac{1}{\gamma_2} \right] &> \frac{\psi_2}{\gamma_2} \\ \frac{1}{3}\text{SNR} + \frac{\psi_2}{3} \left[\frac{1}{\gamma_1} + \frac{1}{\gamma_2} + \frac{1}{\gamma_3} \right] &< \frac{\psi_2}{\gamma_3}\end{aligned}\quad (3.58)$$

3.6.2 Double polarization transmitter

For the case of a double polarization of transmitter, as we seen on the previous section, the $\mathcal{W}^{2 \times 3}$ can be approximated as $\bar{\mathcal{W}}^{2 \times 3}$:

$$\bar{\mathcal{W}}^{2 \times 3} = \begin{pmatrix} \psi_2 & 0 & 0 \\ 0 & \psi_6(D \cos(\theta))^4 & \psi_5(D \cos(\theta))^3 \\ 0 & \psi_5(D \cos(\theta))^3 & \psi_4(D \cos(\theta))^2 - \psi_6(D \cos(\theta))^4 \end{pmatrix} \quad (3.59)$$

where ψ_2, ψ_4, ψ_5 and ψ_6 have been defined previously.

As previously the three eigenvalues for this matrix can be calculated as:

$$\begin{aligned}\gamma_1 &= \psi_2 \\ \gamma_2 &= \frac{(D \cos \theta)^2}{2} \left[\psi_4 + \sqrt{[\psi_4 - 2(D \cos \theta)^2 \psi_6]^2 + 4(D \cos \theta)^2 \psi_5^2} \right] \\ \gamma_3 &= \frac{(D \cos \theta)^2}{2} \left[\psi_4 - \sqrt{[\psi_4 - 2(D \cos \theta)^2 \psi_6]^2 + 4(D \cos \theta)^2 \psi_5^2} \right]\end{aligned}\quad (3.60)$$

If we remember from the previous section, we want that this eigenvalues are ordered from bigger to lower ($\gamma_1 > \gamma_2 > \gamma_3 > 0$), this can be demonstrated with:

$$(D \cos \theta)^2 \psi_4 = \frac{1}{2d} \int_{-d}^d \frac{(D \cos \theta)^2}{((x - D \sin \theta)^2 + (D \cos \theta)^2)^2} dx \leq \frac{1}{2d} \int_{-d}^d \frac{1}{((x - D \sin \theta)^2 + (D \cos \theta)^2)^2} dx = \psi_2 \quad (3.61)$$

therefore, we can see that it is enough to show that

$$\frac{1}{2} \sqrt{[\psi_4 - 2(D \cos \theta)^2 \psi_6]^2 + 4(D \cos \theta)^2 \psi_5^2} < \psi_4 \quad (3.62)$$

or, equivalently

$$(D \cos \theta)^2 \psi_5^2 < \frac{3}{4} \psi_4^2 + [\psi_4 - (D \cos \theta)^2 \psi_6] (D \cos \theta)^2 \psi_6 \quad (3.63)$$

To see this, consider the matrix

$$\begin{bmatrix} (D \cos \theta)^2 \psi_6 & D \cos \theta \psi_5 \\ D \cos \theta \psi_5 & \psi_4 - (D \cos \theta)^2 \psi_6 \end{bmatrix} = \frac{1}{2d} \int_{-d}^d \frac{1}{r^6(x)} \begin{bmatrix} D \cos \theta \\ (x - D \sin \theta) \end{bmatrix} \begin{bmatrix} D \cos \theta \\ (x - D \sin \theta) \end{bmatrix}^H dx \quad (3.64)$$

where $r(x) = \sqrt{(x - D \sin \theta)^2 + (D \cos \theta)^2}$. This matrix is positive definite by definition, so that its determinant is positive, implying that

$$(D \cos \theta)^2 \psi_6 (\psi_4 - (D \cos \theta)^2 \psi_6) > (D \cos \theta)^2 \psi_5^2. \quad (3.65)$$

Therefore, the second term on the right hand side of the previous equation is positive.

This shows that the condition of ordered in descendent order is met since:

- When analysing first eigenvalue vs second eigenvalue: For the second eigenvalue first term in the elements between bracket, when taking common factor tends to half of ψ_2 and the second term will be positive but smaller than $\psi_2/2$ (since we demonstrated that the term inside is positive but smaller than ψ_4). Therefore the first eigenvalue (ψ_2) will be bigger than the second eigenvalue that can be approximated as $\psi_2/2 + \psi_{2aux}$ where ψ_{2aux} will be something smaller than ψ_2
- Between the second and third eigenvalue: This case is easier since we can see that they are equal but the second term between brackets it's being subtracted instead of added, and this term has been demonstrated to be smaller than ψ_4 .
- Third eigenvalue bigger than 0: This as the previous condition can be seen because the first term between brackets will be positive and bigger than the second term, this make that this eigenvalue is positive.
- Let us now analyze the condition that guarantees the activation of one, two or three transmission modes.

$$\text{SNR} < \text{SNR}^{(1)} = \frac{\gamma_1 - \gamma_2}{\gamma_1 \gamma_2} = \frac{2\psi_2}{(D \cos \theta)^2} \frac{\psi_4 - \sqrt{[\psi_4 - 2(D \cos \theta)^2 \psi_6]^2 + 4(D \cos \theta)^2 \psi_5^2}}{\psi_4^2 - [\psi_4 - 2(D \cos \theta)^2 \psi_6]^2 - 4(D \cos \theta)^2 \psi_5^2} - 1 \quad (3.66)$$

- Activation of two modes ($n_+ = 2$). The two conditions are given by

$$\begin{aligned} \frac{1}{2} \text{SNR} + \frac{1}{2} \left[\frac{1}{\gamma_1} + \frac{1}{\gamma_2} \right] &> \frac{\psi_2}{\gamma_2} \\ \frac{1}{3} \text{SNR} + \frac{1}{3} \left[\frac{1}{\gamma_1} + \frac{1}{\gamma_2} + \frac{1}{\gamma_3} \right] &< \frac{\psi_2}{\gamma_3} \end{aligned} \quad (3.67)$$

and this can be reformulated as

$$\begin{aligned} \text{SNR}^{(1)} < \text{SNR} < \text{SNR}^{(2)} &= \left[\frac{2}{\gamma_3} - \frac{1}{\gamma_1} - \frac{1}{\gamma_2} \right] \psi_2 = \\ &= \frac{2\psi_2}{(D \cos \theta)^2} \frac{\psi_4 + 3\sqrt{[\psi_4 - 2(D \cos \theta)^2 \psi_6]^2 + 4(D \cos \theta)^2 \psi_5^2}}{\psi_4^2 - [\psi_4 - 2(D \cos \theta)^2 \psi_6]^2 - 4(D \cos \theta)^2 \psi_5^2} - 1 \end{aligned} \quad (3.68)$$

- Activation of three nodes ($n_+ = 3$). This occurs when $\text{SNR} > \text{SNR}^{(2)}$ as defined above.

In this chapter we have seen the theoretical analysis for exploring some of the capabilities of an ELAA transmitter with double polarization and fully polarized. Given the scenario in Figure 3.3, we could see how to calculate the optimal precoder for maximizing the capacity, how to calculate the capacity. We could see also how to obtain the eigenvalues of the channel from a holographic asymptotic approximation given closed forms for them, which at the end will help us to calculate the number of activation modes and the optimal precoder.

Now, on the following chapter we are going to validate numerically this asymptotic approximation using Matlab. Also, we will analyse how this optimal precoder behaves and the behaviour of number of activation modes available comparing also the differences between a fully polarized and a double polarization transmitter.

Chapter 4

Numerical validation

Having established the theoretical foundations of the problem, we now move to the practical section of this project, focusing on simulations and numerical analysis using MATLAB. By setting up a controlled simulation environment, we can test and validate the theoretical approximations.

Next, we will implement the theoretical models in MATLAB to simulate system behavior under various conditions. This will allow us to approximate scenarios tending towards infinity and validate the theoretical approximations against general formulas. The simulation results will be analyzed to assess the accuracy of the models and highlighting key findings. This practical exploration bridges the gap between theory and simulation, enhancing our understanding of the theoretical constructs. All the Matlab code is available at the appendix section 5.

The objective of this chapter is twofold. On the one hand, we will first devote the first sections to a numerical validation of the asymptotic results presented above. Thereafter, we will use these analytical results to investigate the number of available spatial modes in the space and its dependence on physical parameters such as the elevation, the relative dimension of the array and the number of orthogonal polarizations used at the transmitter.

4.1 Scenario by default

This study focuses on the behavior of an antenna array transmitter and its interaction with a receiver under controlled theoretical conditions. Unless stated otherwise, the antenna array transmitter is simulated to be centered at the origin of the coordinate system and consists of 1001 antennas, with 500 antennas on each side along the y-axis, it is also important to note that the transmitter is assumed to know the transmitter channel which is not always the situation in real life. This setup is illustrated in Figure 3.3.

For the purpose of this theoretical analysis, the following conditions are assumed:

- **Permittivity:** Unless stated otherwise, to be normalized.
- **Power:** Unless stated otherwise, to be normalized.
- **Frequency:** Operating at 6 GHz.
- **Element Separation:** The separation between elements in the antenna array is 0.1 wavelength.

These simplified parameters allow us to focus on the fundamental behavior of the system by abstracting ourselves from physical electromagnetic characteristics of the channel. Since our primary objective is to understand the underlying principles and interactions, the use of idealized parameters is justified. It provides a clear and controlled environment to observe the effects of various changes in the system, which can later be adapted to more realistic scenarios.

The position of the receiver will vary depending on the specific aspect of the study being conducted. This variability is essential to understand the influence of different positions on the system's performance. The receiver will be assumed to have full polarization and we will assume that the rotation matrix between receiver and transmitter is \mathbf{I} . This can be seen to be irrelevant in the fully polarized (3×3) situation. When the transmitter uses only two polarizations, this assumption implies that the two transmit infinitesimal dipoles are oriented in the directions of the x and y axis.

It is important to note that the MATLAB code used for simulations is designed to be flexible, allowing easy modification of these parameters to suit different real-world conditions. This approach ensures that our initial findings remain relevant and can be applied to more complex, real-world environments.

In summary, the theoretical parameters chosen for this study provide a foundation for understanding the behavior of the antenna array system. By starting with these ideal conditions, we establish a baseline that can be expanded upon with more detailed and realistic parameters in future work.

4.2 Calculating the optimum precoder matrix

In this section we will calculate the optimum precoder that focalizes the transmission on a particular spatial point, then we analyze the performance of this precoder when the receiver is not located in the intended position, but rather moves around the y-z plane.

4.2.1 Steps Followed

Following the theory, in order to calculate the precode matrix we followed the next steps:

1. Calculate the distance and vector distance from each of the elements of the antenna array to the receiver equation (3.1).
2. Calculate the transmit channel matrix equation (3.4).
3. Concatenate all of the transmit channel matrix of the elements to form the transmit channel matrix of the system equation (3.11).
4. Calculate the singular value decomposition of the transmit channel, from that we will use the right singular vector (\mathbf{V}) and the singular values.
5. Using the positive coefficients $\sqrt{\rho_1}, \dots, \sqrt{\rho_{r_{pol}}}$ we will implement the waterfilling algorithm equation (3.27). Note that the waterfilling works on the eigenvalues (rather than the singular values) of the channel matrix, so we need to take the square of the original quantities.
6. From that we will get the positive coefficients $\sqrt{p_1}, \dots, \sqrt{p_{r_{pol}}}$ equation (3.25).
7. With that we will be able to calculate the matrix $\mathcal{P}^{1/2}$ with only the active channels, filling the diagonal of $\mathcal{P}^{1/2}$ with the corresponding power allocation values.
8. With the previous matrix $\mathcal{P}^{1/2}$ and with the right singular vector (\mathbf{V}) we will be able to calculate the optimum precoder as $\mathbf{W} = \mathbf{V}\mathcal{P}^{1/2}$.

4.2.2 Analysing the capacity

In this section, we will analyze the capacity of our scenario with an ELAA using the optimal precoder derived earlier. Understanding capacity provides crucial insights into the maximum achievable data rates, the impact of array configurations, and the efficiency of power allocation. This analysis helps in optimizing system performance and guiding practical design choices. To calculate the capacity of the system we will use the equation (3.16).

4.2.2.1 Fully polarized transmitter

Let's first analyse the capacity of the system with a fully polarized transmitter. First, we calculated the optimum precoder for each point on the simulate plane and we computed the capacity of the system when the receiver is at each of these points to analyse how the capacity varies across the space. We can see the result of the simulation in Figure 4.1. Observe that

higher capacity is obtained when we are close to the center of the array (point with coordinates (0,0) in that figure), and that it obviously decays with distance due to the fact that the channel norm decays with the square of this quantity.

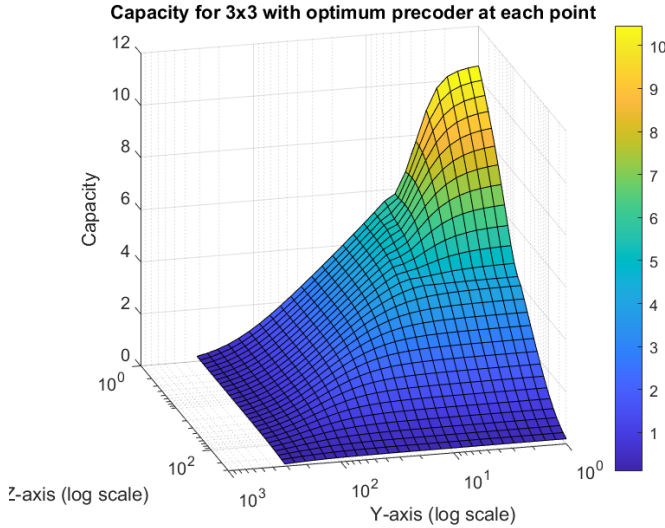


Figure 4.1: Capacity when the optimum precoder is done for each point on the grid for a fully polarized transmitter.

Next, we consider the behaviour in a more realistic setting where the precoder is designed for a particular user location, while the user is effectively somewhere else. In this situation, the capacity of the user is of course typically lower, unless we consider locations that are closer to the transmit array (which may experience higher channel quality and hence higher capacity). We analysed two cases: a first case where the receiver is at position $Y=Z=2$ Figure 4.2 and a second case where receiver is at the location $Y=Z=15$ Figure 4.3).

As we can see on the Figure 4.5, for the case that the receiver has been calculated for the point $X=Y=2$, the capacity reaches its global maximum 8.6 bit/s/Hz, at this particular point, while around this point the capacity decays really fast.

For the case that the receiver is located more far away $X=Y=15$, the capacity reaches a local maximum of 3.5 bit/s/Hz, and also decays when the true location moves away from that point. However, in the vicinity of the transmitter the capacity also reaches a comparable value. As mentioned above, this is because the channel response becomes stronger as we approach the transmit array. This implies a better capacity regardless of the precoder.

4.2.2.2 Double polarization at the transmitter

Let's now analyse the capacity of the system with a doubly polarized transmitter. As in the case of the fully polarized transmitter, we calculated the optimum precoder for each point in the

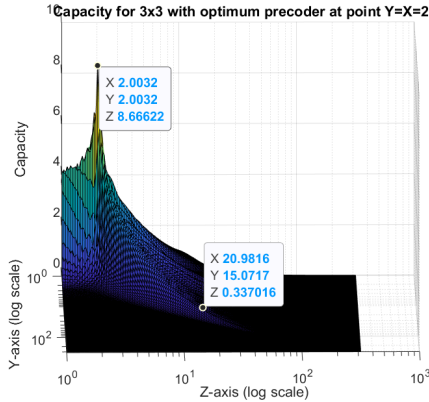


Figure 4.2: Optimum precoder calculated for position $X=Y=2$

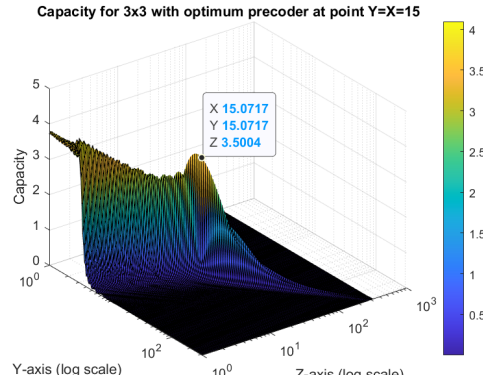


Figure 4.3: Optimum precoder calculated for position $X=Y=15$

Figure 4.4: Capacity when the optimum precoder is done for just one point of the grid for a fully polarized transmitter

space simulated and computed the capacity of the system when the receiver is at each of these points to analyse how the achievable rate varies across the space. We can see the result of the simulation in Figure 4.5.

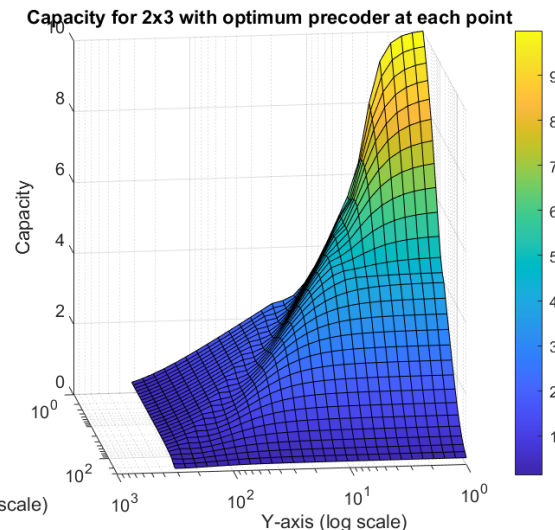


Figure 4.5: Capacity when the optimum precoder is done for each point on the grid for a double polarization transmitter

Note that the achievable rates are slightly lower than in the fully polarized case, although no big differences are in practice observed. As in the fully polarized case, now, we will see the behaviour in the real case, where the receiver is known to be at one location (we analysed two cases: the receiver is at position $Y=Z=2$ and case where receiver is at the location $Y=Z=15$),

and we will analyse the capacity of the system at all the points in the space. We can see on Figure 4.8 both cases.

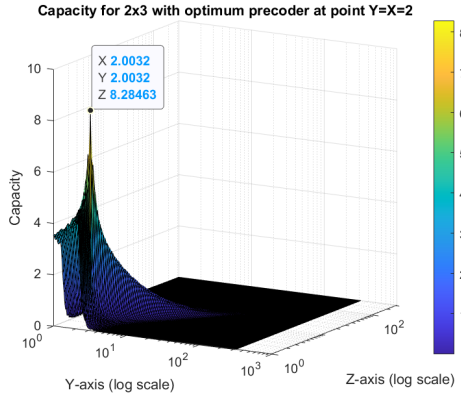


Figure 4.6: Optimum precoder calculated for position $X=Y=2$

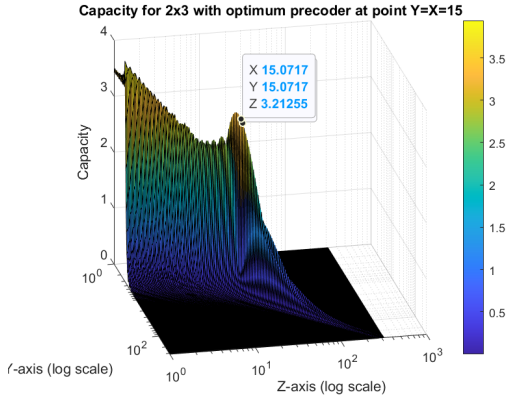


Figure 4.7: Optimum precoder calculated for position $X=Y=15$

Figure 4.8: Capacity when the optimum precoder is done for just one point of the grid for a double polarization transmitter

We can see on the Figure 4.8 that in the case that the optimum precoder has been calculated for the position $X=Y=2$ that the maximum of the capacity is at this point with a maximum of 8.2 bit/s/Hz. Nearby this point we can see that the capacity falls sharply as in the fully polarized case.

In the case of the precoder calculated for the position $X=Y=15$, we can see that the capacity near the antenna is a little bit bigger than at this point but we can also clearly differentiate a local maximum with 3.2 bit/s/Hz as max.

4.2.2.3 Analysing the capacity results

The capacity is generally expected to be higher near the transmitter compared to farther away, and this has been corroborated by the figures where we calculate the optimal precoder for each of the points in the space. This is due to several reasons:

1. **Signal Strength:** Closer to the transmitter, the signal strength is higher due to lower path loss. This results in a higher signal-to-noise ratio (SNR), which directly translates to higher capacity.
2. **Less interference:** We can see that at other points than the defined receiver, the capacity is really low, this behaviour is as the normalized gain seen in some papers, what can be associated to really low interference at other positions.

3. **Beamforming and Spatial Resolution:** For systems like ELAA, the spatial resolution and the effectiveness of beamforming are enhanced when the receiver is closer to the array. The array can more precisely direct its energy towards the receiver, improving the effective channel conditions and thus the capacity.

Therefore, as the receiver moves away from the transmitter, the capacity generally decreases due to increasing path loss, reduced SNR, and potentially poorer channel conditions.

This trend can change when using an optimal precoder for a given position as we can see on the images where we fixed the receiver position and we used for the whole system the optimal precoder corresponding to that user. The optimal precoder allows us to:

1. **Beamfocus the Signal:** Focus the signal into a specific region in space, ensuring that the user at this position receives maximum power. This targeting improves the effective SNR at the user's location, enhancing capacity even at greater distances.
2. **Power Efficiency:** By focusing the signal, the required power at the transmitter to ensure the user receives the message can be reduced. This efficiency means that less power is needed to maintain high capacity.
3. **Interference Reduction:** The optimal precoder also reduces the received power for users in different positions, thus minimizing interference with other systems. This selective transmission enhances overall network performance by reducing unwanted signal spillover.

By leveraging optimal precoding, we can significantly mitigate the negative effects of distance on capacity, maintaining high performance even as the receiver moves away from the transmitter if we adapt the optimal precoder to this moving user.

However, as we move further away from the transmitter, even with an optimal precoder for a given receiver position, the maximum capacity of the system might not be achievable at this receiver's position. This is because the overall signal power diminishes with distance due to path loss, and the effectiveness of beamforming decreases. Thus, despite optimal precoding, physical limitations set an upper bound on the achievable capacity far from the transmitter. As we can see on the previous figures, we can achieve a local maximum making sure that we will be receiving a significant amount of power to recover the message compared to other users in the vicinity at different locations. Additionally, in real life this matter could be significantly more challenging since environmental factors such as obstacles and multipath effects can degrade the channel conditions, making it challenging to maintain high capacity at greater distances.

Let us know compare both cases when we have a fully polarized transmitter and when we have a double polarization transmitter, to compare them we plot the difference in capacity

between the fully polarized and the double polarization case, which is represented in the Figure 4.9.

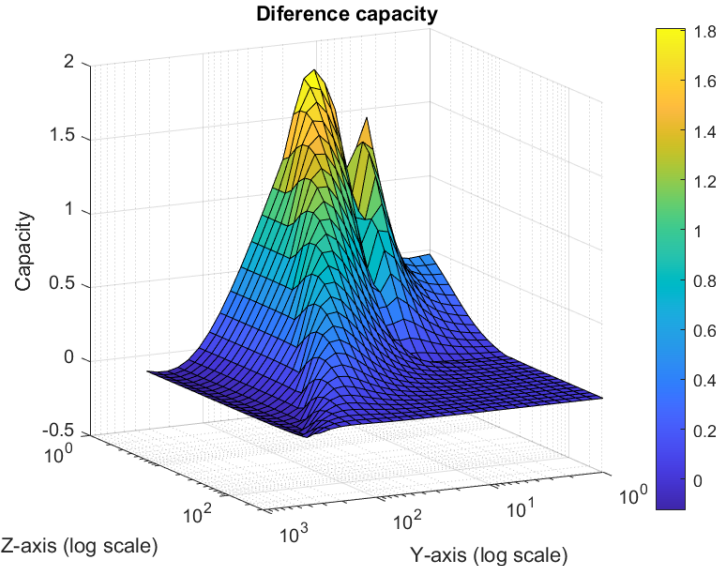


Figure 4.9: Difference in capacity between fully polarized and double polarization transmitter when the optimum precoder is used at every point.

In the Figure 4.9 we can see that the capacity that we can provide with a fully polarized it is higher in every region in the space, although this improvement is not uniform. Near the antenna array position the improvement in terms of capacity is not as significant as in a medium distance from the antenna array, so for users that can be at a medium distance from the antenna it can be really interesting to work with a fully polarized antenna, since this improvements will be significant. Far away of the antenna the capacity improvement is almost 0.

By exploiting multiple polarization states, it can create more parallel channels within the same spatial and frequency resources, boosting spatial multiplexing and overall system capacity. Additionally, the ability to use multiple polarization states allows for better separation of signals, mitigating interference and improving the signal-to-noise ratio (SNR) for each channel.

In contrast, a double polarized transmitter limits the diversity gain and the number of parallel channels available for spatial multiplexing, this reduces the system's capacity. Furthermore, with fewer polarization states, the ability to separate signals and mitigate interference is diminished, potentially leading to lower SNR and reduced capacity.

In real life, utilizing a wider range of polarization states in a fully polarized system also helps overcome adverse channel conditions, such as multipath fading.

4.3 Accuracy of the asymptotic approximations

In this section we will numerically assess the accuracy of the asymptotic behaviour of $\bar{\mathcal{W}}^{t_{pol} \times r_{pol}}$ validate the analytical expressions for the eigenvalues of the channel obtained in the previous chapter.

4.3.1 Validation procedure

In this section we will explain the steps followed numerically assess the accuracy of the asymptotic approximation. To do so, we will first validate the asymptotic behaviour of $\bar{\mathcal{W}}^{t_{pol} \times r_{pol}}$ by comparison with the original matrix $\mathcal{W}^{t_{pol} \times r_{pol}}$. We operate according to the following steps:

1. Calculate $\mathcal{W}^{t_{pol} \times r_{pol}}$ from equation (3.48).
2. Calculate $\bar{\mathcal{W}}^{t_{pol} \times r_{pol}}$ from equation (3.51) for fully polarized transmitter and (3.59) for the double polarization.
3. Compare the obtained matrices and quantify the error between them.

Once we have validated the $\mathcal{W}^{t_{pol} \times r_{pol}}$ compared to its approximation, we will then validate the expression of the eigenvalues obtained from this matrix compared to the ones we can obtain from the channel.

1. Calculate eigenvalues for the case we are taking into account the asymptotic approximation from equations.
2. Calculate the eigenvalues of the previous calculated transmit channel and sort them in descending order.
3. Compare the obtained matrices and quantify the error between them.

4.3.2 Matrix $\mathcal{W}^{t_{pol} \times r_{pol}}$ validation

Let us now validate the asymptotic behaviour of $\bar{\mathcal{W}}^{t_{pol} \times r_{pol}}$ by comparing it against the matrix $\mathcal{W}^{t_{pol} \times r_{pol}}$ calculated from the \mathbf{P}_m^\perp via MatLab simulations. We will identify the components of the matrix as [row, column].

4.3.2.1 Fully polarized transmitter

Let's first focus on the case of the fully polarized transmitter. To compare them we plot the relative error of four of the nine components of the $\mathcal{W}^{t_{pol} \times r_{pol}}$ matrix.

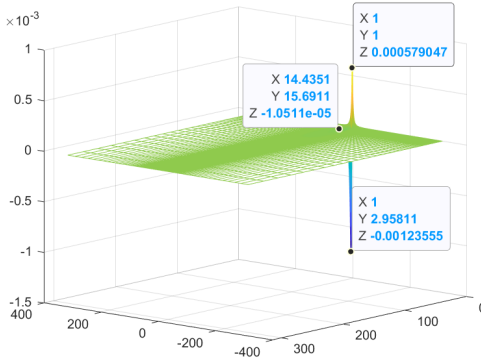


Figure 4.10: Relative error of component [1,1] for $r_{pol} = t_{pol} = 3$

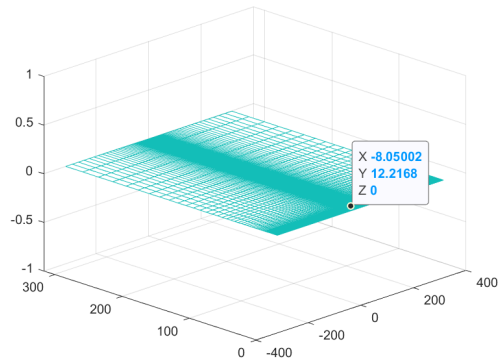


Figure 4.11: Relative error of component [1,2] for $r_{pol} = t_{pol} = 3$

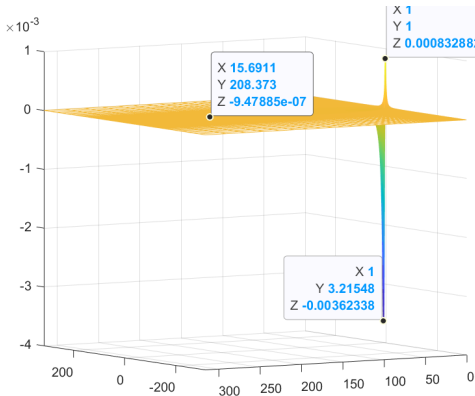


Figure 4.12: Relative error of component [2,2] for $r_{pol} = t_{pol} = 3$

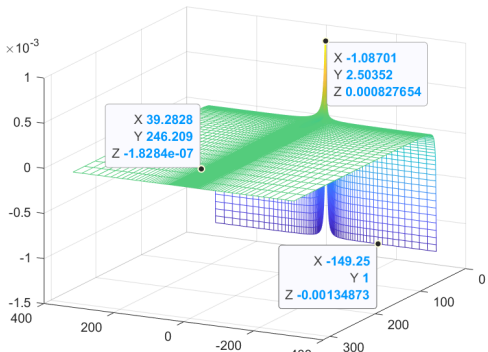


Figure 4.13: Relative error of component [3,3] for $r_{pol} = t_{pol} = 3$

In general, from the graphics above, we can see that the accuracy of the asymptotic approximation is significantly good regardless of the position of the intended receiver, except for positions that are relatively close to the transmitter, which exhibit a higher error magnitude. Across various scenarios, we observed consistent results where the relative error remained around 10^{-3} , indicating a high degree of accuracy in our approximation method. This demonstrates that the asymptotic approximation is effective and can be reliably used as a good approximation of the original channel matrix.

As pointed out above, we can also observe that the error is relatively high near the origin of the coordinates and very low in other points in the space for the cases [1,1], [2,2], [2,3], and [3,2]. For the cases [1,2], [1,3], [2,1], and [3,1], the error is negligible in all instances. Finally, we can see that the case [3,3] is the worst case, where we are getting more error along the z-axis.

The higher error near the antenna in most components can be expected since this region does

not adhere as well to the asymptotic behavior, given that the distance between transmitters does not tend to zero compared to the distance to the receiver of our antenna array. This discrepancy can be attributed to the physical limitations of the antenna placement and the inherent geometric constraints.

Next, we will examine how the accumulated absolute error squared of all components on the matrix $\mathcal{W}^{t_{pol} \times r_{pol}}$ changes when we vary the area of the transmit array. To do this, we simulated scenarios where the product between the number of antennas and the separation between them remains constant. This constant product essentially represents the effective length of the antenna array.

In the simulations, we compared the eigenvalues for different configurations where this product varied, thereby altering the antenna array's effective length. It is important to note that this approach slightly modifies the initial scenario configuration that we initially established. Through this examination, we aim to understand the relationship between the antenna array's physical dimensions and the accuracy of our asymptotic approximation.

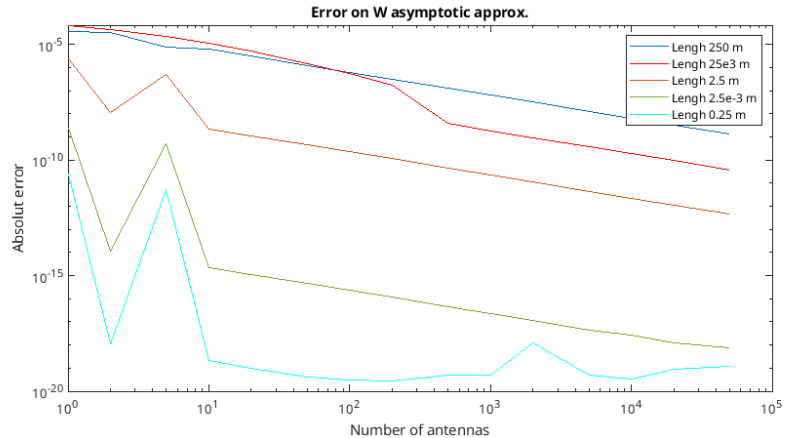


Figure 4.14: Accumulated absolute error at the power of 2 for matrix $\mathcal{W}^{t_{pol} \times r_{pol}}$

As expected, the accuracy increases as the number of antennas grows and the separation between them is reduced, which is the basic assumption that is made in the derivations, when we approximate to this holographic asymptotic approximation the whole transmitter as a radiating surface. On the other hand, we also see that the accuracy is significantly low even for a relatively small number of transmit elements. We can also see that the error has its upper limit around when the antenna length 250m, since the error in this case and with 25e3m the error is almost the same, it is important to realize the difference in order when we change the area since it is really significant, showing that our approximations work specially well when the area is lower, and if we need to implement in real life we will need to consider this error as part of the trade-off between the precision and the size, since building antennas more and more smaller will be more

costly and we might arrive to technology limits.

Despite this modifications we can see that the error is really low in all the cases so we can validate our asymptotic approximation as valid.

4.3.2.2 Double polarization transmitter

Let's now focus on the case of the double polarization transmitter:

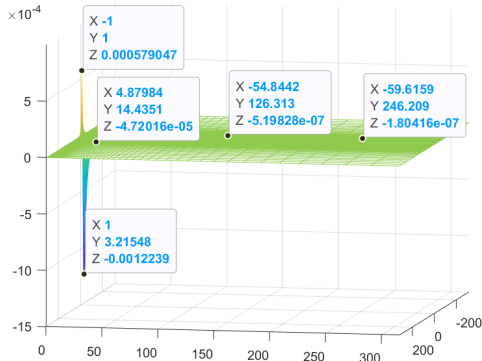


Figure 4.15: Relative error of component [1,1] for $r_{pol} = 3, t_{pol} = 2$

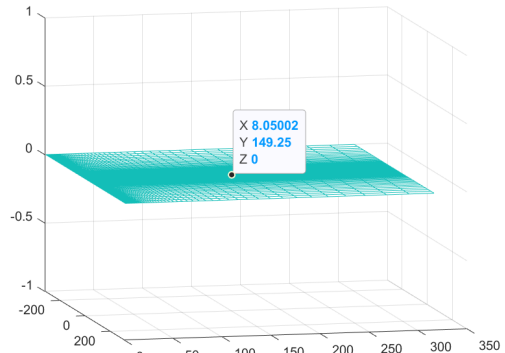


Figure 4.16: Relative error of component [1,2] for $r_{pol} = 3, t_{pol} = 2$

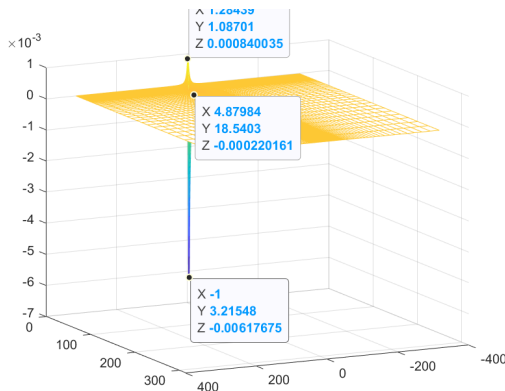


Figure 4.17: Relative error of component [2,2] for $r_{pol} = 3, t_{pol} = 2$

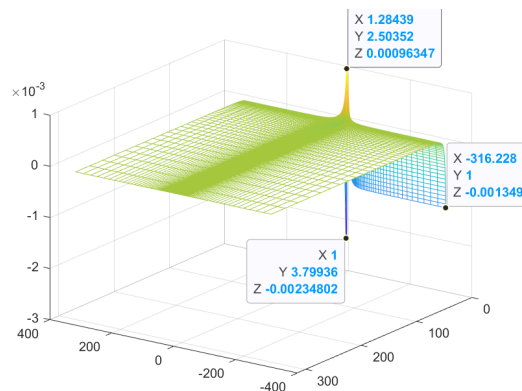


Figure 4.18: Relative error of component [3,3] for $r_{pol} = 3, t_{pol} = 2$

In the case of the double polarization case, we can see that similar numerical results are obtained, where we get higher errors near the antenna array for the same reason as before. Also, in this case we can see that the component [3,3] is the one with a higher error, despite that the error is still very low, with a maximum relative error of the order of 10^{-3} .

Now, we can do the same exercise as before and plot the error when we change the number of antennas and separation between the elements on the antenna array for different areas.

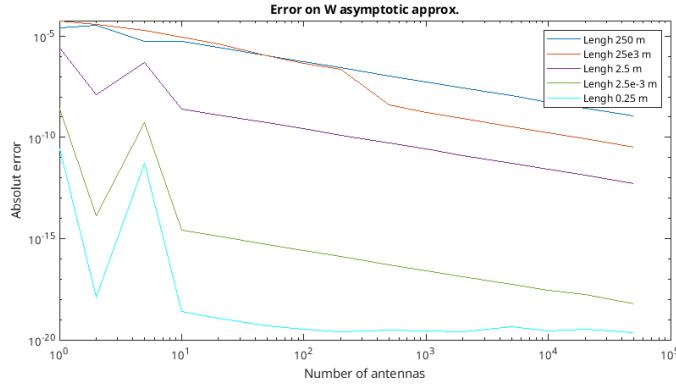


Figure 4.19: Accumulated absolute error at the power of 2 for matrix $\mathcal{W}^{t_{pol} \times r_{pol}}$

We can see the same behaviour as before where increasing the number of antennas and decreasing the separation between antennas it improves the estimation giving us less error and in general the higher is the area the bigger is the error we are committing.

So we can validate the results approximation for the $\mathcal{W}^{t_{pol} \times r_{pol}}$ asymptotic approximation also for this case and we can see that the approximations in the two cases, fully polarized and double polarized transmitter with the same accuracy, since the error we are getting in both cases is the same.

4.3.3 Eigenvalues validation

Now, let us go a step farther and compare the eigenvalues of this asymptotic approximation with the eigenvalues of the transmit channel. In the previous section we explained how can we obtain these eigenvalues that we are going to validate now. As we have done on all previous cases we will validate the fully polarized transmitter case and double polarization in the transmitter case.

In this case instead of plotting the relative error we will plot the ratio between them since it will give us some relevant information that we will analyse and explain later.

4.3.3.1 Fully polarized transmitter

Let us begin with the case of the fully polarized transmitter. These eigenvalues as explained on the Steps section can be obtained from:

- Eigenvalues asymptotic approximation: Equations (3.52).

- Eigenvalues from transmit channel of the system eigenvalues(HH^H).

In Figures 4.20, 4.21 and 4.22 we can see the ratio between eigenvalues from the channel and eigenvalues with asymptotic approximation.

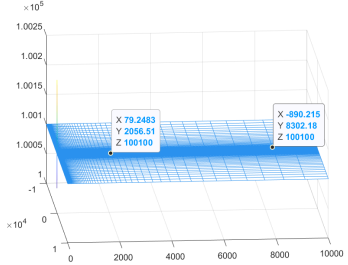


Figure 4.20: Relative error of eigenvalue 1 $r_{pol} = t_{pol} = 3$

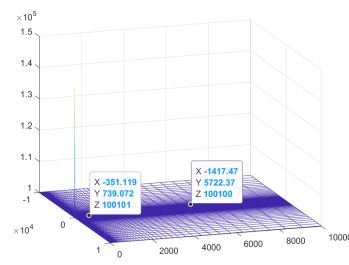


Figure 4.21: Relative error of eigenvalue 2 for $r_{pol} = t_{pol} = 3$

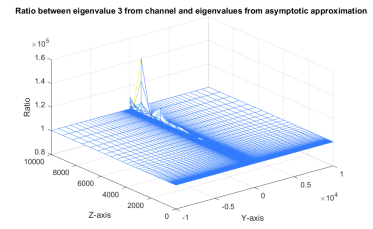


Figure 4.22: Relative error of eigenvalue 3 for $r_{pol} = t_{pol} = 3$

We can see that the ratio is a constant approximately 100100 at all the points in the space, in the case of the eigenvalue 3 we can see that we have more variation in that ratio than in the other cases. Really close to the transmitter we can see that this ratio is modified, specially as said in the case of eigenvalue 3, that difference near the transmitter can be associated to the fact that the asymptotic approximation don't work as well.

Now, we will plot how the error varies when we change the area of the transmitter, to do that we simulated cases where the product between the number of antennas and the separation between them is constant, and we compared the eigenvalues for different iterations with this product being different between them. This product will give us the length of the antenna array if we suppose the wide to be 1 we will obtain the area of the ELAA.

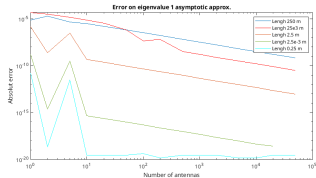


Figure 4.23: Absolute error on eigenvalue 1 with fixed Area at position Y=60 and Z=80 for $r_{pol} = 3, t_{pol} = 3$

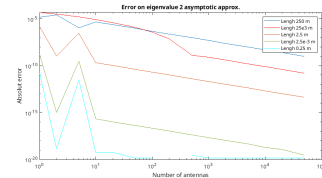


Figure 4.24: Absolute error on eigenvalue 2 with fixed Area at position Y=60 and Z=80 for $r_{pol} = 3, t_{pol} = 3$

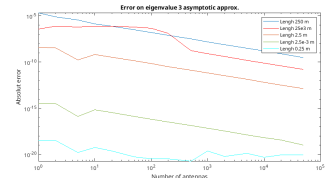


Figure 4.25: Absolute error on eigenvalue 3 with fixed Area at position Y=60 and Z=80 for $r_{pol} = 3, t_{pol} = 3$

Like in the case we're we did the same exercise with the $\mathcal{W}^{t_{pol} \times r_{pol}}$ we are getting basically the same result, with higher number of antennas and lowering the distance between elements on the antenna array the approximation it behaves closer to the real scenario, giving us lower

difference between them. Also, as before, the bigger is the area, the bigger is the error we are committing. A thing that we can easily realize is that the error between $\mathcal{W}^{t_{pol} \times r_{pol}}$ matrix and between the eigenvalues have the same order as we could expect since they come from the same approximation.

4.3.3.2 Double polarization transmitter

And now let's analyse the case of the double polarization transmitter. In this case the the equations we're we calculate the eigenvalues of the asymptotic approximation are the equation (3.60). We can see the figures show the ratio on the figures 4.26, 4.27 and 4.28.

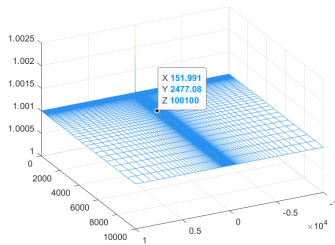


Figure 4.26: Relative error of eigenvalue 1 $r_{pol} = 3, t_{pol} = 2$

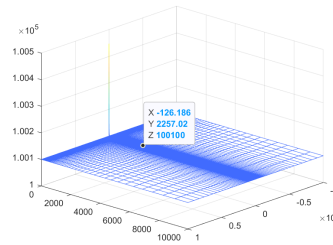


Figure 4.27: Relative error of eigenvalue 2 for $r_{pol} = 3, t_{pol} = 2$

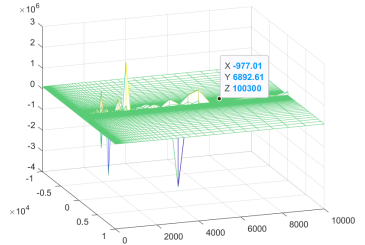


Figure 4.28: Relative error of eigenvalue 3 for $r_{pol} = 3, t_{pol} = 2$

Now, we can do the same exercise as before and plot the error when we change the number of antennas and separation between the elements on the antenna array for different areas.

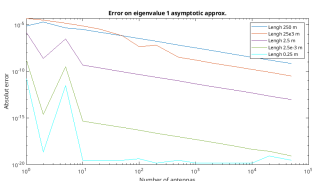


Figure 4.29: Absolute error on eigenvalue 1 with fixed Area at position Y=60 and Z=80 for $r_{pol} = 3, t_{pol} = 2$

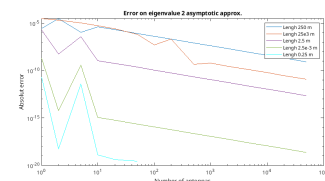


Figure 4.30: Absolute error on eigenvalue 2 with fixed Area at position Y=60 and Z=80 $r_{pol} = 3, t_{pol} = 2$

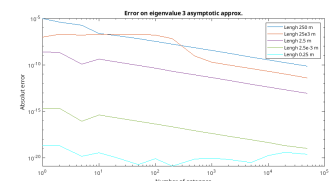


Figure 4.31: Absolute error on eigenvalue 3 with fixed Area at position Y=60 and Z=80 for $r_{pol} = 3, t_{pol} = 2$

As in the previous case, the behaviour is also the same higher number of antennas and lower separation between them the approximation work better and as the area increases the error it becomes higher.

4.3.3.3 Results analysis

After calculating the ratio between a given value and its asymptotic approximation, it was observed that this ratio remains constant at most of the points in space, we can see that this ratio are different at some points near the antenna array origin of coordinates and at some points random in the space.

This constancy indicates that there is a predictable, consistent difference between the calculated value and its asymptotic approximation which is around 10100. By compensating for this ratio between the eigenvalues, we can correct for this difference on the transmit channel, leading to more accurate calculations. This correction can be specifically related to the equation below:

$$\mathcal{W}^{t_{\text{pol}} \times r_{\text{pol}}} = \left| \frac{\lambda}{\xi} \right|^2 \frac{1}{2M+1} \mathbf{H}^{t_{\text{pol}} \times r_{\text{pol}}} \left(\mathbf{H}^{t_{\text{pol}} \times r_{\text{pol}}} \right)^H \quad (4.1)$$

Then the factor to correct between the eigenvalues then can be associated to $(2M+1) \left| \frac{\lambda}{\xi} \right|^2$. Therefore to correct this factor we will need to multiply by the square of this factor the channel, since the eigenvalues from the channel are calculated with the power of two of the channel. By applying this correction, we can now verify that the eigenvalues are the same, so in the following figures we can see the ratio once this correction has been applied.

First, for the fully polarized transmitter:

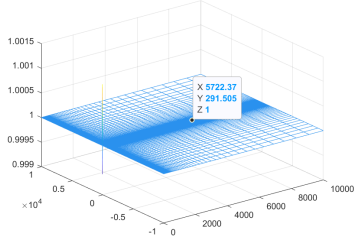


Figure 4.32: Ratio of eigenvalue 1 with corrected factor $r_{\text{pol}} = 3, t_{\text{pol}} = 3$

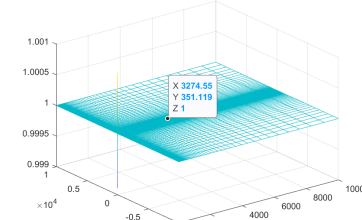


Figure 4.33: Ratio of eigenvalue 2 with corrected factor for $r_{\text{pol}} = 3, t_{\text{pol}} = 3$

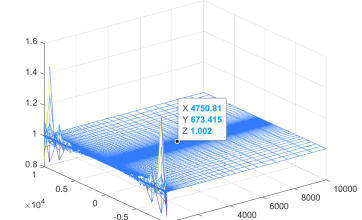


Figure 4.34: Ratio of eigenvalue 3 with corrected factor for $r_{\text{pol}} = 3, t_{\text{pol}} = 3$

Now, for the double polarization transmitter:

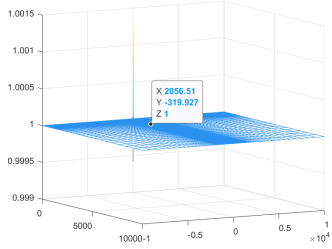


Figure 4.35: Ratio of eigenvalue 1 with corrected factor for $r_{pol} = 3, t_{pol} = 2$

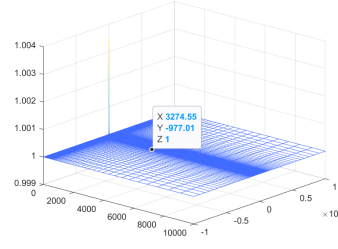


Figure 4.36: Ratio of eigenvalue 2 with corrected factor for $r_{pol} = 3, t_{pol} = 2$

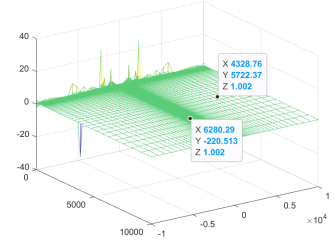


Figure 4.37: Ratio of eigenvalue 3 with corrected factor for $r_{pol} = 3, t_{pol} = 2$

As we can see on the figures above, with the correction factor applied the ratio between the compared eigenvalues becomes 1, so the approximation is working fine.

Also, we've seen that like with the $\mathcal{W}^{t_{pol} \times r_{pol}}$ estimation as the number of antenna increase and the separation between them decreases the result we are getting is better, that align with the principle of holographic MIMO to put the maximum number of antennas in the same space in order to the extreme have something like a radiating surface.

Reducing the area of our antenna will provide a better approximation to desired performance characteristics, such as enhanced spatial resolution and beamforming capabilities. However, this comes at a higher cost due to the need for smaller, more precisely manufactured antennas. Advanced materials and fabrication techniques are required, which are more expensive and complex. Additionally, achieving the same performance in a smaller size involves intricate design processes and potential trade-offs in bandwidth and efficiency. At some point, we may also encounter technological limits, where further miniaturization becomes impractical.

4.4 Activation modes

In this section, we use the asymptotic approximation formulas to study the number of spatial multiplexing modes that are activated in space. To analyse that, we will make some transformations to the previous equations to find the SNR that determines the number of activation nodes.

We will transform the SNR_M equations and the limits ($SNR^{(N)}$) to depend only on two parameters d/D and θ the angle. Reducing the number of parameters simplifies the process of solving the problem, facilitating system design and parameter selection. It also aids in characterizing system behavior across various scenarios with different parameter variations. This in

in the future we can analyse the behaviour of the distance D depending on the angle for the limits where 1, 2 or 3 modes are available.

To get the number of active modes from the asymptotic approximation we will need to compare the SNR_M of our system at one point, with the limit for activating the channels ($SNR^{(N)}$) at the same point. So, first, since the SNR_M can be express generally independently from the number of polarization's at the transmitter we will transform following from equation (3.33) as:

$$\frac{SNR'}{D^2} = SNR \frac{D^2}{D^2} = \frac{P}{D^2 \sigma^2 t_{pol}} \left| \frac{\xi}{\lambda} \right|^2 \psi'_2$$

Now, we need to apply the transformations to the limits $SNR^{(N)}$ so they can be calculated from just the two parameters θ that defines the angle and d/D that defines relation between the ELAA distance and the distance to the receiver,

You can see on the following subsections the transformations needed for both cases: fully polarized transmitter and double polarization transmitter.

4.4.1 Fully polarized Transmitter

Let us begin with the case of the fully polarized transmitter, we will transforms the equations (3.54) and (3.56) to depend only on the parameters θ and d/D . Since the limits they only depend on those 2 parameters, it is better in the sense that we will have less unknowns variable for our system, helping us to compare different scenarios in the future.

To make that transformations we will focus on the first limit ($SNR^{(1)}$) and then, since both equations are similar it will be quite easy to extrapolate the results into $SNR^{(2)}$. The $SNR^{(1)}$ can be calculated as:

$$SNR^{(1)} = \psi_2 \frac{\gamma_1 - \gamma_2}{\gamma_1 \gamma_2} = \frac{\psi_2 - \frac{1}{\sqrt{(D^2 - d^2)^2 + (2dD \cos \theta)^2}}}{\psi_2 + \frac{1}{\sqrt{(D^2 - d^2)^2 + (2dD \cos \theta)^2}}}$$

To do the transformations we can multiply the numerator and denominator with D^2 , with what we will have:

$$SNR^{(1)} = \frac{\psi_2 D^2 - \frac{D^2}{\sqrt{(D^2 - d^2)^2 + (2dD \cos \theta)^2}}}{\psi_2 D^2 + \frac{D^2}{\sqrt{(D^2 - d^2)^2 + (2dD \cos \theta)^2}}}$$

We can define the following new terms to simplify the transformations:

$$\psi'_2 = \psi_2 D^2 = \frac{1}{2\frac{d}{D} \sin \theta} [...] \quad (4.2)$$

Note: In this case we left between brackets the terms that can change depending on the relation between D and d.

$$\psi'_8 = \frac{D^2}{\sqrt{(D^2 - d^2)^2 + (2dD \cos \theta)^2}} = \frac{1}{\sqrt{\left(1 - \left(\frac{d}{D}\right)^2\right)^2 + (2\frac{d}{D} \cos \theta)^2}} \quad (4.3)$$

Then, the $SNR^{(1)}$ can be reformulated as:

$$SNR^{(1)} = \frac{\psi'_2 - \psi'_8}{\psi'_2 + \psi'_8} \quad (4.4)$$

And for the $SNR^{(2)}$ is quite simple to see that it can be reformulated as:

$$SNR^{(2)} = SNR^{(1)} + \frac{8\psi'_2\psi'_8}{\psi'^2_2 - \psi'^2_8} \quad (4.5)$$

4.4.2 Double Polarization Transmitter

Let us now do the transformations for the limits ($SNR^{(N)}$) for double polarization transmitter case considering the equations (3.66) and (3.68) so they, as before, only depend on the parameters θ and d/D :

$$\begin{aligned} SNR^{(1)} &= \frac{2\psi_2}{(D \cos \theta)^2} \frac{\psi_4 - \sqrt{[\psi_4 - 2(D \cos \theta)^2 \psi_6]^2 + 4(D \cos \theta)^2 \psi_5^2}}{\psi_4^2 - [\psi_4 - 2(D \cos \theta)^2 \psi_6]^2 - 4(D \cos \theta)^2 \psi_5^2} - 1 = \frac{SNR^{(1)} D^4}{D^4} = \\ &= \frac{2D^2 \psi_2}{(D \cos \theta)^2} \frac{D^2 \psi_4 - \sqrt{[D^2 \psi_4 - D^2 2(D \cos \theta)^2 \psi_6]^2 + (2D^3 \cos \theta)^2 \psi_5^2}}{(D^2 \psi_4)^2 - [\psi_4 D^2 - (D \cos \theta)^2 D^2 \psi_6]^2 - 4(D^2 \cos \theta)^2 \psi_5^2} - 1 \end{aligned} \quad (4.6)$$

Then we can redefine following the next equations:

$$\begin{aligned}
\psi'_4 &= D^4 \psi_4 = \frac{1}{2 \cos^2 \theta} \left[\frac{\left(1 + \left(\frac{d}{D}\right)^2\right) - 2 \sin^2 \theta}{\left(1 + \left(\frac{d}{D}\right)^2\right)^2 - \left(2 \frac{d}{D} \sin \theta\right)^2} + D^2 \psi_2 \right] \\
\psi'_5 &= D^5 \psi_5 = - \frac{\left(1 + \left(\frac{d}{D}\right)^2\right) \sin \theta}{\left(\left(1 + \left(\frac{d}{D}\right)^2\right)^2 - \left(2 \frac{d}{D} \sin \theta\right)^2\right)^2} \\
\psi'_6 &= D^6 \psi_6 = \frac{1}{4 \cos^2 \theta} \frac{\left(1 + \left(\frac{d}{D}\right)^2\right)^2 - 4 \sin^2 \theta}{\left(\left(1 + \left(\frac{d}{D}\right)^2\right)^2 - \left(2 \frac{d}{D} \sin \theta\right)^2\right)^2} \\
&\quad + \frac{3}{8 \cos^4 \theta} \left[\frac{\left(1 + \left(\frac{d}{D}\right)^2\right) - 2 \sin^2 \theta}{\left(1 + \left(\frac{d}{D}\right)^2\right)^2 - \left(2 \left(\frac{d}{D}\right) \sin \theta\right)^2} + D^2 \psi_2 \right]
\end{aligned} \tag{4.7}$$

And ψ'_2 can be calculated as in the fully polarized transmitter case (on the subsection above). Then the $SNR^{(1)}$ can be calculated as:

$$SNR^{(1)} = \frac{2\psi'_2}{(D \cos \theta)^2} \frac{\psi'_4 - \sqrt{[\psi'_4 - 2 \cos(\theta)^2 \psi'_6]^2 + 4 \cos(\theta)^2 \psi'^2_5}}{(\psi'_4)^2 - [\psi'_4 - 2 \cos(\theta)^2 \psi'_6]^2 - 4 \cos(\theta)^2 \psi'^2_5} - 1 \tag{4.8}$$

Then, from that calculations we can assume the same for $SNR^{(2)}$ and we came to the conclusions that this can be expressed as:

$$SNR^{(1)} = \frac{2\psi'_2}{(D \cos \theta)^2} \frac{\psi'_4 + 3 \sqrt{[\psi'_4 - 2 \cos(\theta)^2 \psi'_6]^2 + 4 \cos(\theta)^2 \psi'^2_5}}{(\psi'_4)^2 - [\psi'_4 - 2 \cos(\theta)^2 \psi'_6]^2 - 4 \cos(\theta)^2 \psi'^2_5} - 1 \tag{4.9}$$

4.4.3 Steps

In this section we will explain how we calculated the number of active modes for both cases, which basically the asymptotic approximation values can be obtained from the formulas that we have seen in the section just before and the ones obtained from the channel has been calculated previously in the section of the optimum precoder.

So, on the one hand, to calculate the number of active modes from the channel:

- Calculate the distance and vector distance from each of the elements of the antenna array to the receiver equation (3.1).
- Calculate the transmit channel matrix equation (3.4).

- Concatenate all of the transmit channel matrix of the elements to form the transmit channel matrix of the system equation (3.11).
- Calculate the singular value decomposition of the transmit channel, from that we will use the right singular vector (V) and the singular values.
- From that we will get the positive coefficients $\sqrt{\rho_1}, \dots, \sqrt{\rho_{r_{pol}}}$.
- Once obtained ρ_i With waterfilling following equation (3.27), we will be able to calculate n_+ (which is our number of active modes). Note that the values to calculate n_+ are done with the ρ_i (singular values at the power of 2).

And on the other hand to calculate the number of active modes from the asymptotic approximation:

- Calculate the ψ_2 value from equation (3.34).
- Calculate the SNR_M from equation (3.32).
- Calculate the limits $SNR^{(1)}$ and $SNR^{(2)}$ for the corresponding case (fully polarization case equations (4.5) and (4.6) respectively and double polarization case equations (4.9) and (4.10) respectively).
- Now, with the limits and the SNR_M we can now calculate the number of active modes for the asymptotic approximation.
- Now we have the number of active modes for both, we can compare them and check that our approximation is working properly.

4.4.4 Results analysis

With the theoretical foundation established, we will now plot and analyze the results using MATLAB. We will plot the number of active modes in the two different cases and compare the results obtained with the asymptotic approximation.

To have and idea we can plot how is the form of the SNR_M and how the limits of both $SNR^{(1)}$ and $SNR^{(2)}$ behave. In the following figure we can see the SNR_M in blue, $SNR^{(1)}$ in red and $SNR^{(2)}$ in green for the case with a fully polarized transmitter.

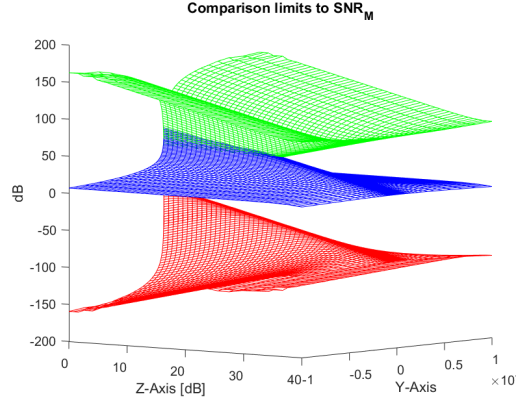


Figure 4.38: SNR_M comparison with limits.

4.4.4.1 Fully polarized transmitter

First, for the fully polarized transmitter, following the scenario definition above we plot the active modes across the space for both cases, obtained from the channel and with the asymptotic approximation, on the next figures we can see the results obtained for different points in the space.

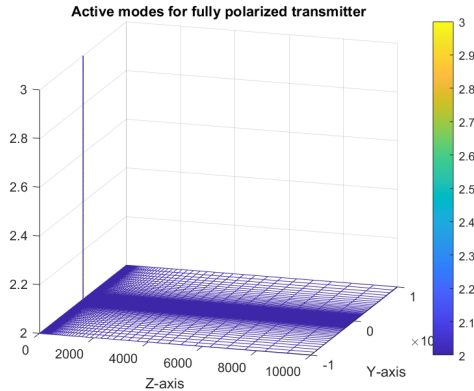


Figure 4.39: Activation modes in the space for $r_{pol} = 3, t_{pol} = 3$ (plot distance)

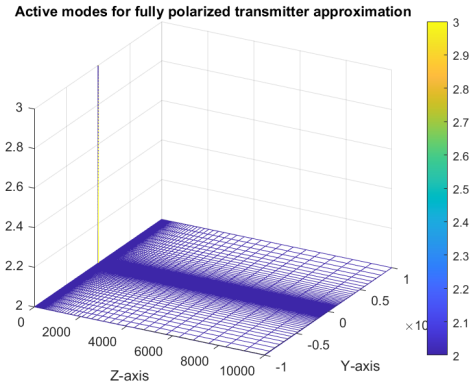


Figure 4.40: Activation modes in the space for $r_{pol} = 3, t_{pol} = 3$ (plot distance) with asymptotic approximation

With the figures we can see a similar behaviour, where near the antenna 3 modes are being active. Note, however, that this only happens really near the antenna, once we move a little bit farther just two of the modes are being active and it maintains these 2 modes active. With this particular case of fully polarized transmitter, looking at the powers associated to each mode, we can see that the power between the first mode and second mode are very similar, meanwhile

the power for the third mode is much lower, this allows to have 2 mode actives in most of the space since the power of them it divide equivalently for both of the modes.

To compare this case, we also can plot the mode activation versus the points (instead of the distance). This is just to compare better that the approximation is working. The grid that we have considered is a logarithmic scale with the same number of points for decade, in this case we considered from 1m to 10 km considering 20 points for decade. This particular visualization helps us to see that the activation modes for both cases is really similar, with the real visualization it's harder to see and verify this similarity to validate our asymptotic approximation.

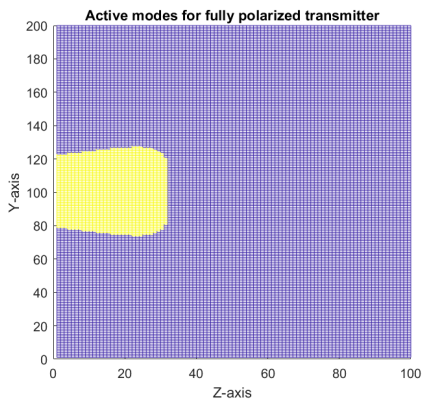


Figure 4.41: Activation modes in the space for $r_{pol} = 3, t_{pol} = 3$ (plot points)

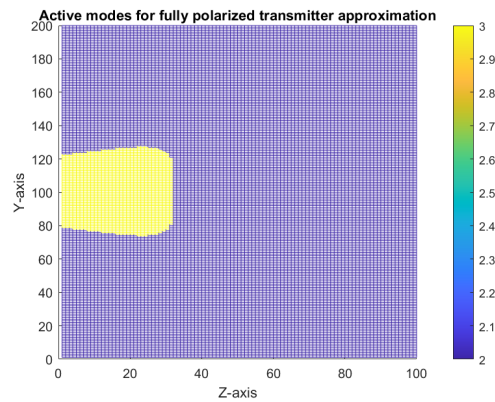


Figure 4.42: Activation modes in the space for $r_{pol} = 3, t_{pol} = 3$ (plot points) with asymptotic approximation

With this new graphic it's easier to verify that the behaviour on both cases is the same, since the asymptotic approximations is giving the same results than the calculated with the channel to calculate the optimum precoder for the fully polarized transmitter, we can verify that the approximation is working properly. This also, shows that the approximation is working also well near the antenna array not just far away, that allow us to work with that approximation in the future.

4.4.4.2 Double polarization transmitter

Now, for the double polarization transmitter we will plot the same graphics with side by side the obtained number of modes from the channel to calculate the optimum precoder and with the asymptotic approximation:

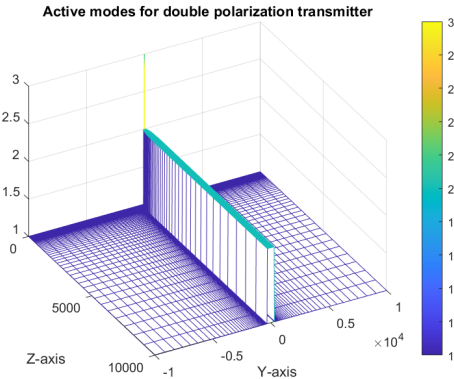


Figure 4.43: Activation modes in the space for $r_{pol} = 3, t_{pol} = 2$ (plot distance)

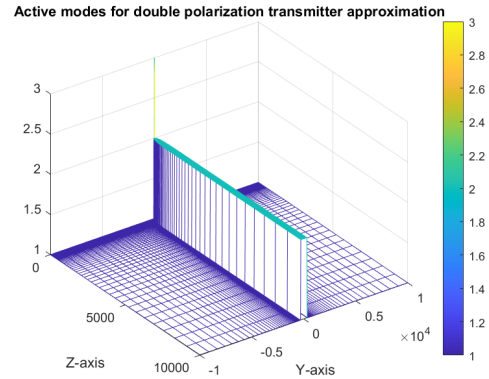


Figure 4.44: Activation modes in the space for $r_{pol} = 3, t_{pol} = 2$ (plot distance) with asymptotic approximation

With the figures 4.43 and 4.44 we can see that the number of active modes in this case varies between 1 and 3 instead of the minimum being 2 like in the fully polarized case.

Near the antenna array, the number of active nodes is 3 as in the previous case. We can also see that alongside the perpendicular direction of the antenna array (situate along the y-axis with center at the origin of coordinates) the number of active modes it maintains to two, while in other directions the number active modes it goes down to 1.

As in the previous case, we will also see the plot for the points that we have taken instead of the distance since it will give us a better perspective to compare the asymptotic approximation and the number of active channels calculated from the optimum precoder.

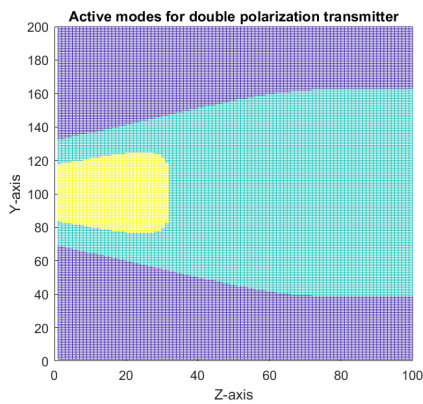


Figure 4.45: Activation modes in the space for $r_{pol} = 3, t_{pol} = 2$ (plot points)

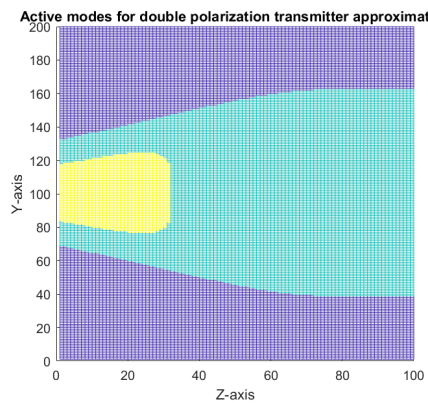


Figure 4.46: Activation modes in the space for $r_{pol} = 3, t_{pol} = 2$ (plot points) with asymptotic approximation

In this case, we can see that the results as in the previous case are the same, so we can validate that the approximation is working properly in this case also.

In MIMO systems the limit from Shannon's theorem is extended to instead of the number of antennas at each site, the number of antennas multiplied by the number of polarizations for the antennas. This with the simulated scenario simulated increase the number of simultaneous streams since for each one of the polarizations we can transmit or receive different signals.

With the graphics we can clearly see that the Shannon's theorem is being verified since the maximum number we are getting is 3 in the graphics and the theorem states that the maximum number of simultaneous streams in a communication system is determined by the minimum of the number of transmit antennas and receive antennas is being verified, since this maximum in our case is the number of polarizations on the receiver (3), since in the transmitter we have a lot of antennas.

4.4.5 Activation modes with power

Now, let us check how the activation modes change when the signal power is being changed for also both different transmitters, for a fixed SNR at a distance 100m. We will see the number of activated modes for the asymptotic approximation and the ones we obtain from the channel. This scenario was simulated with 501 antennas and the other conditions as the scenario configuration established before. It is important to note that despite we justified some power, we are seeing the behaviour when the power is modified, but not for realistic powers, since all this as we said before depend on some scale factors that can be modified.

Let's begin with the fully polarized transmitter where we showed 3 relevant cases:

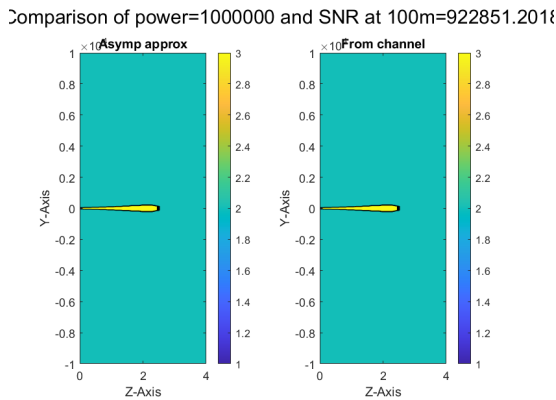


Figure 4.47: Activation modes in the space for $r_{pol} = 3, t_{pol} = 2$ with power 10^6 W

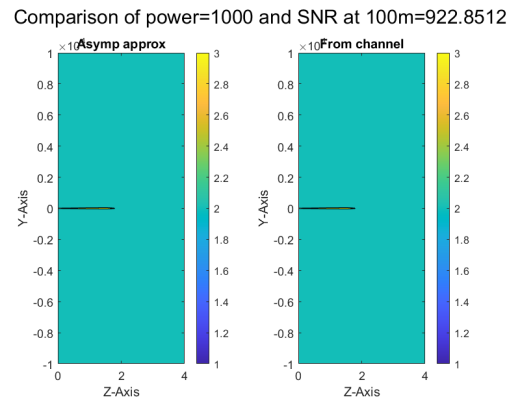


Figure 4.48: Activation modes in the space for $r_{pol} = 3, t_{pol} = 3$ with power 10^3 W

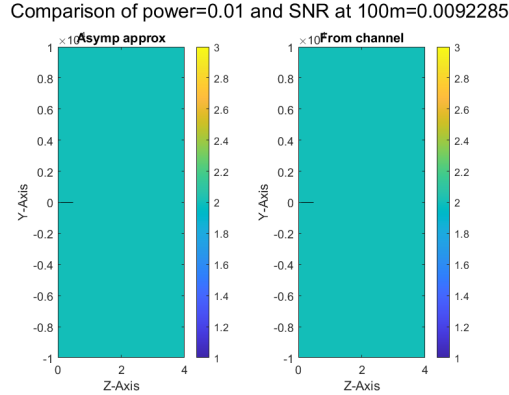


Figure 4.49: Activation modes in the space for $r_{pol} = 3, t_{pol} = 3$ with power 10^{-2} W

We can see that in all the space simulated the minimum number of modes active that we can find is 2, we can see that 3 activate near the antenna on a perpendicular direction from the antenna array from the center of the antenna array. When we decrease the power this region where 3 modes are being activated is smaller until it finally disappears. We can see that evolution from Figure 4.47 to Figure 4.49, in fact with that last case we can see that the region with 3 modes activated is almost 0 and if we decrease more the power it will finally disappear.

As we said before, with the channel that we have defined in the case $r_{pol} = t_{pol} = 3$ the contribution of power from the first 2 modes is almost the same, that leads to what we've seen that 2 modes at least are maintained active.

Now, let's take a look on the case with double polarization transmitter:

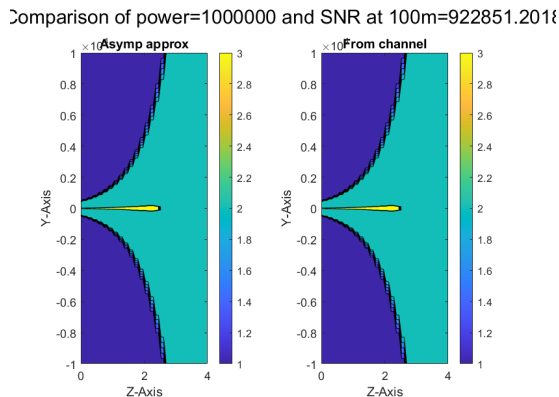


Figure 4.50: Activation modes in the space for $r_{pol} = 3, t_{pol} = 2$ with power 10^6 W

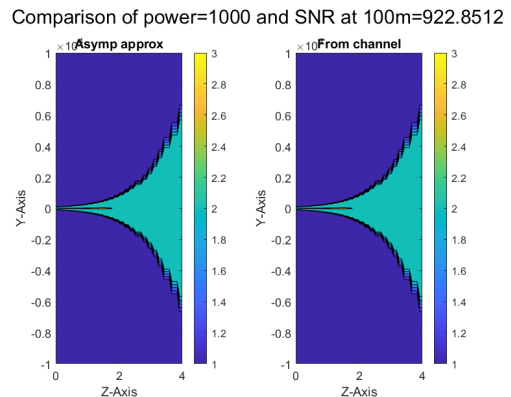


Figure 4.51: Activation modes in the space for $r_{pol} = 3, t_{pol} = 2$ with power 10^3 W

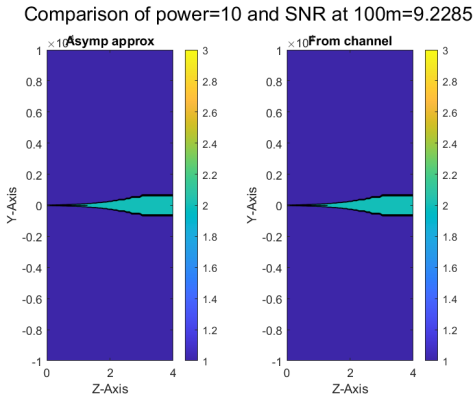


Figure 4.52: Activation modes in the space for $r_{pol} = 3, t_{pol} = 2$ with power 10 W

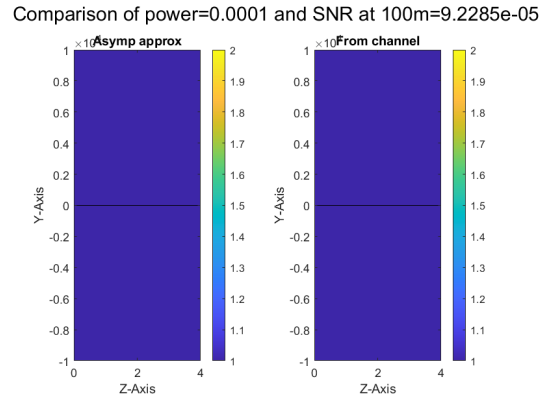


Figure 4.53: Activation modes in the space for $r_{pol} = 3, t_{pol} = 2$ with power 10^{-4} W

Similarly to before when we have a more power we can see that we have a region from the center of the antenna array and perpendicular to it, where 3 modes are active. In this region when the power is decreased also it becomes smaller, but this time it becomes smaller faster than in the fully polarized case. Differently than in the previous case, we can see that not all the time they are 2 active modes at least, we can see some regions where only one mode is active. We can see that the region where 2 modes are active at least goes from the center of the antenna array and it expands along the space from it. When the power is diminished this region tends to a focus beam in the direction perpendicular to the antenna array until it finally becomes for all the space only one mode active.

This behavior indicates that power levels and polarization significantly impact the spatial distribution and active modes for ELAAs, at a higher power more modes they activate and having 3 polarizations at the transmitter instead of 2 guarantees that we will have at least two modes active. For the case of two polarizations we observe 2 active modes at the most of the space, this also affects to the 3 active modes, when we have 3 polarizations, we won't need that much power to achieve 3 available active modes.

So, as we seen we will have more chances to have more polarizations at that perpendicular line to the antenna array, so it will be a good idea to put the users in that perpendicular line to be able to serve more of them or increase the available bit-rate for them. This would not always will be possible because in general we won't know the positions of the receiver and it will depend on the application that is being used, it will only be possible in the case where the receiver and transmitter are always fixed and before the installation this position is known.

Chapter 5

Conclusions

In this project, we considered an ELAA transmitter with multiple polarizations and a fully polarized receiver working in the near field. For that scenario, we developed and verified some closed-form holographic asymptotic approximations for a case where we use an optimal precoder of ELAAs to maximize capacity. We calculated some parameters that will give us insights into how the system would work once designed in the established conditions. This approximation will also help to calculate the required parameters for that configuration, as the eigenvalues calculated can be used to define the optimal precoder (W).

First, we analyzed the behavior in terms of capacity of our CSI optimal precoder (assuming the transmitter knows the transmit channel), which showed us we can build a system with high capacity at a defined point, where the receiver is located, but very low capacity at other points in the space. This is related to other studies showing that the normalized gain of our optimal precoder is capable of distributing high power to the receiver and very low power in other directions, allowing for very low interference to other users.

Then, we developed and validated numerically that our holographic approximation for the eigenvalues of the channel works with very low error for a large number of antennas. We've seen that these approximations work not only far from the antenna but also near the antenna array, ensuring us that this approximation can be used at any point in space for any system that is required to be built or analyzed for a significant number of antenna elements.

We also developed closed-form expressions to determine the number of active modes with an asymptotic approximation and compared the results to the number of active modes obtained when building the channel. We could see that these approximations work with high precision at any point in space. We also studied how the different modes activate along the space and observed that, to maximize the number of active modes, it is required that the user is in a perpendicular position to the ELAA from its center. Additionally, with the approximations developed,

we can estimate how the channel will behave with a less computational costly equations.

We also compared the behavior of the system when working with a fully polarized transmitter and a double polarization transmitter. We could see that with the first case, we obtained better results with higher capacity and allowed working with lower power to achieve the same behavior along the space. The difference was especially noticeable while studying the number of active modes (which gives us information on the number of simultaneous streams at a certain location, relating it with Shannon's theorem). The fully polarized setup guarantees having two simultaneous streams in most of the space without needing to imply much power. Achieving two polarizations was particularly difficult with the double polarization case at positions just above or below the antenna array.

Based on these results, we can conclude that to maximize the number of parallel streams, we need to work with the maximum number of polarizations possible, although that with enough power it will be possible to have similar behaviour. The holographic approximations carried on will give us some closed form to estimate the behaviour of ELAAs and help us to calculate their precoder that will be valid when the antenna array has a large number of antennas, but it will also be valid when this number is not that huge. And also, we can conclude that using the optimal precoder in terms of capacity we are able to beamfocus the signal to a certain power without compromising communication systems at other points in the space.

As future lines, it can be explored more in detail how the number of antennas affect the accuracy of this approximations, how the distance and direction affect directly the number of modes active at any point in the space and compare the whole behaviour with other polarization's configurations such as having a receiver with two orthogonal dipoles.

Bibliography

- [AA24] Xavier Mestre Adrian Agustin, “Polarized near-field beamfocusing in xl-mimo”, *To be submitted to IEEE Transactions on Wireless Communications*, 2024.
- [Agu23] Adrian Agustin, Xavier Mestre, “Near-field beamfocusing with polarized antennas”, 11 2023.
- [An23a] Jiancheng An, Chau Yuen, Chongwen Huang, Mérouane Debbah, H Poor, Lajos Hanzo, H Vincent, “Holographic mimo communications, performance analysis, holographic beamforming, near-field communications”, 2023.
- [An23b] Jiancheng An, Chau Yuen, Chongwen Huang, Mérouane Debbah, H Poor, Lajos Hanzo, H Vincent, “A tutorial on holographic mimo communications-part i: Channel modeling and channel estimation”, 2023.
- [Bj1] Emil Björnson, Özlem Demir, Luca Sanguinetti, “A primer on near-field beamforming for arrays and reconfigurable intelligent surfaces”, 10 2021.
- [Com] “Compensation for signal loss at higher frequencies”, .
- [Cui22] Mingyao Cui, Wu Zidong, Yu Lu, Xiuhong Wei, Linglong Dai, “Near-field communications for 6g: Fundamentals, challenges, potentials, and future directions”, 03 2022.
- [Dai20] Linglong Dai, Marco Di Renzo, Chan-Byoung Chae, L. Hanzo, Bichai Wang, Min Wang, Xue Yang, Jingbo Tan, Shuangkaisheng Bi, Shenheng Xu, Fan Yang, Zhi Chen, “Reconfigurable intelligent surface-based wireless communications: Antenna design, prototyping, and experimental results”, *IEEE Access*, Vol. PP, pags. 1–1, 03 2020.
- [Dir] “Directional radiation pattern, adaptive beamforming, interference rejection”, .
- [Gon23] Tierui Gong, Panagiotis Gavriilidis, Ran Ji, Huang Chongwen, George Alexopoulos, Li Wei, ZhaoYang Zhang, mérouane Debbah, H. Vincent Poor, Chau Yuen, “Holographic mimo communications: Theoretical foundations, enabling technologies, and future directions”, 04 2023.

- [He24] Zhenyao He, Wei Xu, Zhaohui Yang, Hong Shen, Ningning Fu, Yongming Huang, Zhaoyang Zhang, Xiaohu You, “Unlocking potentials of near-field propagation: Elaa-empowered integrated sensing and communication”, 04 2024.
- [Li22] An Li, Shi-Wei Qu, Shiwen Yang, “Conformal array antenna for applications in wide-scanning phased array antenna systems”, *IEEE Antennas and Wireless Propagation Letters*, Vol. 21, n° 9, pags. 1762–1766, 2022.
- [Liu24] Hao Liu, Tianci Guan, Chunsen Fu, Shuqi Zhang, Xin Xu, Ziqiang Xu, Anyong Qing, Xianqi Lin, “Improving scanning performance of patch phased array antenna by using a modified siw cavity and sequential rotation technique”, *Electronics*, Vol. 13, pags. 1776, 05 2024.
- [Lu21] Haiquan Lu, Yong Zeng, “Communicating with extremely large-scale array/surface: Unified modeling and performance analysis”, *IEEE Transactions on Wireless Communications*, Vol. PP, pags. 1–1, 11 2021.
- [Mar19] Thomas Marzetta, “Super-directive antenna arrays: Fundamentals and new perspectives”, pags. 1–4, 11 2019.
- [Mon23] Mehdi Monemi, Mohammad Amir Fallah, Mehdi Rasti, Matti Latva-aho, Mérourane Debbah, “Towards near-field 3d spot beamfocusing: Possibilities, challenges, and use-cases”, *ArXiv*, Vol. abs/2401.08651, 2023.
- [Ram23] Parisa Ramezani, Alva Kosasih, Amna Irshad, Emil Björnson, “Exploiting the depth and angular domains for massive near-field spatial multiplexing”, *IEEE BITS the Information Theory Magazine*, Vol. 3, pags. 14–26, 03 2023.
- [Shl21] Nir Shlezinger, George Alexandropoulos, Mohammadreza Imani, Yonina Eldar, D. Smith, “Dynamic metasurface antennas for 6g extreme massive mimo communications”, *IEEE Wireless Communications*, Vol. PP, pags. 1–8, 01 2021.
- [Wei22] Li Wei, Chongwen Huang, George C. Alexandropoulos, Zhaohui Yang, Jun Yang, Wei E. I. Sha, Zhaoyang Zhang, Merouane Debbah, Chau Yuen, “Tri-polarized holographic mimo surface in near-field: Channel modeling and precoding design”, 11 2022.
- [Zha22] Haiyang Zhang, Nir Shlezinger, Francesco Guidi, Davide Dardari, Mohammadreza Imani, Yonina Eldar, “Beam focusing for near-field multiuser mimo communications”, *IEEE Transactions on Wireless Communications*, Vol. 21, pags. 1–1, 09 2022.
- [Zhu23] Lipeng Zhu, Wenyan Ma, Rui Zhang, “Movable-antenna array enhanced beamforming: Achieving full array gain with null steering”, *IEEE Communications Letters*, Vol. 27, pags. 3340–3344, 12 2023.

Appendices

5.1 Matlab code used

Here you can find the Matlab Code used for the numerical validation.

```
1 % Define antenna array properties
2 number_ant_tx = 1001; % Number
3 % transmitters
4 ant_rx = 1; % Number receivers
5 frequency = 6*10^9; % Transmit frequency
6 wavelength = 3*10^8 /frequency; % Calculate
7 separation_tx_antennas = 0.1*wavelength; % Define eparation between
8 % transmitters antenna elements from the array.
9 flag_2_channels = 1;
10 % To Fix relation between separation between antennas and number
11 % of antennas
12 % start_decade_sep = 0; % 10^1 = 10
13 % end_decade_sep = 5; % 10^20 = 10000
14 % num_antennes_array = [10.^ [start_decade_sep+1:end_decade_sep]'
```

```

    * [0.1 0.2 0.5] ]';

15 % num_antennes_array = num_antennes_array(:)';
16 % sep_array = 5000./num_antennes_array;
17
18
19 % Define points for the receiver component Y and Z
20 % Receiver position
21 % y_antenna_rx_pos = 4; z_antenna_rx_pos = 3;
22 start_decade = 0; % 10^1 = 10
23 end_decade = 4; % 10^20 = 10000
24
25 % Specify the number of points per decade
26 num_points_per_decade = 20;
27
28 % Generate the logarithmically spaced vector
29 z_axis = logspace(start_decade, end_decade, num_points_per_decade
    * (end_decade - start_decade + 1));
30 y_axis = [-1*logspace(start_decade, end_decade,
    num_points_per_decade * (end_decade - start_decade + 1)) ,
    logspace(start_decade, end_decade, num_points_per_decade * (
        end_decade - start_decade + 1))];
31 y_axis = sort(y_axis);
32
33 % Define TX antenna position
34 % We suppose transmissions antenas at the origin coordinates y=0
35 y_antennas_tx_pos = -floor(number_ant_tx/2)*
    separation_tx_antennas:separation_tx_antennas:floor(
    number_ant_tx/2)*separation_tx_antennas;
36 z_antennas_tx_pos = 0;
37
38 alpha_m = 1;
39 beta_m = 1;
40 %impedance free space
41 scale_impedance_factor = (1i)*1/2;
42 noise_power = 1;
43 signal_power = 1*10^(0);
44 %%%%%%%%%%%%%%%%
45 % TO ANALYSE FOR DIFFERENT POWERS AND EIGENVALUES APPROX

```

```
46
47
48 matrix_Sigma = zeros(length(y_axis), length(z_axis), 3);
49 matrix_eigenvalues_channel = zeros(length(y_axis), length(z_axis)
    , 3);
50 matrix_eigenvalues_channel_approx = zeros(length(y_axis), length(
    z_axis), 3);
51 matrix_limits = zeros(length(y_axis), length(z_axis), 2);
52 matrix_n_from_SNR = zeros(length(y_axis), length(z_axis));
53 matrix_capacity = zeros(length(y_axis), length(z_axis));
54 matrix_W_compare = zeros(length(y_axis), length(z_axis), 9);
55 matrix_eigenvalues_compare= zeros(length(y_axis), length(z_axis)
    ,3);
56 matrix_SNR_M = zeros(length(y_axis), length(z_axis));
57
58
59 % [n_plus_value,lambda_rpol, SNR,Sigma,P_matrix, V,
60 % transmit_channel] = calculate_activation_modesDepending_pos(
61 % y_antennas_tx_pos, z_antennas_tx_pos, 2, 2, number_ant_tx,
62 % scale_impedance_factor, wavelength, alpha_m, beta_m,
63 % signal_power, noise_power, flag_2_channels);
64 % W_precoder = V * P_matrix;
65 for signal_power=10.^{0:1:0}
66     for y_index=1:length(y_axis)
67         for z_index = 1:length(z_axis)
68             [n_plus_value,lambda_rpol, SNR,Sigma,P_matrix, V,
69              transmit_channel] =
70                 calculate_activation_modesDepending_pos(
71                 y_antennas_tx_pos, z_antennas_tx_pos, y_axis(
72                     y_index), z_axis(z_index), number_ant_tx,
73                     scale_impedance_factor, wavelength, alpha_m, beta_m
74                     , signal_power, noise_power, flag_2_channels);
75             %transmit_channel = calculate_transmit_channel(
76             %y_antennas_tx_pos, z_antennas_tx_pos,y_axis(y_index)
77             %), z_axis(z_index), number_ant_tx,
78             %scale_impedance_factor, wavelength, alpha_m, beta_m
79             %, flag_2_channels);
```

```

67     matrix_n(y_index,z_index) = n_plus_value;
68     matrix_eigenvalues_channel(y_index,z_index,:) = sort(
69         eig(transmit_channel*transmit_channel'), 'descend')
70         ;
71     matrix_SNR(y_index,z_index) = SNR;
72     matrix_Sigma(y_index,z_index,:) = diag(Sigma);
73     %           matrix_capacity(y_index,z_index) =
74     % calculate_capacity(noise_power, W_precoder, transmit_channel
75     );
76
77     [W_Green] = calculate_WGreen_matrix(y_antennas_tx_pos
78         , z_antennas_tx_pos, y_axis(y_index), z_axis(
79             z_index), number_ant_tx, flag_2_channels);
80
81     [W_calculated_D,angle, auxiliardD, D, value2,
82         matrix_eigenvalues_channel_approx(y_index,z_index
83         ,:)] = calculate_W_matrix(y_antennas_tx_pos,
84         z_antennas_tx_pos,y_axis(y_index), z_axis(z_index),
85         flag_2_channels);
86
87     %
88         COMPARE W MATRIXES
89
90     W_comparison = compare_matrixs(W_Green,
91         W_calculated_D);
92
93     W_comparison(isnan(W_comparison))=0;
94     %matrix_W_compare(y_index,z_index,:)=reshape(
95     %W_comparison,[9,1]);
96
97     %
98         COMPARE EIGENVALUES
99
100
101    matrix_eigenvalues_compare(y_index,z_index,:) =
102        matrix_eigenvalues_channel(y_index,z_index,:)./
103        matrix_eigenvalues_channel_approx(y_index,z_index
104        ,:);
105
106    %
107        COMPARE LIMITS
108
109
110    [matrix_limits(y_index,z_index,1),matrix_limits(
111        y_index,z_index,2)] = calculate_limit(auxiliardD,
112        angle,flag_2_channels);
113
114    P_aux = signal_power * (number_ant_tx);

```

```
88     matrix_SNR_M(y_index,z_index) = P_aux/(noise_power) *
89         abs(scale_impedance_factor/wavelength)^2*value2;
90
91     matrix_n_from_SNR(y_index,z_index) =
92         get_n_from_limits(matrix_SNR_M(y_index,z_index),
93             matrix_limits(y_index,z_index,1),matrix_limits(
94                 y_index,z_index,2));
95
96
97
98
99
100
101
102
103
104
105
106
107
108
109    sgtitle(['Comparison of power=' , num2str(signal_power), ' and
110          SNR at 100m=' , num2str(matrix_SNR_M(length(y_axis)/2+1,
111          num_points_per_decade*(3-start_decade)))]);
112
113
114
115
116
117
118
119 % %%%%%% To plot capacity
```

```

120 % ylabel('Z-axis (log scale)');
121 % zlabel('Capacity');
122 % title('Capacity for 3x3 with optimum precoder at each point');
123 % colorbar;
124
125
126
127 %
%%%%%%%%%%%%%%%
128 % Compare W and Eigenvalues with fixed d*Num_Ant
129 %
130 % matrix_eigenvalues_channel_approx = zeros(length(
131 %     num_antennes_array), 3);
132 % matrix_eigenvalues_channel = zeros(length(num_antennes_array),
133 %     3);
134 % matrix_W_compare = zeros(length(num_antennes_array), 1);
135 %
136 % y_antenna_rx_pos = 3; z_antenna_rx_pos = 3;
137 % for index_rel_antennas_sep=1:length(num_antennes_array)
138 %
139 %     separation_tx_antennas=sep_array(index_rel_antennas_sep)*
140 % wavelength;
141 %     number_ant_tx=num_antennes_array(index_rel_antennas_sep)+1;
142 %     y_antennas_tx_pos = -floor(number_ant_tx/2)*
143 % separation_tx_antennas:separation_tx_antennas:floor(
144 %     number_ant_tx/2)*separation_tx_antennas;
145 %     z_antennas_tx_pos = 0;
146 %     transmit_channel = calculate_transmit_channel(
147 %         y_antennas_tx_pos, z_antennas_tx_pos, y_antenna_rx_pos,
148 %         z_antenna_rx_pos, number_ant_tx, scale_impedance_factor,
149 %         wavelength, alpha_m, beta_m, flag_2_channels);
150 %
151 %     matrix_eigenvalues_channel(index_rel_antennas_sep,:) = sort(
152 %         eig(transmit_channel*transmit_channel')./number_ant_tx./abs(
153 %             scale_impedance_factor/wavelength)^2, 'descend');
154 %
155 %     [W_Green] = calculate_WGreen_matrix(y_antennas_tx_pos,
156 %         z_antennas_tx_pos, y_antenna_rx_pos, z_antenna_rx_pos,
157 %         number_ant_tx, flag_2_channels);

```

```
144 % [W_calculated_D,angle, auxiliardD, D, value2,
145 % matrix_eigenvalues_channel_approx(index_rel_antennas_sep,:)] =
146 % calculate_W_matrix(y_antennas_tx_pos, z_antennas_tx_pos,
147 % y_antenna_rx_pos, z_antenna_rx_pos, flag_2_channels);
148 % matrix_W_compare(index_rel_antennas_sep)=compare_matrixs(
149 % W_Green, W_calculated_D);
150 %
151 % end
152 % figure();
153 % loglog(num_antennes_array, sqrt(abs(matrix_W_compare)));
154 % %plot(10*log10(num_antennes_array),matrix_W_compare);
155 % xlabel('Number of antennas [dB]');
156 % xlabel('Number of antennas [dB]');
157 % title("Error on W asymptotic approx.");
158 %
159 %
160 % figure();
161 % loglog(num_antennes_array,abs(matrix_eigenvalues_channel(:,1)-
162 % matrix_eigenvalues_channel_approx(:,1)) )
163 % %plot(num_antennes_array,(matrix_eigenvalues_channel(:,1)-
164 % matrix_eigenvalues_channel_approx(:,1))./
165 % matrix_eigenvalues_channel(:,1));
166 % xlabel('Number of antennas [dB]');
167 % xlabel('Number of antennas [dB]');
168 % title("Error on eigenvalue 1 asymptotic approx.");
169 %
170 % figure();
```

```

171 % loglog(num_antennes_array , abs(matrix_eigenvalues_channel (:,3)-
172 matrix_eigenvalues_channel_approx(:,3)))
173 % %plot(10*log10(num_antennes_array),10*log10((
174 matrix_eigenvalues_channel(:,3)-
175 matrix_eigenvalues_channel_approx(:,3))./
176 matrix_eigenvalues_channel(:,3)));
177 % xlabel('Number of antennas [dB]');
178 % xlabel('Number of antennas [dB]');
179 % title("Error on eigenvalue 3 asymptotic approx.");
180
181 function C = calculate_capacity(noise_power, W, H)
182 % Function to calculate capacity from general form given
183 % noise_power, W
184 % (precoder) matrix and H (transmit channel matrix)
185 C= abs(log10(det(eye(3)+ 1/noise_power* H*W*W'*H')));
186 end
187
188 function n = get_n_from_limits(SNR, n1_limit, n2_limit)
189 % Function to calculate the number of active modes given SNR
190 % (SNR_M),
191 % n1_limit (first limit) and n2_limit (second limit)
192
193 %  

194 %  

195 %  

196 %  

197 %  

198
199 function [limit_n1,limit_n2] = calculate_limit(auxiliar_dD, angle
200 , flag_2_channels)
201 % Function to calculate the limits for active modes given d/D
202 , angle of

```

```
201 % the receiver, and a flag_2_channels to indicate the number
202 % of
203 % polarizations at the transmitter.
204 if auxiliar_dD < 1
205     value2_subD2 = 1/ (2*auxiliar_dD*cos(angle)) * atan(2*
206         auxiliar_dD*cos(angle)/(1-auxiliar_dD^2));
207 elseif auxiliar_dD == 1
208     value2_subD2 = 1/ (2*auxiliar_dD*cos(angle))*(pi/2);
209 elseif auxiliar_dD > 1
210     value2_subD2 = 1/ (2*auxiliar_dD*cos(angle)) *( pi +
211         atan(2*auxiliar_dD*cos(angle)/(1-auxiliar_dD^2)));
212 end
213
214 if flag_2_channels ==0
215
216
217 else
218
219     value4_subD2 = 1/(2*cos(angle)^2) * (((1+auxiliar_dD^2) -
220         2 *sin(angle)^2)/ ((1+auxiliar_dD^2)^2 - (2*
221         auxiliar_dD*sin(angle))^2 ) + value2_subD2 );
222     value5_subD2 = -(sin(angle) *(1+auxiliar_dD^2)) /((1+
223         auxiliar_dD^2)^2-(2*auxiliar_dD*sin(angle))^2)^2;
224     value6_part_subD2 = ((1+auxiliar_dD^2)^2-4*sin(angle)^2)
225         /((1+auxiliar_dD^2)^2-(2*auxiliar_dD*sin(angle))^2)^2;
226
227     value6_subD2 = 1/(4*cos(angle)^2)*(value6_part_subD2) +
228         1/(4*cos(angle)^2)*(3*value4_subD2);
229
230
231 %limit_n1 = (2*value2_subD2/(cos(angle)^2))*(1/(
232     value4_subD2+sqrt((value4_subD2-2*cos(angle)^2*
```

```

    value6_subD2)^2+4*(cos(angle))^2*value5_subD2^2 ))))-1;
227 limit_n1 = ((2*value2_subD2/(cos(angle)^2))*(value4_subD2
- (1)*sqrt((value4_subD2-2*cos(angle)^2*value6_subD2)
^2+4*cos(angle)^2*value5_subD2^2))/ ...
228     (value4_subD2^2-(value4_subD2-2*cos(angle)^2*
value6_subD2)^2-4*cos(angle)^2*value5_subD2^2))-1;
229 %
230 limit_n2 = ((2*value2_subD2/(cos(angle)^2))*(value4_subD2
+ (3)*sqrt((value4_subD2-2*cos(angle)^2*value6_subD2)
^2+4*cos(angle)^2*value5_subD2^2))/ ...
231     (value4_subD2^2-(value4_subD2-2*cos(angle)^2*
value6_subD2)^2-4*cos(angle)^2*value5_subD2^2))-1;
232 end
233
234 end
235
236
237 function [W,angle, auxiliardD, D, value2, eigenvalues] =
238 calculate_W_matrix(y_antennas_tx_pos, z_antennas_tx_pos,
y_antenna_rx_pos, z_antenna_rx_pos, flag_2_channels)
239
% Function to calculate the W being the  $W_{\text{caligraphic}}$  from
240 % the system,
241 % relation  $d/D$  being  $D$  distance to the receiver (also
242 % returned) and  $d$ 
243 % the length of half of the antenna array , parameter  $\psi_2$ 
244 % and the eigenvalues given receiver and antenna elements
245 % positions
246 d = abs(max(y_antennas_tx_pos) - min(y_antennas_tx_pos))/2;
247 dy = abs(y_antenna_rx_pos - ((max(y_antennas_tx_pos) - min(
y_antennas_tx_pos))/2+ min(y_antennas_tx_pos)));
248 dz = abs(z_antenna_rx_pos - z_antennas_tx_pos );
249 D = sqrt(dy^2 + dz^2);
250 angle = atan(dy/ +dz);
251 auxiliardD = d/D;

if d < D
    value2 = 1/ (2*d*D*cos(angle)) * atan(2*D*d*cos(angle)/(D

```

```

        ^2-d^2));
252
253    elseif d == D
254        value2 = 1/ (2*d*D*cos(angle))*(pi/2);
255    else
256        value2 = 1/ (2*d*D*cos(angle)) *( pi + atan(2*D*d*cos(
257            angle)/(D^2-d^2)));
258
259    value3 = -D* sin(angle)/((D^2+d^2)^2-(2*d*D*sin(angle))^2);
260    value4 = 1/2 * 1/(D*cos(angle))^2 * ((D^2+d^2)-2*D^2*sin(
261        angle)^2)/((D^2+d^2)^2 - (2*d*D*sin(angle))^2)+ value2/(2*(D*
262            cos(angle))^2);
263
264    eigenvalue1 = value2;
265    if flag_2_channels == 0
266
267        eigenvalue2 = (1/2)* (value2 +1/sqrt((D^2-d^2)^2 + (2*d*D
268            *cos(angle))^2));
269        eigenvalue3 = (1/2)* (value2 -(1/sqrt((D^2-d^2)^2 + (2*d*
270            D*cos(angle))^2)));
271        eigenvalues = [eigenvalue1, eigenvalue2, eigenvalue3];
272
273    else
274        eigenvalue2 = 0.5*((D*cos(angle))^2)*(value4 + sqrt((
275            value4-2*(D*cos(angle))^2*value6)^2 + (2*(D*cos(angle))
            *value5)^2));
276        eigenvalue3 = 0.5*((D*cos(angle))^2)*(value4 - sqrt((

```

```

        value4-2*(D*cos(angle))^2*value6)^2 + (2*(D*cos(angle))
        *value5)^2));
276 eigenvalues = [eigenvalue1, eigenvalue2, eigenvalue3];
277 W = [value2 0 0; 0 value6*D^4*cos(angle)^4 value5*D^3*cos
        (angle)^3; 0 value5*D^3*cos(angle)^3 value4*D^2*cos(
        angle)^2-value6*D^4*cos(angle)^4];
278 end
279
280
281 end
282
283 function [W_Green] = calculate_WGreen_matrix(y_antennas_tx_pos,
        z_antennas_tx_pos, y_antenna_rx_pos, z_antenna_rx_pos,
        number_ant_tx, flag2_channels)
284 % Function to calculate W_caligraphic from the channel.
285 W_Green = zeros(3);
286 for m_antenna_number = 1:number_ant_tx
287     distance_vector_m =
        calculate_distance_vector_to_m_antenna(m_antenna_number
        ,y_antenna_rx_pos,z_antenna_rx_pos,y_antennas_tx_pos,
        z_antennas_tx_pos);
288     distance_m = calculate_distance_to_m_antenna(
        m_antenna_number, y_antenna_rx_pos,z_antenna_rx_pos,
        y_antennas_tx_pos,z_antennas_tx_pos);
289
290     P = eye(3) - distance_vector_m * distance_vector_m';
291     if flag2_channels == 1
292         P = P(:,1:2);
293     end
294     W_Green = W_Green + 1/(number_ant_tx) * 1/(distance_m)^2
        * P*P';
295
296 end
297
298 end
299
300 function [n_plus_value,lambda_rpol, SNR, Sigma_sqr,P_matrix, V,
        transmit_channel] = calculate_activation_modesDepending_pos(

```

```

y_antennas_tx_pos, z_antennas_tx_pos, y_antenna_rx_pos,
z_antenna_rx_pos, number_ant_tx, impedance, wavelength, alpha_m
, beta_m, signal_power, noise_power, flag_2_channels)
301 transmit_channel = calculate_transmit_channel(
    y_antennas_tx_pos, z_antennas_tx_pos, y_antenna_rx_pos,
    z_antenna_rx_pos, number_ant_tx, impedance, wavelength,
    alpha_m, beta_m, flag_2_channels);
302 % it will appear a scale factor difference
303 % correct this with the following correction
304 % transmit_channel = transmit_channel *(abs(wavelength/
    impedance)*1/sqrt(number_ant_tx));
305
306 [U,Sigma_aux,V_aux] = svd(transmit_channel);
307
308 len_Sigma=length(Sigma_aux(:,1));
309
310 Sigma_sqr = Sigma_aux(1:len_Sigma,1:len_Sigma);
311 V = V_aux(:,1:len_Sigma);
312
313
314 SNR = trace(transmit_channel*ctranspose(transmit_channel))/
    noise_power;
315 [n_plus_value, lambda_rpol] = find_n_plus_value(Sigma_sqr.^2,
    signal_power, noise_power);
316
317 rho_values=diag(Sigma_sqr);
318 rho_values(n_plus_value+1:end)=0;
319 Sigma_sqr = diag(rho_values);
320 p_values = 1/lambda_rpol -noise_power./rho_values;
321 p_values(n_plus_value+1:end)=0;
322 P_matrix = diag(p_values);
323 end
324 function [n_plus_value, lambda_rpol] = find_n_plus_value(Sigma,
    signal_power, noise_power)
325 % Function to obtain n_+ and lambda_rpol doing the
    waterfilling
326 % solution to calculate the optimal precoder
327 n_plus_value = 1;

```

```
328
329     for n=1:length(Sigma)
330         max_lambda_value = 1/n * signal_power;
331         for n_aux=1:n
332             max_lambda_value = max_lambda_value + 1/n *(
333                 noise_power / Sigma(n_aux,n_aux));
334             end
335             max_limit = (noise_power / Sigma(n,n));
336             if max_limit >= max_lambda_value
337                 break;
338             else
339                 n_plus_value = n; lambda_rpol = max_lambda_value;
340             end
341         end
342         lambda_rpol = 1/lambda_rpol;
343
344 end
345
346 function transmit_channel = calculate_transmit_channel(
347     y_antennas_tx_pos, z_antennas_tx_pos, y_antenna_rx_pos,
348     z_antenna_rx_pos, number_ant_tx, impedance, wavelength, alpha_m
349     , beta_m, flag_2_channels)
350     % Function to calculate whole transmit channel
351
352     transmit_channel = [];
353     for m_antenna_number = 1:number_ant_tx
354         distance_vector_m =
355             calculate_distance_vector_to_m_antenna(m_antenna_number
356             ,y_antenna_rx_pos,z_antenna_rx_pos,y_antennas_tx_pos,
357             z_antennas_tx_pos);
358
359         distance_m = calculate_distance_to_m_antenna(
360             m_antenna_number, y_antenna_rx_pos,z_antenna_rx_pos,
361             y_antennas_tx_pos,z_antennas_tx_pos);
362
363         transmit_channel_m = calculate_transmit_channel_m(
364             distance_vector_m, distance_m, impedance, wavelength,
365             alpha_m, beta_m);
```

```
355     if flag_2_channels == 1
356         transmit_channel = horzcat(transmit_channel,
357                                     transmit_channel_m(:,1:2));
357     else
358         transmit_channel = horzcat(transmit_channel,
359                                     transmit_channel_m);
359     end
360 end
361
362
363
364 function transmit_channel_m = calculate_transmit_channel_m(
365     distance_vector_m, distance_m, impedance, wavelength, alpha_m,
366     beta_m)
367     % Function to calculate the transmit channel from the m
368     % antenna element
369     % to the receiver
370     H_aux_m = alpha_m * eye(3) - beta_m * distance_vector_m *
371     ctranspose(distance_vector_m);
372     transmit_channel_m = impedance / (wavelength * distance_m) *
373     exp(-1i * 2 * pi* distance_m/ wavelength ) * H_aux_m;
374 end
375
376
377
378
379 function distance_vector_to_m_antenna =
400     calculate_distance_vector_to_m_antenna(m, y_rx_pos, z_rx_pos,
401     y_antenna_tx_pos, z_antenna_tx_pos)
402     % Function to calculate the unitary vector from m antenna
403     % element on the
404     % array to receiver
405     distance_to_m_antenna = calculate_distance_to_m_antenna(m,
406     y_rx_pos, z_rx_pos, y_antenna_tx_pos, z_antenna_tx_pos);
407     distance_vector_to_m_antenna = [0; (y_rx_pos -
408     y_antenna_tx_pos(m))/distance_to_m_antenna; (z_rx_pos -
409     z_antenna_tx_pos)/distance_to_m_antenna];
410 end
411
412
413
414
415 function distance_to_m_antenna = calculate_distance_to_m_antenna(
```

```
m, y_rx_pos, z_rx_pos, y_antenna_tx_pos, z_antenna_tx_pos)
380 % Function to calculate the distance from m antenna element
      on the
381 % array to receiver
382 distance_to_m_antenna = sqrt((y_rx_pos-y_antenna_tx_pos(m) )
      ^2 + ( z_rx_pos - z_antenna_tx_pos )^2);
383 end
384
385 function [result_compare] = compare_matrixs(W1,W2)
386 % Function to compare matrices
387 result_compare = sum(sum(abs(W1-W2).^2));
388
389 end
```